Molecular aspect of interfacial phenomena affecting particle characteristics of drug substances

Akira Kitayama

Doshisha University

2020

Contents

Chapter 1 Introduction

1.1 Motivation and objectives

Medicines are industrial products which is an essential help ensure healthy and cultured living of all peoples. Pharmaceutical companies have aimed pharmaceutical development which is to design a quality product and its manufacturing process to consistently deliver the intended performance of the product. As regulatory system required for the industry which may have critical aspect for the life of people, the International Conference on Harmonization of Pharmaceutical Regulations Guidelines (ICH) Q8, Q9 and Q10 have been passed since upon more than 10 years with agreement.[1-3] Guideline indicates that the physicochemical and biological properties of the drug substance that can influence the performance of the drug product and its manufacturability, or were specifically designed into the drug substance (e.g., solid state properties), should be identified and discussed as Critical Quality Attribute (CQA). A CQA is a physical, chemical, biological, or microbiological property or characteristic that should be within an appropriate limit, range, or distribution to ensure the desired product quality.[4] Examples of physicochemical properties that might need to be examined include solubility, water content, particle size, crystal properties. These properties could be interrelated and might need to be considered in combination.

Small molecule is a low molecular weight (<900 daltons[5]) organic compound that may regulate a biological process, with a size on the order of 1 nm within the fields of molecular biology and pharmacology. This “Small molecules” still accounted for 71% (42 of the 59) of new drug substances molecule entities approved by the FDA[6] in 2018 even in the last two decades which large molecules (e.g. antibody) have been expanded in the share of modality of drug substances.[7] The pharmaceutical manufacturing process of small molecule can be divided into two parts: drug substance and drug product. Drug substance is defined as any substance or mixture of substances intended to be used in the manufacture of a drug (medicinal) product and that, when used in the production of a drug, becomes an active ingredient of the drug product. Drug product is a finished dosage form, for example, tablet, capsule or solution that contains a drug substance, generally, but not necessarily, in association with inactive ingredients. The drug substance of small molecules (most of them are crystallized) is usually obtained through mixing, reaction, separation (crystallization), grinding processes.[8] Afterwards, the final formulation is made into a product through the subsequent formulation process, e.g. pre-blending, granulation, sieving, blending, tableting, and film-coating.[9] As mentioned as example of CQA above, particle size distribution of drug substance is a critical property affecting drug product performance.[10] Smaller particles which has under 100 μm as particle diameter dissolve faster and may improve bioavailability of the drug as a result.[11] Such particles are typically dispersed more uniformly as relative standard deviation of within 2.0 %, leading to lower inter-tablet potency variation even if such as below 1.0 mg dose tablet.[12] On the other hand, smaller particles which is under 100 μm can also result in poor powder handling characteristics or other down processing issues. For example, powders can fail to flow through hoppers or stick to tooling surfaces, leading to poor tablet content uniformity or tablet appearance issues.[13,14] During crystallization, smaller particles can also be difficult to filter from the crystallization media. This can lead to higher levels of residual solvents and other impurities. Particle design and size selection are therefore critical to achieving a balance among such as bioavailability, manufacturability, and content uniformity of final drug product.[15]

Considering such critical impacts on drug product due to the solid state of drug substance, especially crystallization and milling process of drug substance have more significant impact to the final quality and manufacturability of the "drug product" design point of view as shown in Figure 1-1. Because the crystallization process yields the crystal form as solid from liquid and the solid-state characteristics which are derived intrinsically from molecular properties and crystal structures. Milling process intends to get desired particle size distribution by input mechanical energy and usually is last process as for drug substance. High mechanical energy can change not only the properties which related shape and size, but also accompanied with crystal lattice deformation and relaxation. These changes may occur during and after the process.[16]

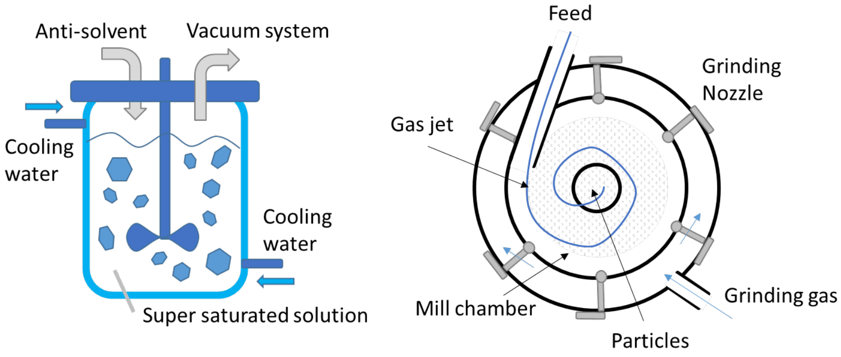

Fig. 1-1 Typical processes of drug substances e.g.) crystallization[17] and milling[18].

One of typical issues from crystallization is the non-uniformity of the crystal morphology lead by the change of the dehydration rate generated at the microscopic liquid–liquid interface on the process with anti-solvent.[19,20] In addition, high energy state at the solid–solid interface caused by the friction energy between the crystals and the metal surface of the equipment induce unintended amorphization on the crystal structure and degradation by excess heat.[21] These physical and chemical change may have impact on the drug substance quality and manufacturability of subsequent galenical processes.

As described above, there are interfacial phenomena of the combination of gas, liquid and solid in crystallization and milling process and the phenomena significantly affect not only the quality of the final drug product but also the processability via the particle characteristics of drug substance.[22] Therefore, it is very important to understand the interfacial phenomena to give the desired properties to the particles and to design the manufacturing suitability. However, the phenomena at liquid–liquid and liquid–solid interfaces are difficult to understand compared to the one at the gas-solid and gas-liquid interfaces (surfaces), which are generally easy to observe and have been widely studied and well known. In general, it is difficult to experimentally observe the fast time-varying microscopic phenomena at the liquid–liquid and liquid–solid interfaces due to the problems of spatial and time resolution.[23] In addition, the contact area cannot be directly observed at the solid–solid interface and makes it more difficult to reveal due to the difference of the intermolecular interactions between bulk and limited surface which has major role of phenomena. Experimental and/or theoretical approaches can provide practical solutions through the studies. However, it causes to stay potentially at superficial understanding to the issues and may lead to the overlooking the critical aspect of phenomena which indicated by the observation. Therefore, every new drug substance of small molecule is synthesized and developed to the market, it has potential issues in the commercial manufacturing process and not to motivate preventive and continuous improvement.

To overcome these issues, numerical simulation has been highlighted widely used as a “3rd approach of science” recently. Also, statistical analysis is focused as meant to add inductive insight. Combination of these approaches is called “4th approach of science"[24] as shown in Figure 1-2 and ensure constant quality throughout the lifecycle of product over the next few decades by shedding light to pleiotropic point of view. Needless to say, the first paradigm is experimental science. Experimental facts are the foundation of science, and actual experimental proofs most certainly contribute to the development of science. The second paradigm is theoretical science. Various theories have been established. Such a theory makes it possible to predict the results to be obtained without examining the myriad of possible experimental conditions. However, the third paradigm, numerical simulation is needed as combination with former two approaches due to limitation comes from theoretical model and/or experimental resolution. As theoretical models have gradually become more complex, it has become more difficult to predict outcomes from the models. Therefore, simulations that obtain results by numerical computation using computers, rather than analytical solutions to theories, have attracted a lot of attention. Nowadays, the fourth paradigm, data-intensive science is focused. Simulations have produced large amounts of data, and with the evolution of measurement instruments, large amounts of data can be obtained from experimental science in a short time. The fourth paradigm of data-intensive science is the approach to gaining new knowledge by aggregating these data in one place.

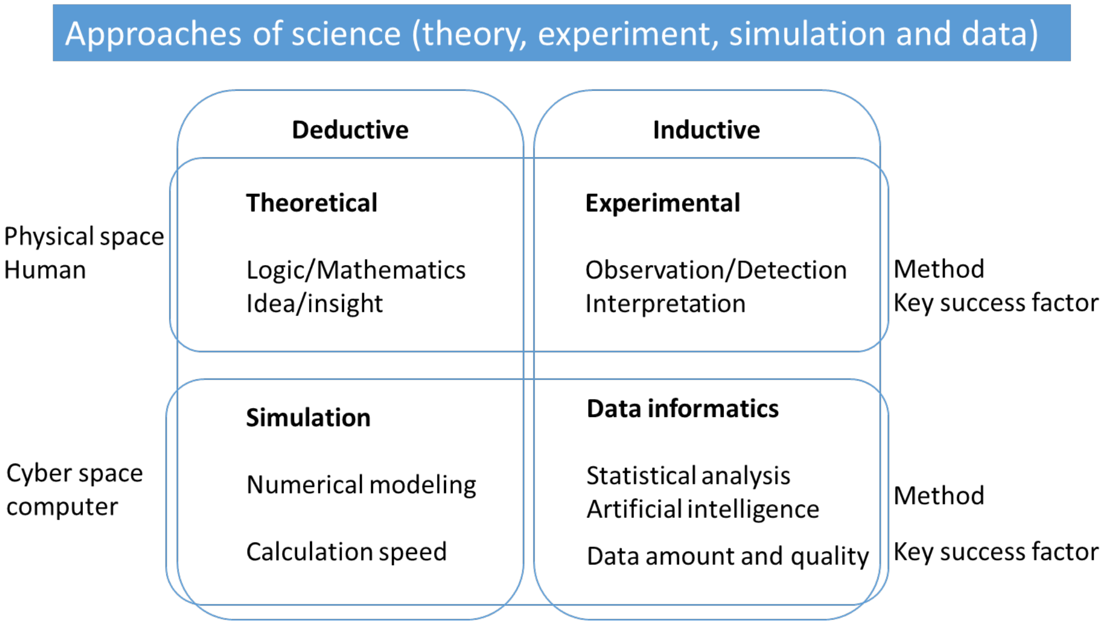

Fig. 1-2 Conceptual diagram of fourth approach of science.

The objective of this thesis is to study the interfacial phenomena which affecting particle characteristics of drug substance. Especially the interface which consisted with liquid and solid phase (liquid–liquid, liquid–solid and solid–solid) are focused on because of the importance of the phenomena and the difficulties by experimental approach, as illustrated in Figure 1-3. This thesis is devoted following topics,

- Study of the microscopic diffusion behavior of water/organic solvents interfaces by MD (Molecular Dynamics) simulation
- Evaluation of the impact on dehydration mechanism of ions by organic solvent by MD simulations
- Investigation of the clustering/nucleation mechanism during anti-solvent crystallization of amino acid as a model drug substance by MD simulations
- Study of the diffusion behavior of Vitamin C & E derivatives from hollow TiO_2 particles which are prepared liquid-liquid interfacial reaction

- Development of an evaluation method for the degree of amorphization of indomethacin and cystine observed during a ball milling by DEM and PCA

Liquid–liquid interfacial phenomena is addressed via investigation of diffusion and clustering behavior of solutes as model for anti-solvent crystallization process in Chapter 2-4. And liquid–solid interfacial phenomena is discussed in Chapter 5 through the interaction diffusion behavior of multi vitamin between vitamins and porous titanium oxide particles. As one of instantaneous change at molecular level of solid, solid–solid interfacial phenomena is focused especially on their unusual change of amorphization of drug substances during co-grinding in Chapter 6.

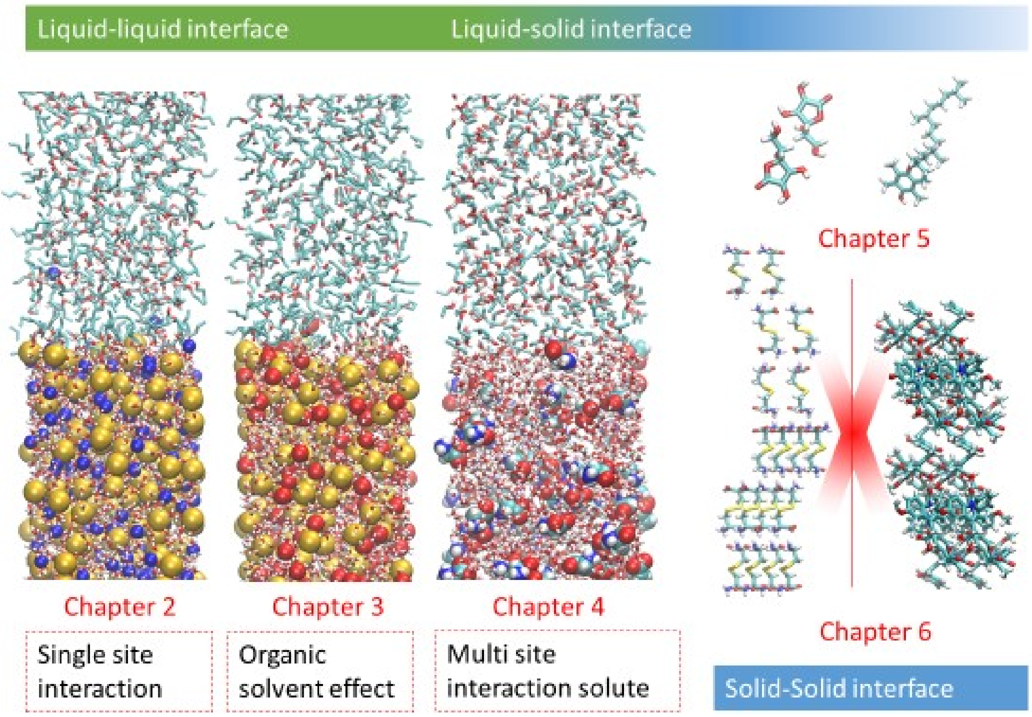

Fig. 1-3 Schematic illustration of the structure of this thesis.

1.2 Review of previous works

An interface is defined as the boundary between two spatial regions occupied by different matter, or by matter in different physical states. The interface between matter and gas, or matter and vacuum, is called a surface. Interfaces are very important in systems with large interface area-to-volume ratios, such as colloids.[25]

Using article search service of the “Scopus”, which is Elsevier’s abstract and citation database launched in 2004, the number of journal publications with the keyword “interface” combined with "surface (gas–liquid, gas–solid)," "liquid–liquid," "liquid–solid" and "solid–solid" over the last 40 years, and the results are shown in Figure 1-4. Although it is not possible to estimate the technical difficulty of the research directly from the number of papers, there is no doubt the “surface” to be obtained about related knowledge through the studies for a long time and has been widely selected as a research object. This is suggested by the fact that the number of papers on the solid–solid interface, which is most difficult to observe directly by experiments among interphases, is low number compared to the one of liquid–liquid and liquid–solid interfaces. The number of papers for such tough targets has been increased in recent years due to the development of analytical apparatuses such as spectrometers and numerical simulations getting more common. The following sections provide an overview of the research on each interface especially in crystallization and milling process which has significant impacts on particle characteristics of drug substance as review of previous research in this dissertation.

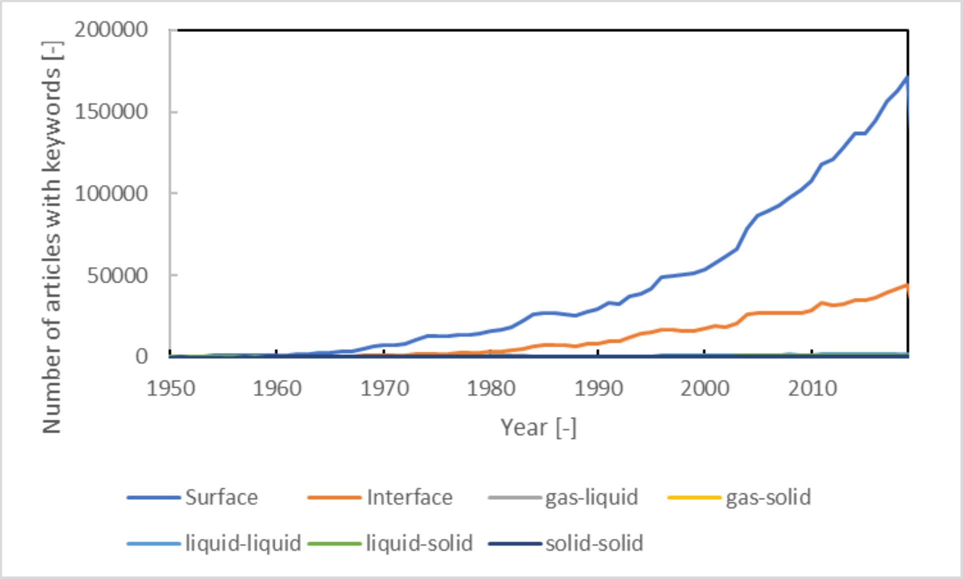

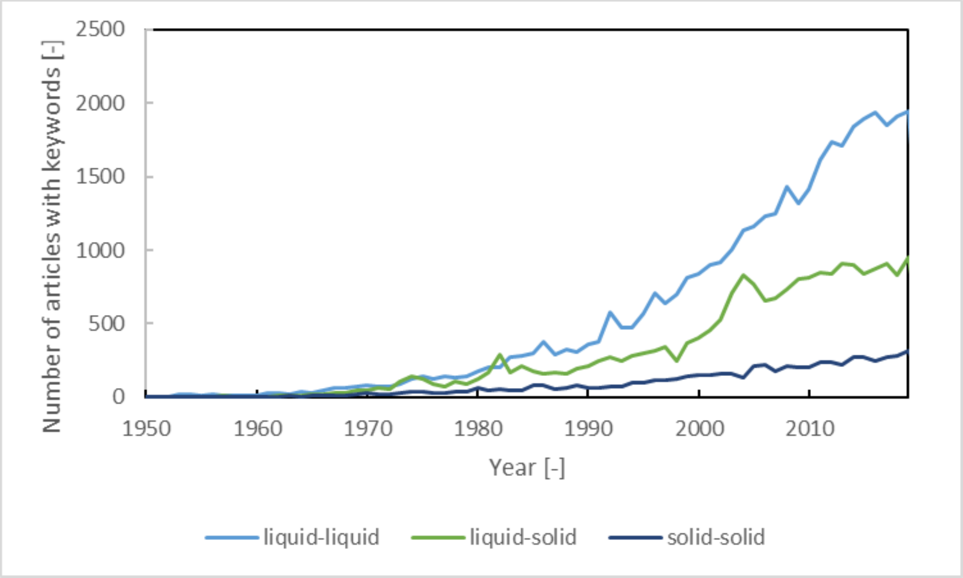

Fig. 1-4 Number of articles from the survey of “Scopus” database.

1.2.1 liquid–liquid interface affecting particle characteristics

In a system with two liquids, internal attractive forces between them (e.g. Van der Waals forces, Coulomb force, hydrogen bonds) and the liquid-liquid interfaces play a key role in various physical and chemical processes (adsorption, liquid–liquid extraction, heterogeneous catalysis, chromatography, or drug delivery).[26, 27] Physical properties such as density, solubility, or dielectric constant change abruptly, yet continuously, in the vicinity of the interfaces. The molecules located at the interface experience a significant different local environment with reference to bulk phases. Physical properties such as orientation, diffusion constant or binding energy of the interfacial molecules are significantly different than those of the bulk phases. Regarding the manufacturing process of drug substances, for example, during anti-solvent crystallization, nucleation and crystal growth is governed both by bulk diffusivity of solvents and solute by interfacial mutual transfer and by localized supersaturation depends on mixing behavior.[28]

Focusing on this particularity, liquid–liquid interface is one of the attractive field for creating new functional materials where various phenomena such as the chemical reaction, extraction and nucleation might occur.[29] There have been many studies on phenomena at liquid–liquid interfaces, which have been important to comprehend the voltammetric studies in electrochemical field.[30-33] Lee et al. studied an ion transfer reaction at liquid–liquid interfaces for electrochemistry.[34] Riva et al. investigated the adsorption and desorption process of cationic molecules at liquid–liquid interfaces using cyclic voltammetry.[35] They analyzed the effect of potential and time polarization as well as the nature from electrochemical perspective. A few researchers have applied the liquid–liquid interface to the field of particle generation by the use of ion transfer at the interface between immiscible electrolyte solutions.[36,37] Miyazawa et al. produced the C60 nano-whiskers with a liquid–liquid interfacial precipitation method.[38] Our group could also be successful in producing asymmetric particles, porous particles and composite particles using liquid–liquid interfacial crystallization.[39-42] These previous works suggested that the fabrication of particles on liquid–liquid interface had a tremendous amount of potential. There has remained much to be studied on the phenomena on liquid–liquid interface at atomic level although the possibility of predicting mutual diffusion was indicated by measuring the solution electrical resistance near interface between solution and organic solvent.[43] It is expected that the microscopic behavior of NaCl and KCl near solution/organic solvent interface might be predicted by measuring Fourier transform infrared spectroscopy (FT-IR).[44,45] The structural change in the liquid–liquid interface due to the mutual diffusion significantly affects the performance of the crystal precipitation. However, time evolution of the interfacial structure for slightly miscible state cannot be observed only by experiments at microscopic level.

1.2.2 liquid–solid interface affecting particle characteristics

Dynamic processes at the solid–liquid interface are key importance across broad areas of science and technology. The processes understanding at the solid–gas interface has advanced tremendously over the past decade due to the routine availability of real-time, high-resolution imaging techniques yielding data that can be compared quantitatively with theory.[46] However, the difficulty of studying the solid–liquid interface leaves our understanding of processes there less complete.

As described above, crystallization is a process that can assume a solid form through mediated solutes as the generation field of liquid–solid interface. Owing to its superior generality towards purified materials, crystallization is widely used in commercial industries, such as food, chemicals and pharmaceuticals. The purified solid material can be yielded through nucleation or crystal growth wherein solutes have been desolvated from solvents. The process of crystallization remains difficult to understand as the involved procedures utilize a wide ranged and complex system from the molecular to visible particle levels with intermediate metastable states in a solute and solvent mixture. Typically, nucleation and crystal growth are described as a fundamental step for crystallization, which is described in classical nucleation theory (CNT).[47] To generate the target quality of the crystal by controlling the nucleation and crystal growth process, mechanistic understanding through theoretical and experimental approaches has been implemented for several decades.[48-50] The nucleation and crystal growth processes significantly impact the physical and chemical properties and manufacturability for the down processing of products, which are used with the crystal. In addition, crystal characteristics (e.g. shape and size distribution) are key to understanding the specific function of the material for the target product.[51] The approach utilizing the classical nucleation theory can be easily implemented in some cases. However, further understanding is required for implementations in more practical scenarios that are not considered in CNT as they can be complex owing to the stochastic and strong impact of boundary conditions.[52]

1.2.3 solid–solid interface affecting particle characteristics

Being close to the end of process steps of drug substance, final form crystallizations typically is considered to ensure filtration rates are acceptable and thus large crystals are generally manufactured. Historically, however, there has been little effort placed on developing the engineering science to consistently control the particle size during crystallization to directly meet particle size specifications of the drug substances. Therefore, the drug substance is subjected to size reduction steps through a milling to achieve the desired particle size distribution. Milling steps are applied to avoid potential downstream issues,[53] however, there are fundamental issues that can arise from size reduction of drug substance due to the high energy impacts via solid–solid interface. For example, crystallinity can be reduced on grinding and in other words, this means unexpected increase of amorphous state. Molecular mobility modes were reported their uniqueness for micronized material compared to the amorphous reference and this indicated that micronized drug substance has physically distinct disorder compared to phase-separated amorphous material.[22] Sometimes, polymorphic changes can be observed on the milling process including bound hydrate. In such a case, grinding process causes irreversible change to the hydrated crystal lattice and this has the potential impact on bioavailability due to less dissolution rate of form changed drug substance. These issues are originated on the solid–solid interface and hard to be investigated by experimental approach directly.

1.3 Dissertation outline

This thesis consists of seven chapters and a brief summary of the contents is as follows:

Chapter 1 describes the introduction, including the objectives and literature review.

Chapter 2 presents the study of interfacial phenomena and crystallization driven by mutual diffusion in a system consisted with ionic solutes, water and primary alcohol. Nonequilibrium molecular dynamics (MD) simulations were performed at interfaces in NaCl solution/1-butanol and KCl solution/1-butanol system to characterize diffusion behavior of solute ions and solvent molecules. Clustering interactions of ions were investigated as simple sites under slightly miscible system. The investigation provides the understanding of origin which leads the difference of each dehydration behavior of ionic solute at molecular level.

Chapter 3 highlights effect of organic solvents on the mutual diffusion and ionic behavior near the liquid–liquid interface between KCl aqueous solution and organic solvent (1-butanol, 2-butanol, 2-methyl-1-propanol and 2-butanone) via the Non-equilibrium molecular dynamics simulations based on the results of Chapter 1. Organic molecules showed the orientational motion in the interfacial region with time evolution and enhanced the concentration fluctuation of solute ions near the interface.

Chapter 4 describes that the anti-solvent crystallization behavior of the glycine aqueous and ethanol system was addressed through a molecular dynamics simulation of a non-equilibrium state. Water, ethanol and glycine zwitterions were selected to investigate the anti-solvent crystallization system at molecular level as simple model material which has multi-interaction sites of molecules. Glycine began to aggregate into clusters with the invasion of ethanol into the aqueous phase, caused by the dehydration and supersaturation of the area.

Chapter 5 presents study that a multivitamin that has hydrophilic and hydrophobic properties and its diffusion behavior from titanium dioxide (TiO_2) hollow particles. The TiO_2 hollow particles encapsulating the vitamins C and E were prepared via a sol-gel reaction process on the liquid–liquid interface formed by an inkjet nozzle. The release behavior of the multivitamin was quite different from that of each single vitamin. This is related to the adsorption state of each vitamin on the TiO_2 particle surface.

Chapter 6 describes the study that the amorphization of indomethacin (IMC) with cystine (Cys2) by discrete element method (DEM) simulations and principal component analysis (PCA). PCA results suggest that IMC/Cys2 system undergoes two-phase amorphization, as indicated by the 2nd PC score, and that the change in phase depends on the total frictional energy calculated by DEM simulations. This findings were gained through the 4th approach of sciences as described above.

Finally, Chapter 7 summarizes the conclusions obtained based on the results of this thesis.

References

[1] International Conference on Harmonisation, *Harmonised tripartite guideline, pharmaceutical development Q8(R2),* 2009

[2] International Conference on Harmonisation, *Harmonised tripartite guideline, Quality Risk Management (Q9)*, 2005

[3] International Conference on Harmonisation, *Harmonised tripartite guideline, Pharmaceutical Quality System (Q10)*, 2008

[4] International Conference on Harmonisation, *Harmonised tripartite guideline, Development and Manufacture of drug substances (Chemical Entities and Biotechnological/Biological Entities) (Q11)*, 2012

[5] M. J. Macielag, *Antibiotic Discovery and Development*, In: Dougherty T., Pucci M. (eds) Antibiotic Discovery and Development. Springer, Boston, 793-820

[6] U. S. Food and Drug Administration, *Center for Drug Evaluation and Research's (CDER) annual report, Advancing Health Through Innovation: New Drug Therapy Approvals, 2018*

[7] M. Saito, *Folia Pharmacol., Jpn.*, 2016, **147**, 168-174

[8] K. D. Seibert, S. Sethuraman, J. D. Mitchell, K. L. Griffiths and B. McGarvey, *J Pharm Innov*, 2008, **3**, 105–112

[9] L. X. Yu, *Pharmaceutical Research*, 2008, **25**, 4

[10] S. I. Farag Badawy, T. J. Lee and M. M. Menning, *AAPS PharmSciTech*, 2000, **1**, 4, 33

[11] S. Kim, B. Lotz, M. Lindrud, K. Girard, T. Moore, K. Nagarajan, M. Alvarez, T. Lee, F. Nikfar, M. Davidovich, S. Srivastava and S. Kiang, *Organic Process Research & Development*, 2005, **9**, 894−901

[12] J. Hilden, M. Schrad, J. Kuehne-Willmore and J. Sloan, *J. Pharm. Sci.,* 2012, **101**, 7, 2364-2371

[13] E. Kougoulos, I. Smales and H. M. Verrier, *AAPS PharmSciTech*, 2011, **12**, 1, 287-294

[14] D. Mateo-Ortiz, F. J. Muzzio and R. Méndez, *Powder Technol.*, 2014, **262**, 215-222.

[15] M. Leane, K. Pitt, G. Reynolds and The Manufacturing Classification System (MCS) Working Group, *Pharmaceutical Development and Technology*, 2015, **20**, 1, 12–21

[16] R. Ho, M. Naderi, J. Y. Y., Heng, D. R. Williams, F. Thielmann, P. Bouza, A. R. Keith, G. Thiele and D. J. *Burnett Pharm Res.*, 2012, **29**, 2806–2816

[17] M. Fujiwara, Z. K. Nagy, J. W. Chew, and R. D. Braatz, *Journal of Process Control*,

2005, **15**, 493–504

[18] S. Bhonsale, D. Telen, B. Stokbroekx and J. Van Impe, *EPJ Web Conf,*. 2017, **140**, 07003

[19] C. T. O′ Ciardha′, P. J. Frawley and N. A. Mitchell, *Journal of Crystal Growth*, 2011, **328**, 50–57

[20] N. Kubota, *Journal of Crystal Growth*, 2008, **310**, 4647–4651

[21] P. A. Priemel, H. Grohganz and T.Rades, *Advanced Drug Delivery Reviews*, 2016, **100**, 126-132

[22] R. Forcino, J. Brum. M. Galop and Y. Sun, *Pharm Res.*, 2010, **27**, 2234–2241

[23] D. O'Grady, M. Barrett, E. Casey and B. Glennon, *School Chemical Engineering Research and Design,* 2007, **85(A7)**, 945–952

[24] T. Hey, S. Tansley and K. Tin Tolle, *The Forth Paradigm Data-IntensIve scIentIfIc Discovery*, Microsoft Research, 2009

[25] S. A., Bratko, D., Wu, J. Z., Elvassore, N., Blanch, H. W., Prausinitz and J. M., *J Chem Phys.,* 2002, **116**, 7733-7743

[26] Y. Kawashima, *Spherical Crystallization as a New Platform for Particle Design Engineering*, Springer, 2019.

[27] K. Patchigolla and D. Wilkinson, *Ind. Eng. Chem. Res.*, 2008, **47**, 804

[28] R. B. Hammond, K. Pencheva, and K. J. Roberts, *Crystal Growth & Design,* 2006, **6**, 6, 1324-1334

[29] A. G. Volkov and D.W. Deamer, *Liquid–liquid Interfaces Theory and Methods*, CRC Press LLC, 1996.

[30] R.A. Iglesias, S.A. Dassie and A.M. Baruzzi, *J. Electroanal. Chem.* 2003, **556**, 23–33

[31] G. M. Gassin, P. M. Gassin, L. Couston, O. Diat, E. Benichou and P.F. Brevet, *Colloids Surf. A Physicochem. Eng. Asp.*, 2012, **413**, 130–135

[32] N.E.A. Cousens, A.R. Kucernak, *Electrochem. Commun.*, 2013, **31**, 63–66

[33] J. Saien, S. Asadabadi, *Colloids Surf. A Physicochem. Eng. Asp.*, 2014, **444**, 138–143

[34] S.H. Lee, J. Sumranjit, P. Tongkate, B.H. Chung and H.J. Lee, *Electrochim. Acta*, 2014, **123**, 198–204

[35] J.S. Riva, R. lglesias and L. M. Yudi, *Electrochim. Acta*, 2013, **107**, 584–591

[36] S. Amemiya, J. Kim, A. Izadyar, B. Kabagambe, M. Shen, R. Ishimatsu, Electrochim. Acta 2013, **110**, 836–845

[37] Y. Gründer, M.D. Fabian, S.G. Booth, D. Plana, D.J. Fermín, P.I. Hill and R.A.W. Dryfe, *Electrochim. Acta*, 2013, **110**, 809–815.

[38] K. Miyazawa, Y. Kuwasaki, A. Obayashi, and K. Kuwabara, *J. Mater. Res.,* 2002, **17**, 83–88.

[38] K. Kadota, S. Tanida, Y. Shirakawa, A. Shimosaka, J. Hidaka, *J. Chem. Eng. Jpn.*, 2007, **40**, 217–221

[40] M. Tanaka, S. Yamanaka, Y. Shirakawa, A. Shimosaka and J. Hidaka, *Adv. Powder Technol.*, 2011, **22**, 125–130

[41] K. Kadota, Y. Shirakawa, K. Gonda, S. Murata, Y. Tozuka, A. Shimosaka and J. Hidaka, *J. Soc. Powder Technol. Jpn.*, 2013, **50**, 790–796

[42] K. Kadota, H. Tamura, Y. Shirakawa, Y. Tozuka, A. Shimosaka and J. Hidaka, *Chem. Eng. Res. Des.*, 2014, 92, 2461-2469

[43] K. Kadota, I. Matsumoto, Y. Shirakawa, A. Shimosaka and J. Hidaka, *J. Soc. Powder Technol. Jpn.*, 2007, **44**, 427–433

[44] W. T. Cheng and S.Y. Lin, *Carbohydr. Polym.*, 2006, **64**, 212–217,

[45] E. Yoda and A. Ootawa, *Appl. Catal. A Gen.*, 2009, **360**, 66–70

[46] Z. Zhang and M. G. Lagally, *Science*, 1997, **276**, 377-383

[47] D. Erdemir, Alfred Y. Lee, and A. S. Myerson, *Accounts Chem. Res.*, 2009, **42**, 5, 621-629

[48] G. Coquerel, *J. Chem. Soc. Rev.*, 2014, **43**, 2286-2300

[49] Z. Gao, S. Rohani, J. Gong, and J. Wang, *Engineering*, 2017, **3**, 343–353

[50] N. Duane Loh, S. Sen, M. Bosman, S. Fen Tan, J. Zhong, C. A. Nijhuis, P. Král, P. Matsudaira, and U. Mirsaidov, *Science*, 2014, **345**, 620

[51] P. York, *Drug Dev. Ind. Pharm.*, 1992, **18**, 6-7

[52] B. C. Knott, V. Molinero, M. F. Doherty, and B. Peters, *J. Am. Chem. Soc.*, 2012, **134**, 48, 19544-19547

[53] J. Salazar, A. Ghanem, R. H. Müller, J. P. Möschwitzer, *European Journal of Pharmaceutics and Biopharmaceutics,* 2012, **81**, 82–90

Chapter 2

Ionic aggregation of NaCl and KCl aqueous solution at liquid–liquid interface

2.1 Introduction

The crystallization technique is classified by the driver of supersaturation for the reduction of solute solubility. Anti-solvent crystallization is one of the crystallization techniques that motivates nucleation and crystal growth with the addition of a poor-solubility solvent to a strong-solubility solvent, containing the solute.[1] One of the benefits of this method is that it can be performed under room temperature and pressure. Moreover, solubility in the mixture can be determined via direct comparison of the component ratio of the strong solvent and anti-solvent. Therefore, anti-solvent crystallization can be used for protein nucleation with temperature control, which is sensitive to the heat stress and needs of higher supersaturation, to generate a pure crystal.[2] In contrast, the local component ratio of the solvents and solutes can be changed by adding an anti-solvent over time, where variation depends on the system, particularly on a large scale. Both the static solubility of solute to each media and their mixing dynamics are crucial to control the process and crystal quality.[3,4] To avoid the complexity of anti-solvent crystallization in designing the crystallization process, separately understanding the behavior of solute and solvents in the macro and micro-scale phenomena is important. Anti-solvent crystallization has a much broader combination of the good solvent and anti-solvent as well as their component ratio to drive nucleation and crystal growth.

Anti-solvent crystallization sequentially progresses as follows: the contact of the good and anti-solvent, the anti-solvent's invasion of the good solvent and increased supersaturation of the microenvironment near the solute. The change in solvent behavior near the solute has been acknowledged as the reduction of solubility from a macroscopic perspective, and this solubility reduction can be estimated using the component ratio and experimental measurements.[5] However, the nucleation and crystal growth were initiated in the micro-scale area,[6,7] wherein solutes, good solvents and the anti-solvent interacted to yield complex effects on the crystal characteristics, even if supersaturation was maintained macroscopic as the value for bulk solution.

For example, a simple solute material, such as salt, can be precipitated with 1-butanol which has good solubility of water but poor to the salt. Figure 2-1 shows a phase diagram of water/1-butanol as a typical example as partially miscible solvents under room temperature as good and anti-solvent for electrolyte solution. In the case of precipitation of NaCl particles, the crystallization behavior in NaCl solution/1-butanol and/2-butanone showed an organic solvent dependence.[8] Moreover, the crystallizations in NaCl solution/1-butanol and KCl solution/1-butanol were performed under the same supersaturation condition. It was found that there was a difference in crystal growth rate between NaCl and KCl crystals.[9] From these previous works, it seemed that the particle growth rate depended on the mutual diffusion between water and organic solvents. Thus, structural change in the liquid–liquid interface due to the mutual diffusion significantly affects the performance of the crystal precipitation. However, time evolution of the interfacial structure for slightly mutual diffusion, which is in a nonequilibrium state, cannot be observed by any experiments at microscopic level. Therefore, the dynamics of the crystallization on the liquid–liquid interface are still not clear.

Molecular simulation provides a useful tool for investigating and modeling the structure and dynamics of the liquid–liquid interface. Early works used by Monte Carlo and molecular dynamics (MD) simulations to study on extraction processes, for example, water structures at interface and the interfacial thickness.[10–19] Chang and Dang reviewed recent advantages in molecular simulations of ion solvation at liquid interfaces.[20] They presented application of MD simulation method such as excess chemical potentials, density profiles, and hydration numbers of solute ions across some interfaces. Their interfacial structures in equilibrium states give us physical information of structural relaxation by asymmetric force fields of the interfaces. However, time evolutions of ionic and molecular behaviors or structural dynamics near the interfaces have to be revealed for clarification of the crystallization mechanism near liquid–liquid interface, nonequilibriumly.

We have researched about the mutual diffusion behavior in the vicinity of the interface in two systems, NaCl solution/1-butanol and KCl solution/1-butanol, to clarify the crystallization mechanism by using MD simulation technique that was able to obtain microscopic information of dynamical change in the interfaces. In this Chapter 2, we showed the results of nonequilibrium MD simulations for discussion of the solvent and ionic diffusion processes at liquid–liquid interfaces.

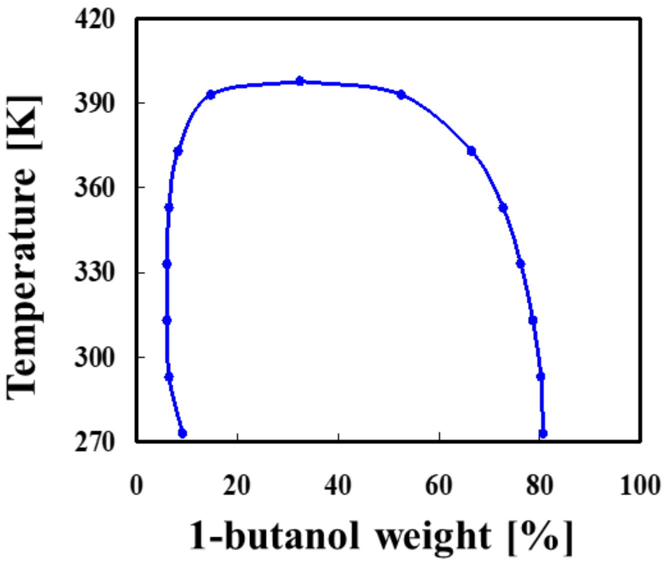

Fig. 2-1 Mutual solubility curve of water and 1-butanol.

2.2 Simulation details

Throughout this study, we used a pairwise-additive potential consisting of Lennard–Jones (L–J) 12–6 and Coulombic interactions of partial charge models to represent the potential energy of the system. Intermolecular pair potentials were taken as the sum of all pair potentials among interaction sites within molecules,

$$U(r_{ij}) = 4\varepsilon_{ij}\left[\left(\frac{\sigma_{ij}}{r_{ij}}\right)^{12} - \left(\frac{\sigma_{ij}}{r_{ij}}\right)^{6}\right] + \frac{q_i q_j}{4\pi\varepsilon_0 r_{ij}} \qquad (2\text{-}1)$$

where r_{ij}, σ_{ij}, ε_{ij}, q_i, and q_j are the separation, LJ well depth, LJ size, and partial charges, respectively, for the pair of atoms i and j, and the values of these parameters are listed in Table A-1.

Water was modeled using the extended simple point charge (SPC/E) model,[21] which included the LJ force for oxygen and Coulombic force of partial point charges located at centers of the three nuclei. 1-butanol was modeled with the Transferable Potentials for Phase Equilibria (TraPPE) Force Field.[22] Interactions in the united-atom model with the $-CH_x$ groups were treated with a single LJ site. The hydroxyl O and H interactions were modeled as the sum of the LJ and the coulmbic interactions. Effective charges for the O, H, and α-CH_2 were obtained from Ref. 22. The nonbonded interactions between sites and pseudo atoms of 1-butanol, which were separated by more than four bonds or belong to different molecules, were described by the pairwise-additive potential as mentioned above. Bond length were used their equilibrium values, and the values constraint in applying SHAKE and RATTLE algorithm (tolerance=1.0×10^{-5})[23,24], however bond angles were allowed to vibrate under harmonic potentials and torsional potentials permitted bond rotations. Values for the parameters used in the models are given in Table A-2. Sodium, potassium, and chloride ions were modeled as charged LJ spheres with the integral charge located at the center of the ion and LJ parameters obtained from Ref. 25. Unlike pair interactions were computed using standard Lorentz–Berthelot combining rules.[26]

The MD simulations were performed on a system consisting of 2400 water molecules and 864 1-butanol molecules in a rectangular simulation cell with linear dimensions of 3.20 × 3.20 × 19.82 nm^3, which yielded liquid densities of 0.998 and 0.810 $\mathrm{g/cm}^3$ for water and 1-butanol at 293.15 K,[21,27] respectively. A schematic representation of the simulation box for the water/1-butanol interface is depicted in Figure 2-2. The interface is chosen to be perpendicular to the z axis. Both solutions correspond to saturated concentration at 293.15 K. Then, NaCl solution contains 266 Na^+ and Cl^- ions, and KCl solution contains 198 K^+ and Cl^- ions.

NVT simulations were used following this adjustment with periodic boundary conditions. All simulations reported at 293.15 K in this work. The temperature was controlled by Woodcock's method.[28] With a time step of 1.0 fs, the solution and 1-butanol were individually equilibrated before the contact simulations. The velocity-Verlet algorithm was used to integrate the equations of motion, and the non-bonded interactions were based on atom-based cutoffs at 1.4 nm.[29] Ewald sum was applied for estimating the long-range Coulombic interactions with the convergence parameter $\alpha=2.214 \times 10^9$ and Kmax=7 (corresponding to a relative accuracy of the Ewald sum of 0.67×10^{-4}).[30]

Two-thirds of the simulation cell was occupied by the 1-butanol phase. This was done to try and maximize the extent of the phase into which interfacial structuring predominantly extends.[31] When the simulation box with two interfaces was used, care must be taken to prevent them from interacting. Namely, the simulation box must be long enough to ensure the independence between the interfaces. In our system, the initial separation distance between the interfaces was 7.02 nm of the water phase and 12.81 nm of the 1-butanol phase, i.e., 5.0 and 9.2 times larger than the long-range cutoff distance. It seems quite enough to avoid interfacial correlations.[32] Regarding the interfacial tension and cluster analysis, the results are directly referred from reference[6] as the results which was performed by similar simulation condition.

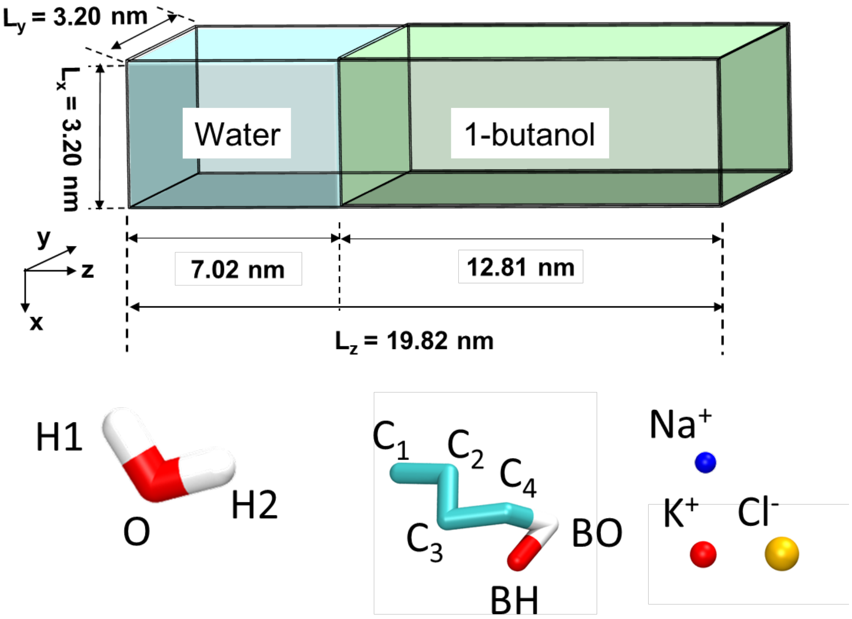

Fig. 2-2 Basic cell (e.g., water/1-butanol) used in MD simulation.

2.3 Results and discussion

2.3.1 Pure water/1-butanol interface

Water and 1-butanol mixture systems have been investigated.[18] Fidler and Rodger clarified some of details of solvation dynamics and structure.[33] Their results indicated changes in the dynamical properties of water molecules in the neighborhood of the alcohol, with longer rotational lifetimes and more oscillatory velocity correlation functions. Ferrari et al. performed standard MD simulations without explicit polarization terms, and their results could reproduce experimental properties and could show phase separation behavior. However, the liquid–liquid crystallization occurs by chemical diffusion due to motive force for transition to equilibrium concentration. Especially, in the case of NaCl solution/1-butanol, crystal surface structure in the solution side is different from 1-butanol side. It indicates that diffusion and aggregation of solute ions show different behaviors at each side. Therefore, in order to know the diffusion and aggregation behavior of solvents and solute ions by comparing molecular motions between with and without solute ions, we have simulated mutual diffusion processes on pure water/1-butanol interface. Figure 2-3 shows time dependence of the mutual diffusion on the liquid–liquid interface. As shown in Fig. 2-3, with focusing on molecular behavior of water adjacent to 1-butanol phase, individual water molecule does not uniformly solvate into 1-butanol, but partially aggregated water molecules diffuse into the 1-butanol phase. The aggregated water molecules randomly vibrate and disperse with diffusing in the 1-butanol phase.

Interfacial tension for a system with two interfaces can be calculated using,

$$\gamma = \frac{1}{2}\left\langle L_z\left(p_{zz} - \frac{p_{xx}+p_{yy}}{2}\right)\right\rangle \tag{2-2}$$

where $p_{\alpha\alpha}$ (α=x, y, or z) is $\alpha\alpha$ element of the pressure tensor and L_z is linear dimension of the simulation cell in z direction perpendicular to the interfaces. The interfacial tension is calculated in each box made by dividing the whole simulation cell into the 100 slabs (a slab thickness of 0.203 nm) parallel to the x-y plane along the z axis. The value is tabulated in Table 2-1 and it agrees rather well with experimental data.

Density profiles of water/1-butanol system were estimated in each slab. They were averaged during first 100 ps. Integration of the density profiles equaled to the total amount of molecules on any area. Essentially, the density profiles should be estimated in an equilibrium state. However, a relatively slow change in structures and strongly structural ordering can remain under averaged treatments and can be detected in their time evolution even if the structures are simulated in a nonequilibrium state. Their densities of the water and 1-butanol at a position away from the interface well agreed with bulk densities as shown in Table 2-1. Focusing on the interfacial structure, the density profiles of 1-butanol had distinct peaks in interfacial area and these peaks came from H_b, O_b, C_4, C_3, C_2, and C_1 (suffix b means an atom in 1-butanol and suffix number of C corresponds to order from the hydrophobic end of a 1-butanol molecule) in order from water to 1-butanol side. This molecular configuration means a hydroxyl group or a hydrophilic group in 1-butanol is strong interact with water phase. The distance between first and second peaks of the hydroxyl group shifted on 0.6 nm to 1-butanol side. It is found that the hydrophilic groups are to be perpendicular to the interface because of estimation of the peak shift value of the density. 1-butanol molecules are oriented in their hydroxyl group in the direction of water phase side or show polarization of 1-butanol molecules in the direction perpendicular to the water/1-butanol interface. Therefore, water molecules can easily diffuse into 1-butanol phase without steric hindrance.

The coordination number of a water molecule by 1-butanol molecules was calculated in order to quantify the structure changing with the mutual diffusion and showed in Figure 2-3. The coordination number is defined by the number of oxygen atom (O_b) of 1-butanol around oxygen atom (O_w) of water within the first minimum peak in radial distribution function of O_w–O_b (r_{min} = 0.325 nm) from water/1-butanol mixture results simulated by the equilibrium MD.[33] The coordination numbers n_i (r_{min}) can be computed by integration of the corresponding g_{ij} (r) peak to the first minimum r_{min},

$$\boldsymbol{n_i = 4\pi\rho_j \int_0^{r_{min}} g_{ij}(r) r^2 dr} \tag{2-3}$$

ρ_j denotes the number density of the jth solvent component, in this case, water is i and oxygen of 1-butanol molecule is j. n_i' are averaged every 20 ps and obtained in each slab mentioned above. As can be seen in Fig. 2-3, the region of mixing two solvents extends in the vicinity of interface and the coordination number increases with increasing contact time, gradually. Thus, the mutual diffusion between solvents advances in their time dependence. Moreover, the diffusions of the water molecules to the 1-butanol phase and the 1-butanol molecules to the water phase simultaneously take place because increasing of the coordination number is seen in the region of $z > 7.22$ nm although the interfacial initial position from the density profiles was the vicinity of $z = 7.34$ nm. However, the water molecule into the 1-butanol phase shows the dominant diffusion in comparison with the 1-butanol molecule into the water phase. This is in agreement with the tendency supposed from the value of the mutual solubility curve (Fig. 2-1) on equilibrium system. Water solubility in 1-butanol is larger than 1-butanol solubility in water. It implies active flow of water into 1-butanol.

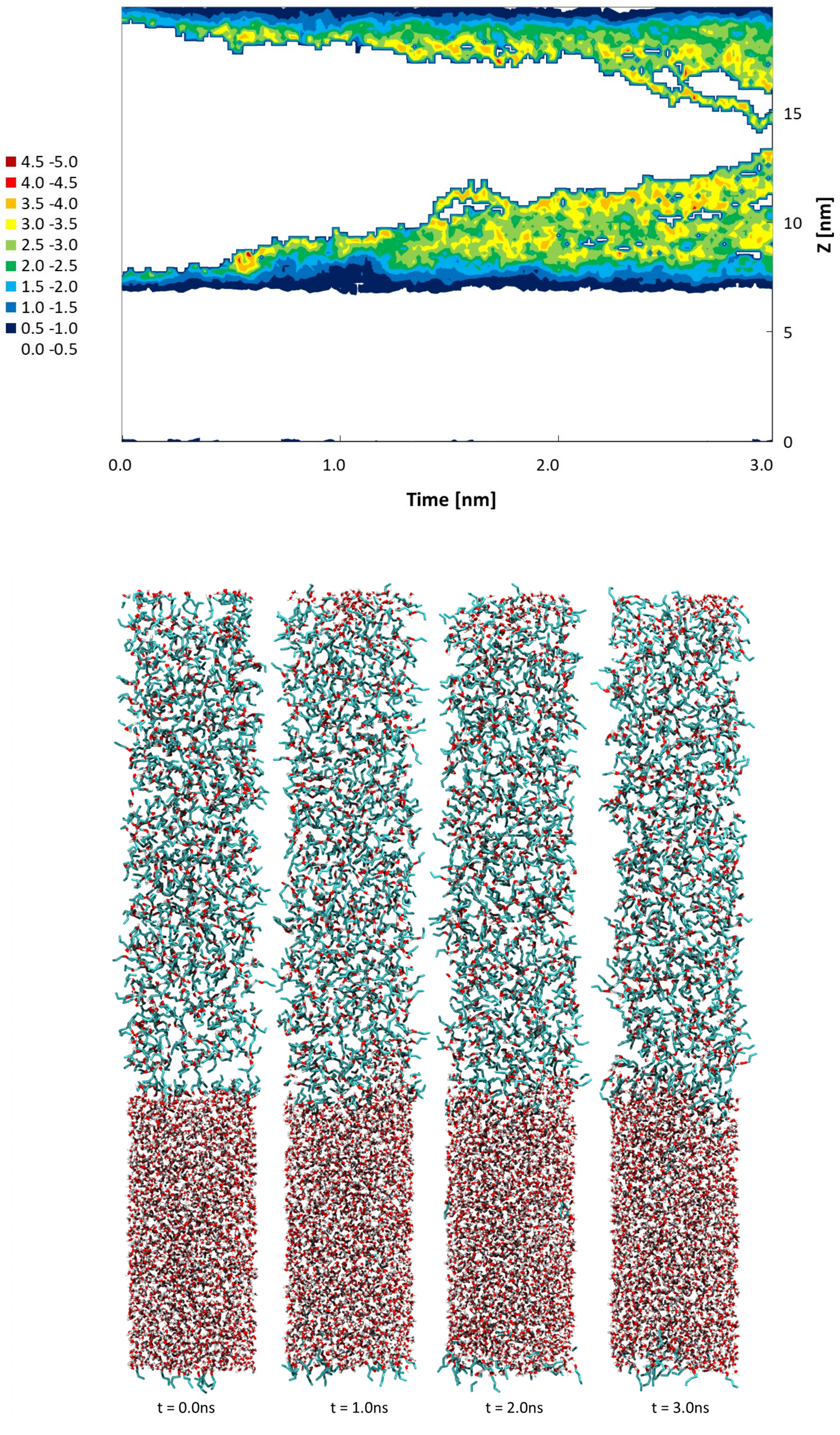

Fig. 2-3 Time evolution of coordination number of water molecule estimated from O_w–O_b bond and snapshots of diffusion behaviors at t = 0.0, 1.0, 2.0, and 3.0 ns in a water/1-butanol system.

Table 2-1 Calculated interfacial tension and density in comparing with experimental data for water/1-butanol interface

	γ [mN/m^2]		ρ [kmol/m^3]	
	Experiment[a]	Present work	experiment[a]	Present work
H_2O	1.8	1.75	55.39	55.03
1-butanol			10.93	10.55

[a] References 21 and 27.

2.3.2 Aqueous solution/1-butanol interface

This paper focuses on the mutual diffusion of solvent molecules with solute ions. The solute ions largely affect the mutual diffusion of the solvent molecules near the liquid–liquid interface. Liquid–liquid equilibrium data of partially miscible systems of water, 1-butanol, and NaCl or KCl were experimentally measured.[34] In the previous paper, it was indicated that water molecules were partitioned into the solution phase and also 1-butanol molecules into the 1-butanol phase as the amount of addition of the salt increased. In this paper, we simulated the mutual diffusion on nonequilibrium state after a contact of NaCl or KCl solution with 1-butanol phase. The mutual diffusion in the systems is obstructed to receive the effect of the salting out as well as the state of equilibrium because the salt level is the saturated concentration for both solutions. The snapshots of the simulation results and the coordination number of the solution/1-butanol system between O_w–O_b site calculated as before are shown in Figure 2-4 for NaCl and Figure 2-5 for KCl system, respectively. It is found that the solution systems have a lower amount of diffusion of the water molecules and also narrow their mixing area compared to the pure water/1-butanol system. The penetration of the mixing area makes a little headway with time, and the coordination number of the water molecules by the 1-butanol molecules does not increase on the solution phase near the interface in their time evolution. Therefore, the solute ions prevent water and 1-butanol molecules from their mutual diffusion. According to the definition of coordination number, the level of the dispersion of water molecule in the 1-butanol phase can be estimated from the degree of the coordination number when the water molecules diffuse from the solution phase. In the both of NaCl/1-butanol and KCl/1-butanol systems, mixing or penetration of the water phase into 1-butanol phase can be detected from the time evolutions of their coordination numbers. The density profiles for the solution/1-butanol systems in the vicinity of interface for t=2.9–3.0 ns were calculated. As operating the same way in pure water/1-butanol, water molecules in the solutions mainly diffused into 1-butanol phase. The amount of the diffusing water of KCl solution/1-butanol system was slightly larger than that of the NaCl solution/1-butanol system. The slope of the density profiles near the interface in the NaCl solution/1-butanol system was also larger than that in the KCl system and it had clearer interface. Therefore, in the case of the KCl solution, the mutual diffusion widely progressed into 1-butanol phase on the system.

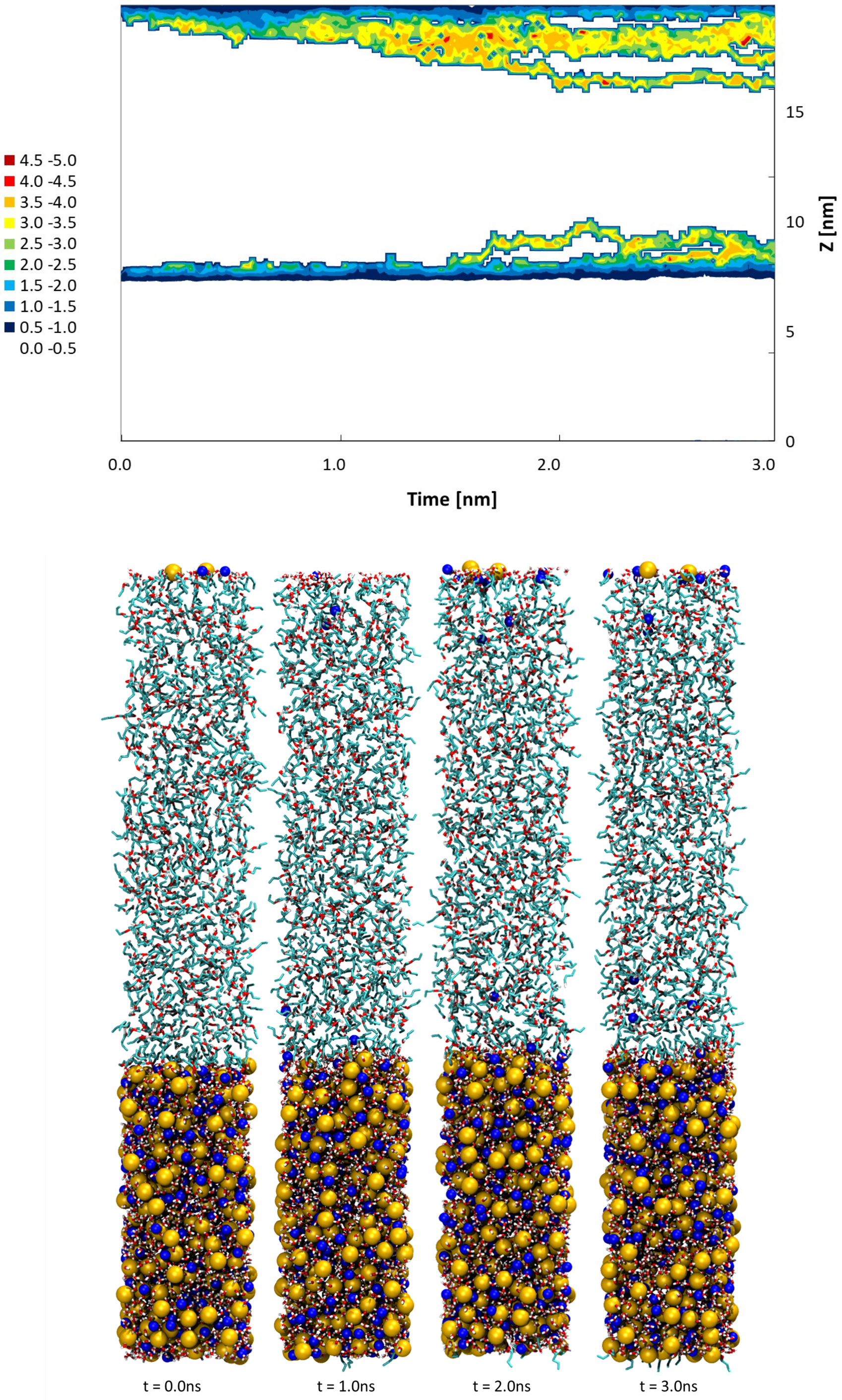

Fig. 2-4 Time evolution of coordination number of water molecule estimated from O_w–O_b bond and snapshots of diffusion behaviors at t = 0.0, 1.0, 2.0, and 3.0 ns in a NaCl solution/1-butanol system.

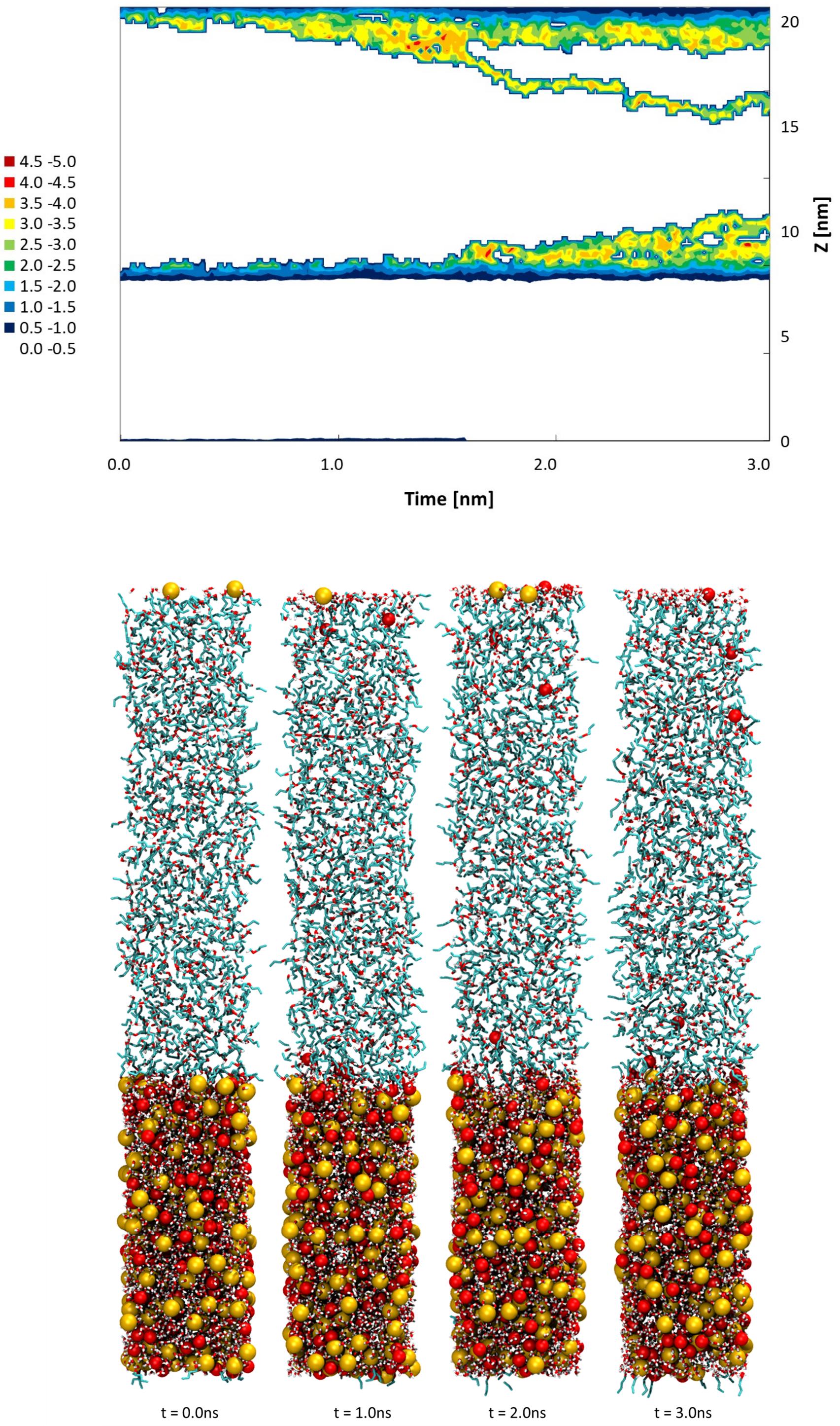

Fig. 2-5 Time evolution of coordination number of water molecule estimated from O_w–O_b bond and snapshots of diffusion behaviors at t = 0.0, 1.0, 2.0, and 3.0 ns in a KCl solution/1-butanol system.

2.3.3 Dehydration and clustering processes

The progress of mutual diffusion in the 1-butanol phase results in a concentration gradient of water near the interface. Therefore, water coordination of the solute ions decreases and the hydrated ions are dehydrated near the interface. Dehydration also occurs in solution phase by 1-butanol penetration which is smaller than water in 1-butanol phase due to their mutual solubilities. The coordination number of cations and anions by water molecules was calculated from a value of the first minimum peak of the radial distribution function between the ion and the water oxygen.[25] The coordination number of Na^+, Cl^- and K^+, Cl^- estimated from simulation results decreased with increasing contact time in the solution phase. It mainly took place in the solution side near the interface because of the solute ions concentrated close to the interface. In general, associating of solute ions gradually occurs as ionic aggregation in supersaturated solutions that is called clusters.[35] Then, we examined the influence of the difference in mutual diffusion behavior between the NaCl solution/1- butanol and the KCl solution/1-butanol on their cluster formation behavior. Cluster is defined as pairing ions within the first minimum peak of radial distribution function of their crystal state (distance between Na^+ and Cl^-) during 0.05 ns (50 000 steps).[35] Figure 2-6 shows changes in the number of clusters as function of the z axis direction calculated from the ion coordination on each step in every slab of 0.203 nm. The number was calculated as the averaged value during 0.5 ns (=500,000 steps). Compared to the NaCl solution/1-butanol, the cluster generates more locally near the interface in the KCl solution/1-butanol system. However, it expanded nonlocally over the solution area from the interface in the time evolution. In contrast, the clusters relatively gather near the interface with simulation time in the NaCl solution. Na^+ is called structure maker and K^+ is called structure breaker as ionic properties on solutions.[36–38] K^+ has weaker interaction with water than Na^+. Therefore, it was easy for the water molecules to leave the solution phase.

Time evolution of the number of clusters normalized to the total number of clusters generated in initial 0.05 ns is shown in Figure 2-7. The numbers in both cases slightly increase with increasing the simulation time. The KCl solution/1-butnaol system has the large absolute value of the number of clusters. Moreover, the cumulated value is also larger than that in the case of NaCl solution. These results are in good agreement with experimental results. Figure 2-8 and Table 2-2 show the change in the ratio and the average value of cluster size with contact time, respectively. The ratio of cluster size changed with the crystallization material and KCl clusters formed larger than NaCl clusters, as shown in Figure 2-9. A rapid increase could be obtained in the growth rate of KCl crystals on the initial stage of operation time in experiments.[7] It seems to come from the speed of the dehydration in the mutual diffusion near the interface attributed to weakness of the interaction between K^+ and water molecule as mentioned above. This is directly related to the difference in the crystal growth rate at the beginning of the operation time observed in the experiments.

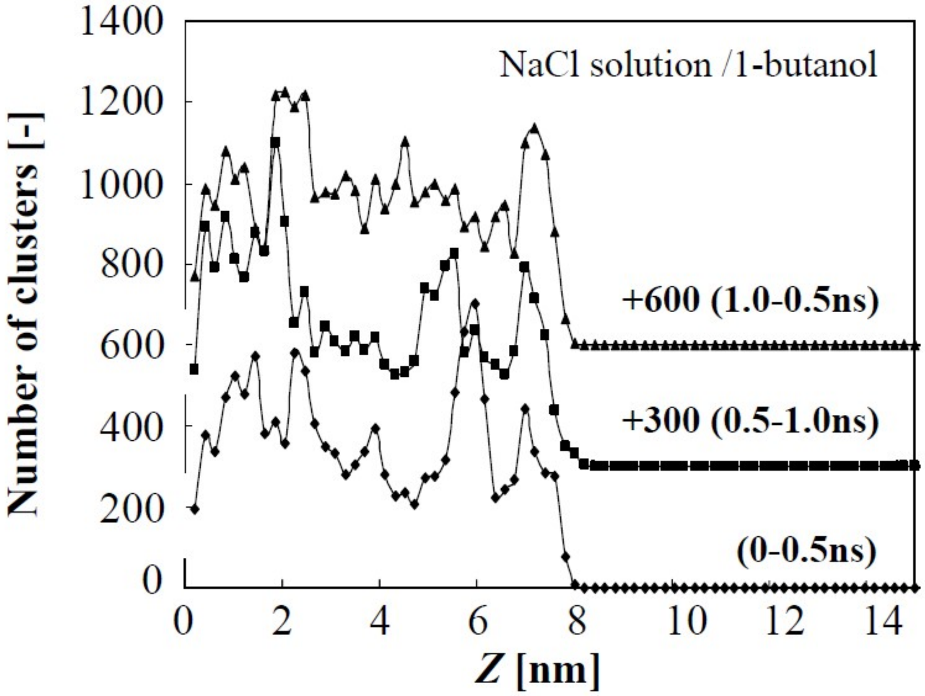

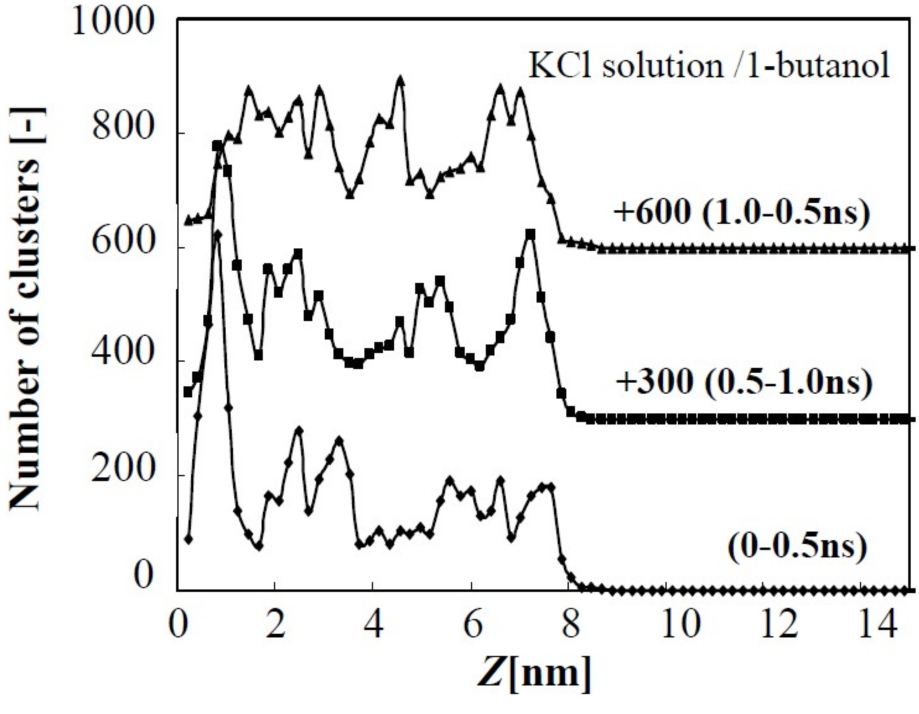

Fig. 2-6 Change in cluster distribution in NaCl solution/1-butanol and KCl solution/1-butanol.

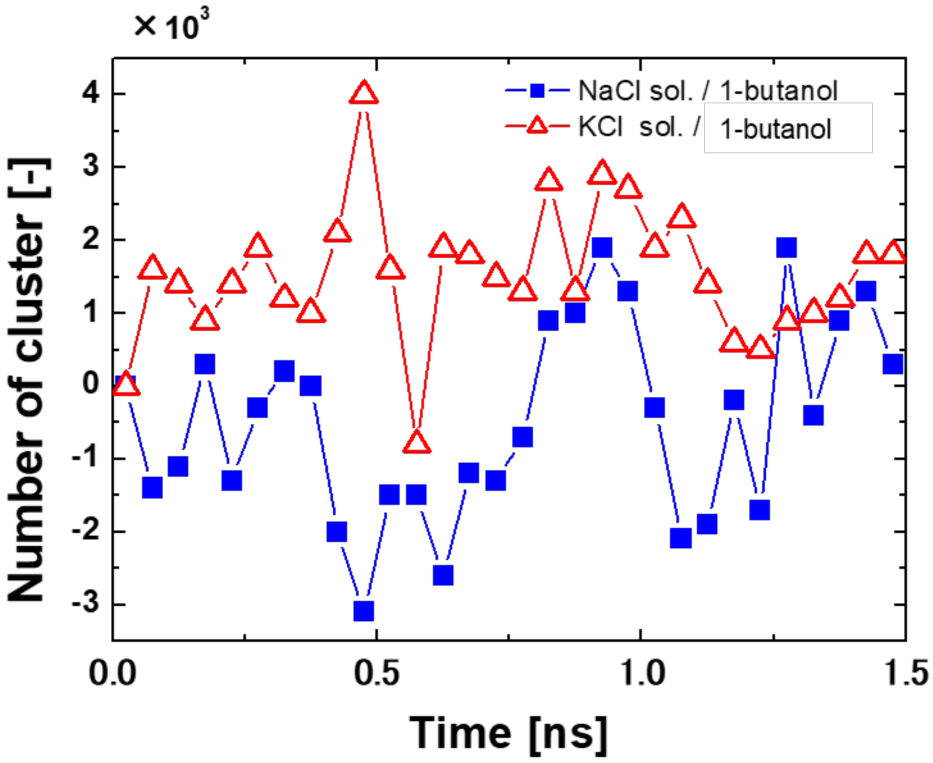

Fig. 2-7 Time dependence of total number of clusters in NaCl solution/1-butanol and KCl solution/1-butanol.

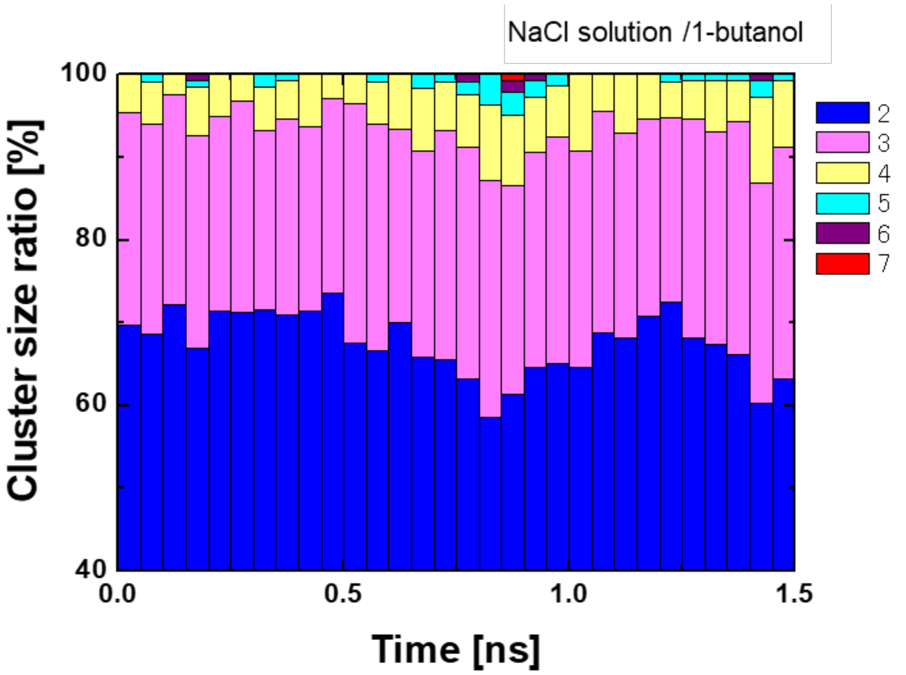

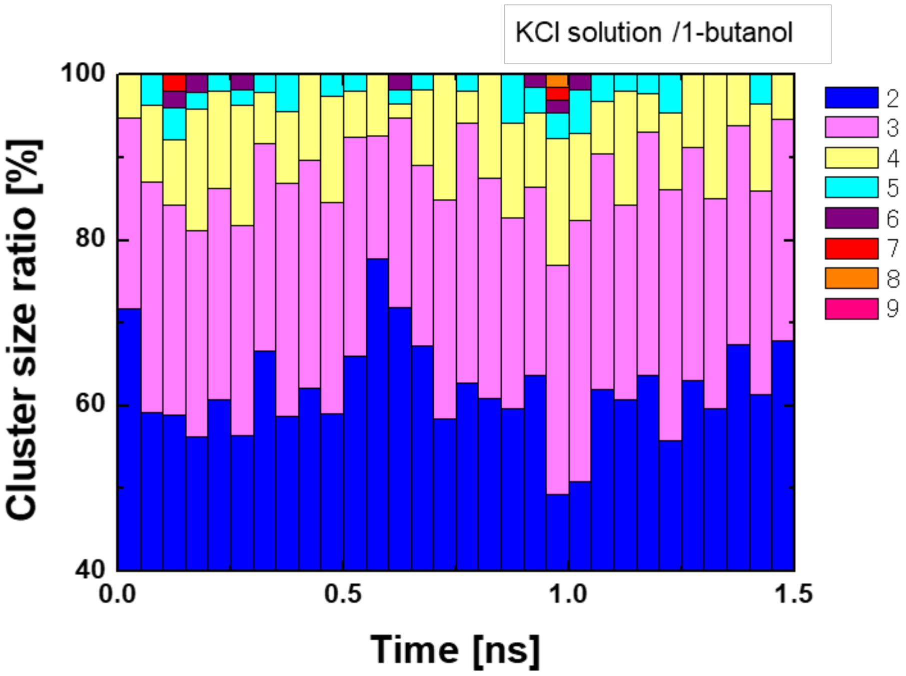

Fig. 2-8 Time dependence of cluster size ratio in NaCl solution/1-butanol and KCl solution/1-butanol. The cluster size is expressed as the number of ions in a cluster.

Table 2-2 Comparison of ratio of cluster size distribution between NaCl solution/1-butanol and KCl solution/1-butanol

Cluster size	Ratio of cluster size [%]	
	NaCl	KCl
2	67.540	61.987
3	25.643	25.920
4	5.838	9.424
5	0.811	2.087
6	0.143	0.414
7	0.704	1.749
8	-	1.538

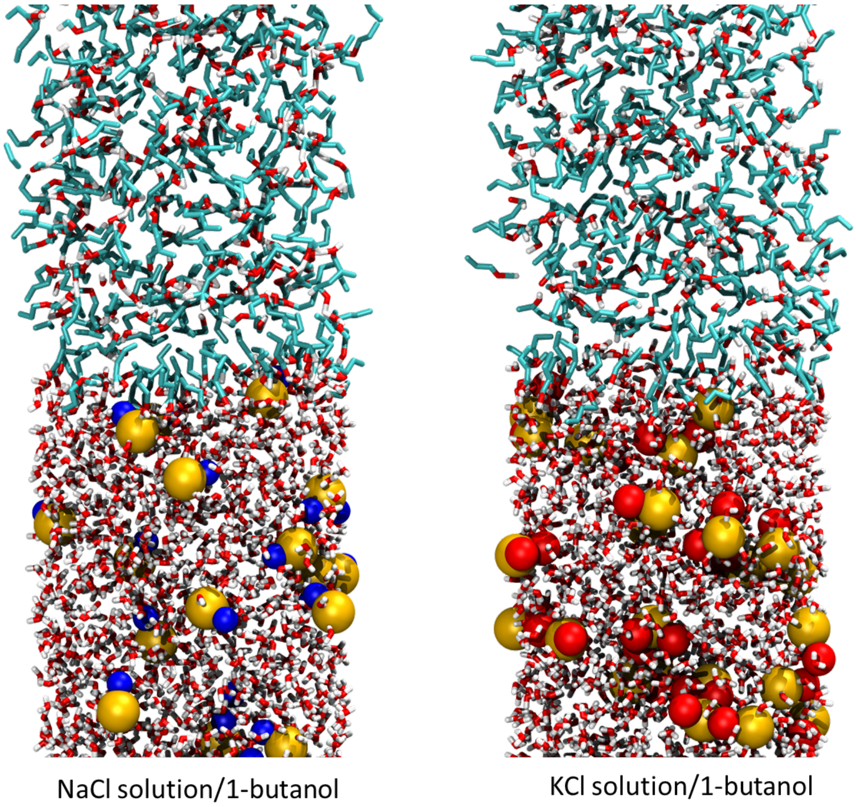

Fig. 2-9 Cluster formation difference between NaCl solution/1-butanol and KCl solution/1-butanol at t=3.0 ns. (Na^+, K^+ and Cl^- within their 1st negative peaks are only depicted.)

2.4 Conclusion

In this chapter, nonequilibrium MD simulations have performed for modeling in partially miscible solution/organic solvent systems to clarify the crystallization mechanism of the liquid–liquid interface. The diffusion of water molecules greatly changes for the solute ion effect from the results of the MD calculation. This originates in the difference between solvation structures in NaCl and KCl solutions, and the mutual diffusion behavior changes depending on the solute ions on the non-equilibrium states. We also examined how dehydration and clustering behaviors affected the nucleation processes in time evolution of the number of cluster and size. In consequence, formation of the clusters, which is the cause of the crystal nucleation and the crystal growth units, occurs in the solution phase when the degree of supersaturation rises by mutual diffusion of water in the vicinity of the interface in the anti-solvent crystallization method.

*This chapter was reproduced and modified from [*J. Chem. Phys.*, 2009, **131**, 174707], with the permission of AIP Publishing.

References

[1] A. A. Lonare and S. R. Pate, *Int. J. Chem. Eng. Appl.*, 2013, **4**, 337-341

[2] S. C. Chang, M. J. Lee, H. and M. Lin, *J. Supercrit. Fluids*, 2008, **44**, 219–229

[3] Z. K. Nagy, M. Fujiwara, and R.D. Braatz, *J. Process Control*, 2008, **18**, 856–864

[4] M. Trifkovic, M. Sheikhzadeh, and S. Rohani, *Ind. Eng. Chem. Res.*, 2008, **47**, 1586

[5] H. Teng, L. Chen and W. Y. Lee, *Food Sci. Technol. Res.*, 2017, **23**, 4 495-502

[6] A. Kitayama, S. Yamanaka, K. Kadota, A. Shimosaka, Y. Shirakawa, and J. Hidaka, *J. Chem. Phys.*, 2009, **131**, 174707

[7] K. Kadota, S. Tanida, Y. Shirakawa, A. Shimosaka, and J. Hidaka, *J. Chem. Eng. Jpn.*, 2007, **40**, 217

[8] K. Kadota, I. Matsumoto, Y. Shirakawa, A. Shimosaka, and J. Hidaka, *J. Soc. Powder Technol. Jpn.*, 2007, **44**, 427

[9] K. Kadota, Y. Shirakawa, I. Matsumoto, A. Shimosaka, and J. Hidaka, *Adv. Powder Technol.*, 2007, **18**, 775

[10] J. Gao and W. L. Jorgensen, *J. Phys. Chem.*,1988, **92**, 5813

[11] P. Linse, *J. Chem. Phys.*, 1987, **86**, 4177

[12] J. B. Buhn, P. A. Bopp, and M. J. Hampe, *J. Mol. Liq.*, 2006, **125**, 187

[13] Y. Zhang, S. E. Feller, B. R. Brooks, and R. W. Pastor, *J. Chem. Phys.*, 1995, **103**, 10252

[14] I. Chorny and I. Benjamin, *J. Phys. Chem. B*, 2005, **109**, 16455

[15] C. Wick and L. X. Dang, *J. Chem. Phys.*, 2007, **126**, 134702

[16] H. A. Patel, E. B. Nauman, and S. Gardea, *J. Chem. Phys.*, 2003, **119**, 9199

[17] A. R. van Buuren, S.-J. Marrink, and H. J. C. Berendsen, *J. Phys. Chem.*, 1993, **97**, 9206

[18] E. S. Ferrari, R. C. Burton, R. J. Davey, and A. Gavezzotti, *J. Comput. Chem.*, 2006, **27**,1211

[19] H. Daiguji, *J. Chem. Phys.*, 2001, **115**, 1538

[20] T.-M. Chang and L. X. Dang, *Chem. Rev.*, 2006, **106**, 4, 1305–1322

[21] H. J. C. Berendsen, J. R. Grigera, and T. P. Straatsma, *J. Phys. Chem.*, 1987, **91**, 6269

[22] B. Chen, J. J. Potoff, and J. I. Siepmann, *J. Phys. Chem. B*, 2001, **105**, 15, 3093–3104

[23] J.-P. Ryckaert, G. Ciccotti, and H. J. C. Berendsen, *J. Comput. Phys.*, 1977, **23**, 327

[24] H. C. Andersen, *J. Comput. Phys.*, 1983, **52**, 24-34.

[25] I. S. Joung and T.E. Cheatham, *J. Phys. Chem. B*, 2008, **112**, 9020–9041

[26] M. P. Allen and D. J. Tildesley, *Computer Simulation of Liquids*, Oxford University

Press, Oxford, 1987.

[27] S. L. Outcalt, A. Laesecke, T. J. Fortin, *J. Mol. Liq.*, 2010, **151**, 50–59

[28] L. V. Woodcock, *Chem. Phys. Lett.*, 1971, **10**, 257

[29] L. Verlet, *Phys. Rev.*, 1967, **159**, 98-103

[30] D. Fincham, *Mol. Simul.*, 1994, **13**, 1

[31] H. B. Wang, E. Carlson, D. Henderson, and R. L. Rowley, *Mol. Simul.*, 2003, **29**, 777

[32] P. A. Fernandes, M. N. D. S. Cordeiro, and J. A. N. F. Gomes, *J. Phys. Chem. B*, 1999, **103**, 6290

[33] J. Fidler and P. M. Rodger *J. Phys. Chem. B*, 1999, **103**, 7695-7703

[34] Z. Li, Y. Tang, Y. Liu, and Y. Li, *Fluid Phase Equilib.*, 1995, **103**, 143

[35] S. A. Hassan, *J. Phys. Chem. B*, 2008, **112**, 10573

[36] S. Chowdhuri and A. Chandra, *J. Chem. Phys.*, 2001, **115**, 3732

[37] J. C. Rasaiah and R. M. Lynden-Bell, *Philosophical Transactions: Mathematical, Physical and Engineering Sciences,* 2001, **359**, 1785, 1545–1574

[38] M. Manciu and E. Ruckenstein, *Langmuir*, 2005, **21**, 11312

Chapter 3

Effect of organic solvent on mutual diffusion and ionic behavior near liquid–liquid interface

3.1 Introduction

Molecular Dynamics (MD) simulations make it possible to simulate nano-scale phenomena in nano-seconds and to monitor temporal change of ionic motion at the interfacial region as shown in Chapter 2. The results revealed that the aggregation behavior of NaCl and KCl on the liquid–liquid interface depends on their solvation structures.[1] However, it remains unclear how the difference of organic solvent species affects the ionic behaviors or particle generation near the liquid–liquid interface. Mirmehrabi et al., reported A method based on the atomic electronegativity to have a systematic approach for predicting or interpreting the effect of the anti-solvents on the production of polymorphs.[2] The calculated partial charge distribution in the solute and solvent molecules has been used to predict the hydrogen bonding ability of the solute and/or solvent molecules.

In this Chapter 3, to elucidate the mechanism of this experimental approach, the effect of solvent on the ionic motion and cluster formation was examined by comparing four kinds of solvents which has four carbon atoms.

3.2 Simulation details

The potential function was used as a pairwise-additive potential consisting of Lennard–Jones (L–J) 12-6 and Coulombic interactions of partial charges models to represent the potential energy of the system. Intermolecular pair potentials were taken as the sum of all pair potentials among interaction sites within molecules as follows:

$$U_{nonbonded}(r_{ij}) = 4\varepsilon_{ij}\left[\left(\frac{\sigma_{ij}}{r_{ij}}\right)^{12} - \left(\frac{\sigma_{ij}}{r_{ij}}\right)^{6}\right] + \frac{q_i q_j}{4\pi\varepsilon_0 r_{ij}} \tag{3-1}$$

where r_{ij}, ε_{ij}, ε_{ij}, q_i and q_j are the separation, L–J well depth, L–J size and partial charges, respectively, for the pair of atoms i and j, and the values of these parameters are listed in

Table A-1. The rigid extended simple point charge (SPC/E) model was used for water molecular interactions, which included the Lennard–Jones (L–J) force for oxygen and Coulombic force of partial point charges located at the center of the three nuclei.[3] 1–butanol (n-butanol), 2-butanol (sec-butanol), 2-methyl-1-propanol (iso-butanol) and 2-butanone (methyl ethyl ketone) were modeled using transferable potentials for phase equilibria−united atom united-atom (TraPPE-UA) force field suggested by Chen and Siepmann et al..[4,5] Interactions in the united-atom model with the –CH_x groups were treated as a single L–J site. The hydroxyl O and H interactions were calculated as the sum of the L–J and the Coulumbic interactions. Effective charges for the O, H and –CH_x, which were also suggested by Chen and Stubbs et al., were adapted. The non-bonded interactions between sites and pseudo-atoms of organic molecules, which were separated from more than four bonds, were described as 1-5 interactions with the pairwise-additive potential. Bond length was used as their equilibrium values and the values constraint in applying SHAKE and RATTLE algorithm (tolerance=1.0×10^{-5}),[6,7] however, harmonic potentials are used to control bond angle bending. Torsional potentials permitted bond rotations. Potassium and chloride ions were modeled as charged L–J spheres with the integral charge located at the center of the ion and L–J parameters obtained from Joung and Cheatham.[8] Values for the parameters used in the models were given in Tables A-1 and A-2. Unlike pair interactions were computed using standard Lorentz–Berthelot combining rules[9] as follows:

$$\sigma_{ij} = \frac{(\sigma_i + \sigma_j)}{2}, \ \varepsilon_{ij} = \sqrt{\varepsilon_i \varepsilon_j} \qquad (3\text{-}2)$$

MD simulations were performed on a system consisting of 2400 water molecules and 864 organic molecules in a rectangular simulation cell, which was determined depending on the liquid densities at 293.15 K, respectively.[10-13] As an example, a schematic representation of the simulation box with the KCl sol./1-butanol interface is described in Figure 3-1 (a) and (b) represents all molecular models used in MD simulations. As a representative of organic solvent, 1-butanol is composed of BH, BO, C_4, C_3, C_2 and C_1, where suffix number of C corresponds to order from the hydrophobic end of a 1-butanol molecule. Attention must be carefully paid to prevent the boundary from interacting each other when the basic simulation cell with two interfaces was set up, indicating that the basic cell must be long enough to secure the overlapping between the interfaces.[14,15] In our calculations, the initial separation distance between the interfaces was 7.45 nm of the KCl solutions and 12.81 nm of the organic phase, i.e., 5.3 and 9.0 times larger than the long range cutoff distance. It seems quite enough to avoid interfacial correlations. Potassium chloride solution contains 198 K ions and Cl ions, which correspond approximately to saturated concentration at 293.15 K under periodic boundary conditions. The volume of aqueous solutions was determined considering the density change caused by adding the solute ions. The interface between aqueous solution and organic solvent was chosen to be perpendicular to the z axis. NVT ensemble was used by controlling temperature of 293.15 K under Woodcock's method.[16] The equation of translational motions was integrated using the velocity Verlet algorithm with time steps 1.0 fs.[17] The nonbonded interactions were based on atom-based cutoffs at 1.4 nm. Ewald sum was applied for estimating the long-range Coulombic interactions with the convergence parameter $\alpha=2.214 \times 10^9$ and Kmax=7 (corresponding to a relative accuracy of the Ewald sum of 0.67×10^{-4}).[18] The calculation for property collection was performed for 3.0 ns with a time step of 1.0 fs. The interfacial structure and ionic motion between potassium chloride (KCl) solutions and any solvents were calculated after the KCl solutions and any solvents were individually equilibrated. Two thirds of the simulation cell was occupied by the organic phase. This was done to try and maximize the extent of the phase into which interfacial structuring predominantly extends.[19] Regarding the force analysis and cluster analysis, the results are directly referred from reference[20] as the results which was performed by similar simulation condition.

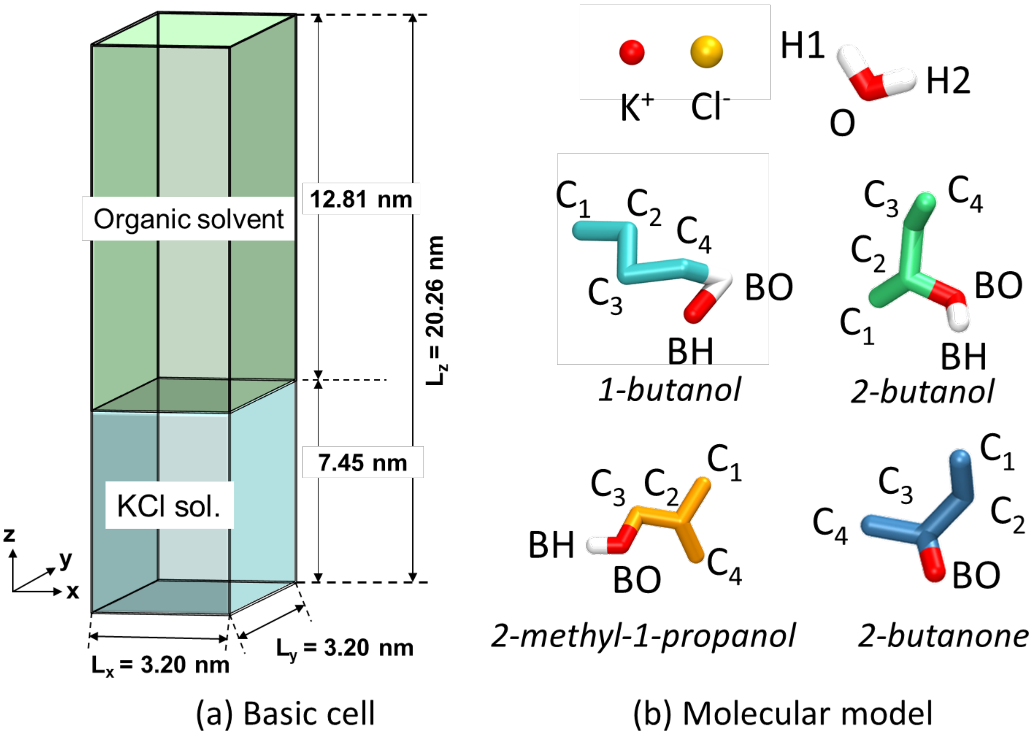

Fig. 3-1 (a) Basic cell and (b) Molecular model for the calculation of MD simulation. (e.g. organic solvent : 2-butanone)

3.3 Results and discussion

3.3.1 Mutual diffusion and density distribution

We investigated the ionic behaviors of KCl at the interfacial zone between aqueous solutions and organic solvents. Potassium ion, which is the structure-breaking ion, disorders the hydration structure. There are higher possibilities of dehydration of potassium ion than that of sodium ion near the liquid–liquid interface, indicating the nucleation of KCl dominantly occurs on the interface compared with sodium chloride.[21] However, it is still not clarified how potassium ion transfers to the organic solvent and precipitate on the liquid–liquid interface. The difference of mutual diffusion within the interface between KCl solutions and organic solvents (1-butanol, 2-butanol, 2-methyl-1-propanol and 2-butanone) was evaluated by MD simulations. We have already reported the validity of this simulation models by calculating the interfacial tension between water and organic solvents in Chapter 1.[14] Their results indicated that the interfacial tension calculated by MD simulations was in relatively good agreement with the previous experimental results.[3,10] Figure 3-2 shows the snapshots of interface between KCl solutions and each organic solvent until 3.0 ns. As shown in Fig. 3-2, the diffusion behavior of interfacial water and organic solvent is different by the type of organic solvent. Water molecules and solute ions diffuse to organic solvent. Meanwhile, organic molecules diffuse to the aqueous solutions. Component densities of C, O, K^+ and Cl^- in KCl solution and each organic solvent are shown in Figure 3-3, where the density distribution of each ion against Z direction was calculated by counting the number of averaged ion in every divided cell. Although the density distribution should be estimated under an equilibrium state, the interfacial structure was investigated under a non-equilibrium state because the structure slowly changed. The oscillations of density profiles in the interfacial zone have been observed as well as the miscible properties between aqueous solutions and organic solvents. Our previous experiments showed that the difference of mutual solubility to water was dependent on the type of organic solvent.[22] It turned out that water transported into an organic solvent side because the electric conductance increased in organic solvent side as time passes. The diffusion of water into 2-butanone occurred immediately compared to others since the electric conductance of 2-butanone initially valued high.

Focusing on the interfacial structure, the density profiles of 1-butanol had distinct peaks in interfacial area and these peaks came from BH, BO, C4, C3, C2 and C1 in order from water to 1-butanol side. To grasp the diffusion mechanism across the interface between aqueous solution and organic solvent, the distribution of cosα was calculated, where α is defined as an angle with organic molecules to unit vector Z_u in the Z direction as depicted in Figure 3-4.[23,24] Figure 3-5 shows the orientation distribution of each organic solvent. The principal direction of organic molecules for 1-butanol, 2-methyl-1-propanol and 2-butanol was decentralized by averaging orientation of organic molecules, and their hydroxyl group did not orient to aqueous phase side. In contrast, significant proportion of carbonyl group in 2-butanone oriented to the aqueous phase side as shown in Fig. 3-5 (d). Our previous results revealed that the molecular orientation to the interface occurred even at the interface between organic solvent and water, where solute ions are not included.[1] In the present simulations, the molecular orientation at interface showed difference of the type of organic solvent. The orientation of solvents near the interface and the existence of solute ions in aqueous solution affect the mutual diffusion of water and organic solvent. Li et al. experimentally clarified that the amount of mutual transfer between water and organic solvent decreased as the addition of solute ions increased in aqueous solutions.[25] The mutual diffusion would be prevented by the precipitation effect at the interface because KCl solutions reach saturation. Furthermore, the presence of ion at the aqueous/organic interface disturbs the structure of interfacial water and organic molecules.[26]

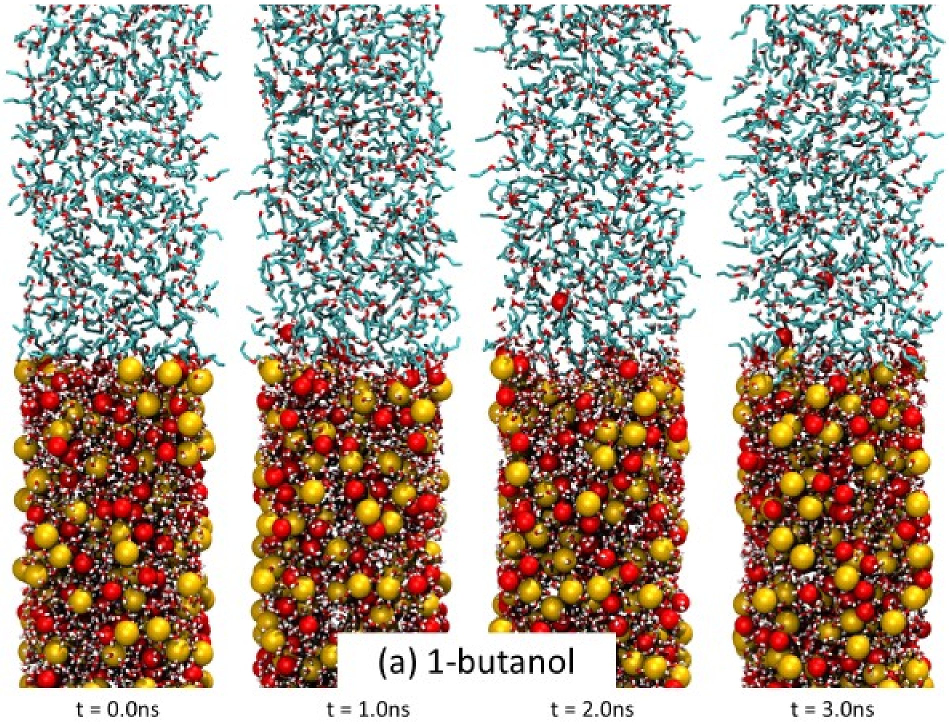
(a) 1-butanol
t = 0.0ns
t = 1.0ns
t = 2.0ns
t = 3.0ns

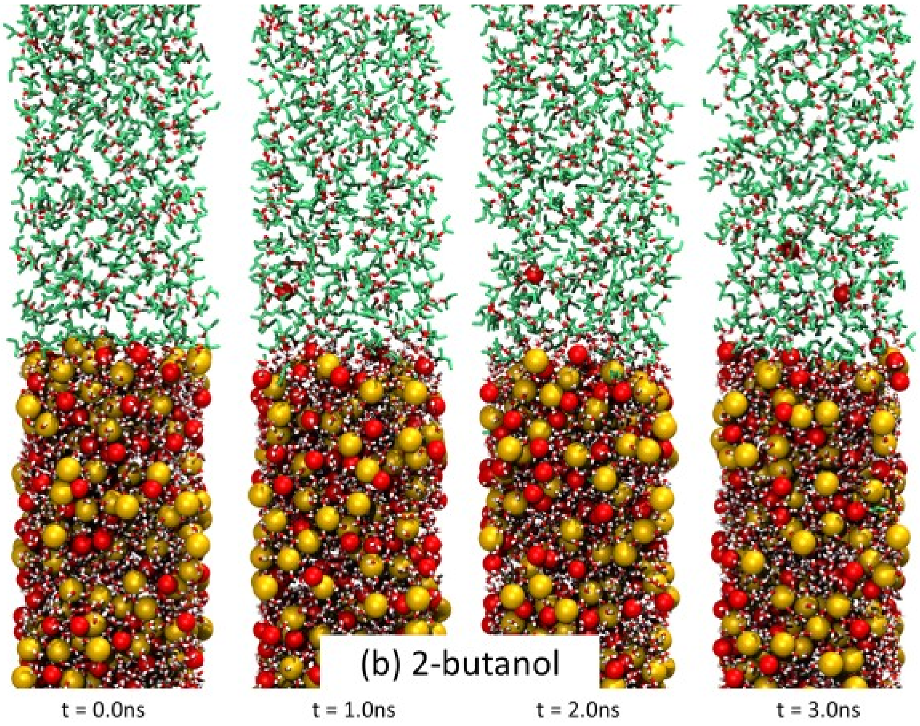
(b) 2-butanol
t = 0.0ns
t = 1.0ns
t = 2.0ns
t = 3.0ns

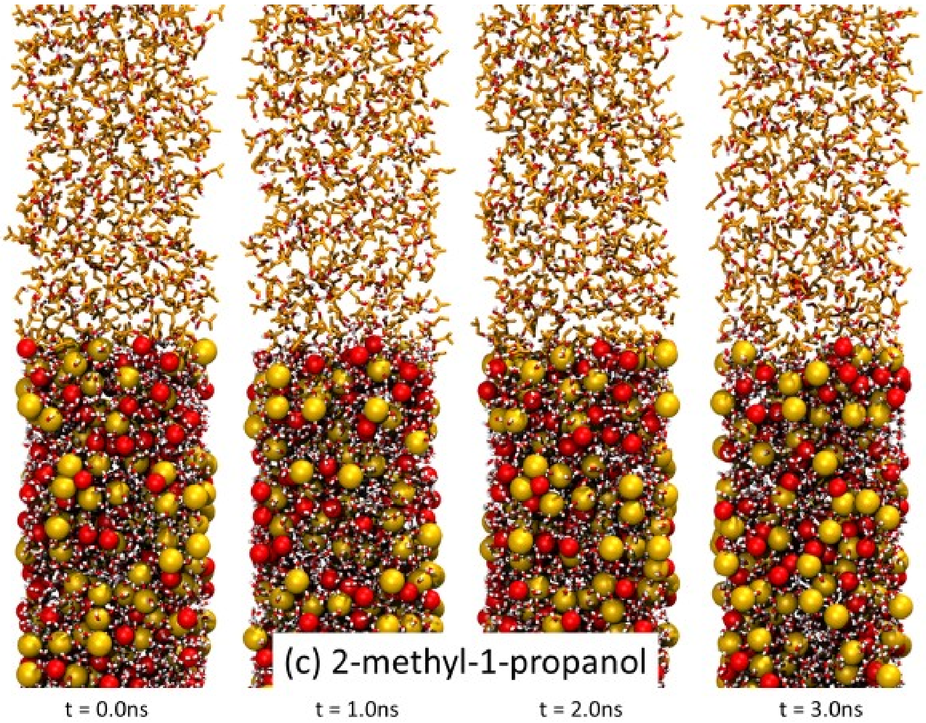

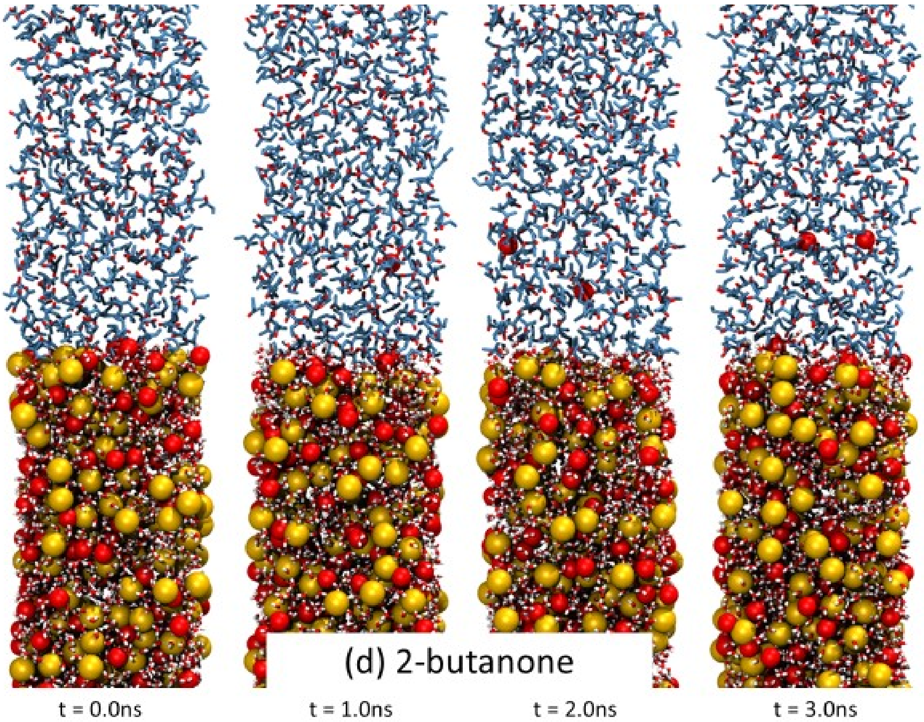

Fig. 3-2 (a) Time dependence of diffusion near interface between KCl solution and organic solvent. (a)1-butanol, (b)2-butanol, (c) 2-methyl-1-propanol, (d) 2-butanone.

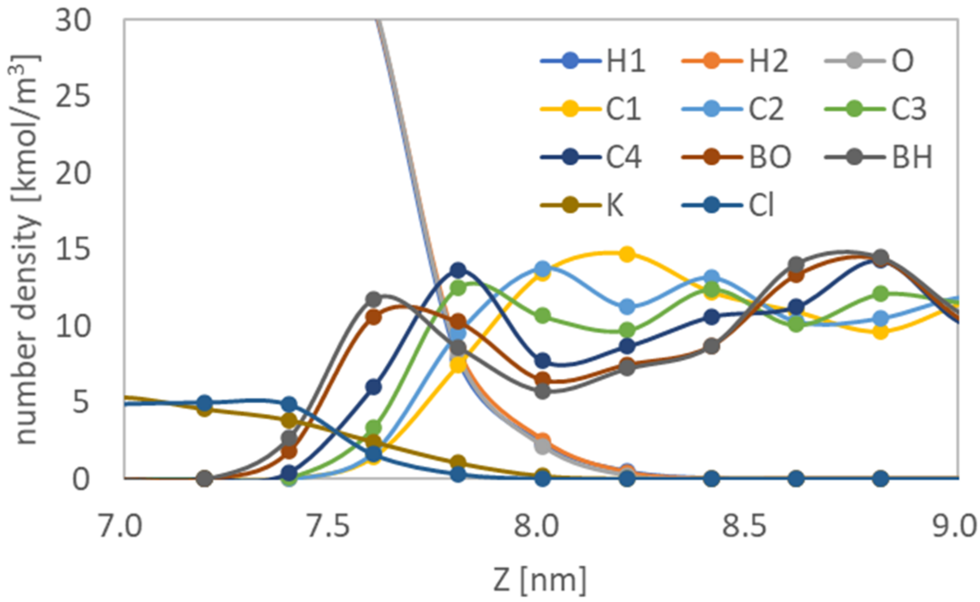

(a) 1-butanol

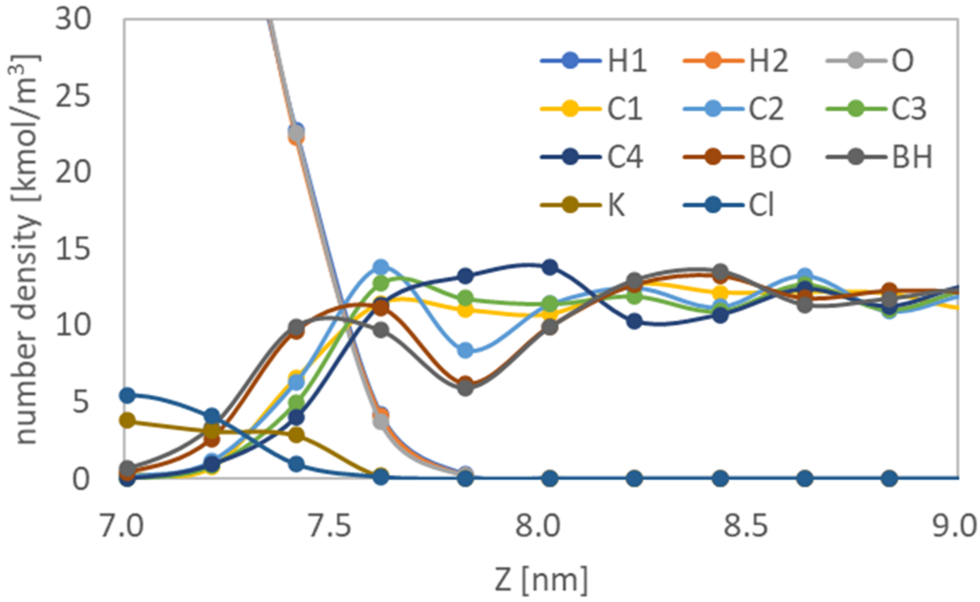

(b) 2-butanol

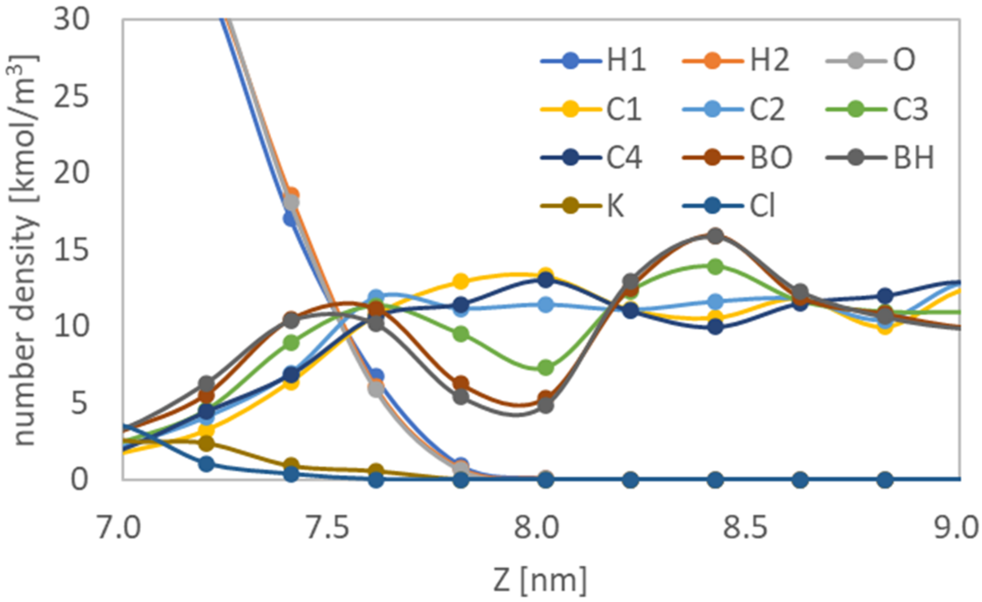

(c) 2-methy-1-propanol

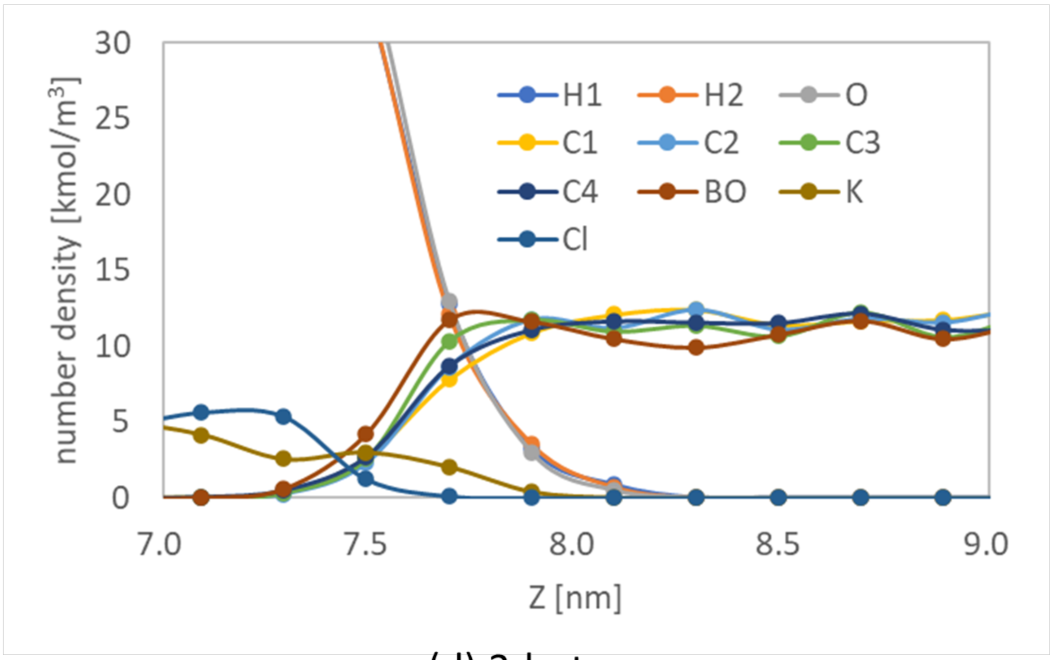

(d) 2-butanone

Fig. 3-3 Number densities of each site in KCl solution/organic solvents. Different C in organic molecules is numbered by index of C. H and O in water and in organic molecules are expressed by H1, H2, O (water), BH and BO (organic solvent), respectively.

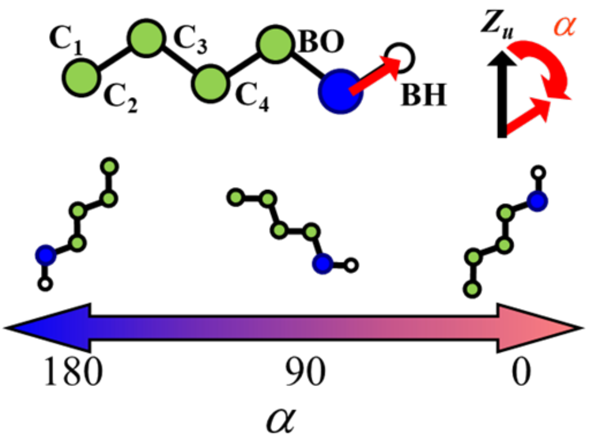

(a) 1-butanol, 2-butanol, 2-methyl-1-propanol

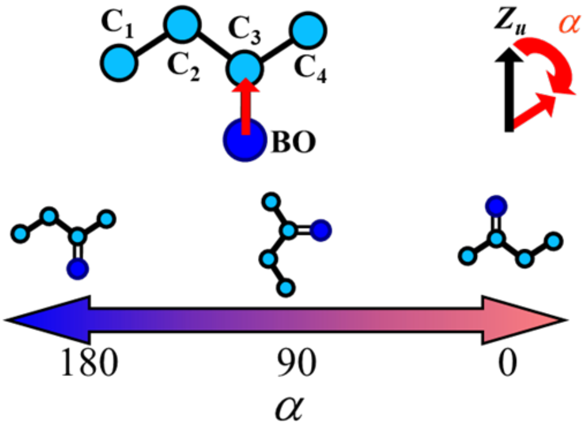

(b) 2-butanone

Fig. 3-4 Definition related to orientation of organic solvent against interface. (a) 1-butanol, 2-butanol, 2-methyl-1-propanol, (b) 2-butanone.

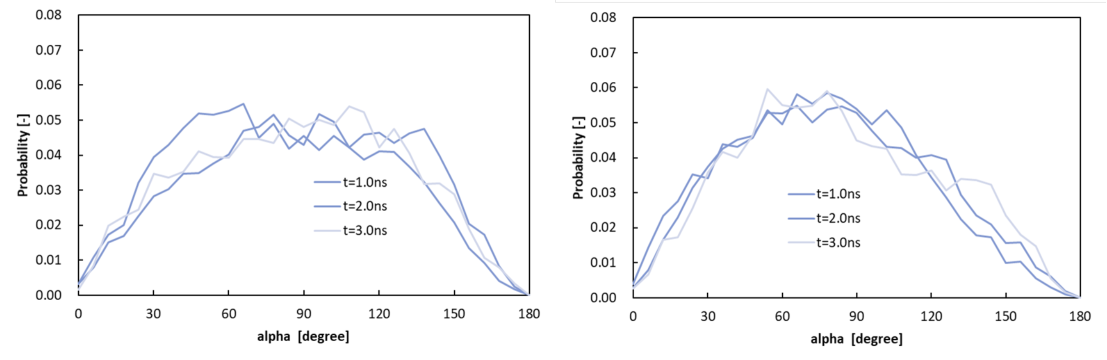

(a) 1-butanol

(b) 2-butanol

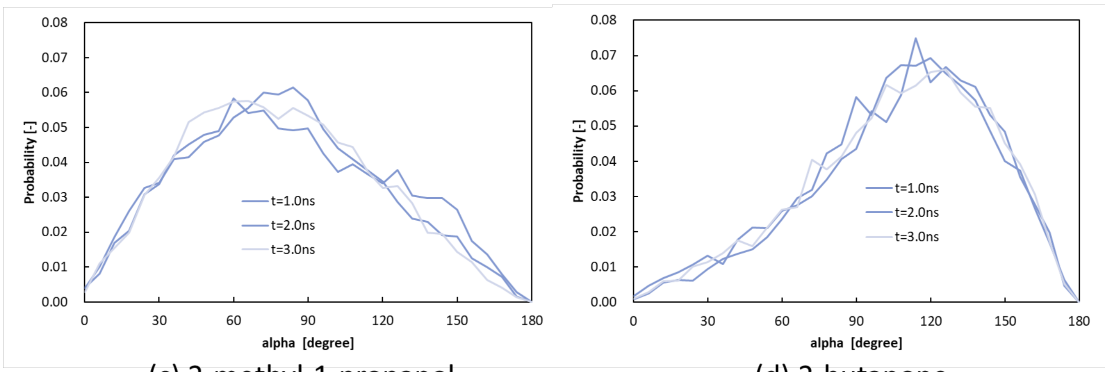

(c) 2-methyl-1-propanol

(d) 2-butanone

Fig. 3-5 Distributions of electric dipole as a function of α, where α is the angle between dipole moment of OH in hydroxyl group/OC in carbonyl group and unit vector of Z axis.

3.3.2 Coordination number of organic solvents around a water molecule

The mutual diffusion was quantitatively evaluated by calculating the coordination number of organic solvents (O_o) around a water molecule in the organic solvent or water molecules (O_W) around an organic solvent in the KCl solution. Figure 3-6 shows time evolutions of number of O_o (oxygen in organic molecules) coordinating to O_w (oxygen in water) in KCl solution/1-butanol/ 2-butanol/ 2-methyl-1-propanol and 2-butanone systems. Figure 3-7 shows time evolutions of number of O_w coordinating to O_o in KCl solution/1-butanol,/ 2-butanol,/ 2-methyl-1-propanol and 2-butanone systems. The coordination number is defined by the number of O_o of organic solvent around O_w

of water within the first minimum peak in radial distribution function of O_w–O_o from water/organic solvent mixture results simulated by the equilibrium molecular dynamics simulations.[27] The coordination numbers n_i (r_{min}) can be computed by the integration of the corresponding $g_{ij}(r)$ peak to the first minimum r_{min}:

$$n_i = 4\pi\rho_j \int_0^{r_{min}} g_{ij}(r) r^2 dr \tag{3-3}$$

where ρ_j denotes the number density of the j-th solvent component, and water is i and oxygen of organic molecule is j. In addition, n_i' are obtained in each divided cell by averaging every 20 ps. The coordination number gradually increases with contact time, and the interfacial boundary between KCl aqueous solutions and organic solvent fluctuates because the mutual diffusion region of two solvents extends near the interface. The mutual diffusion across the interface between KCl aqueous solutions and 2-butanone is formed by a different mechanism. The transfer of water molecules to 2-butanone phase was more difficult than that of any solvents. The displacement of organic solvents to aqueous phase similarly reduces at the interface between 2-butanone and KCl aqueous solution because the diffusion of the water molecules to 2-butanone phase and the 2-butanone molecules to the water phase simultaneously take places. We compared the force in the vicinity of interface between 1-butanol and KCl solution with that of the interface near 2-butanone and KCl solution because 1-butanol, 2-butanol and 2-methyl-1-propanol basically show the similar behavior near the interface.

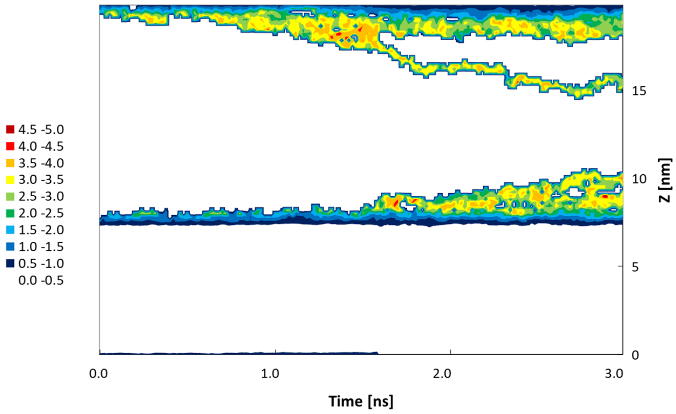

(a) 1-butanol

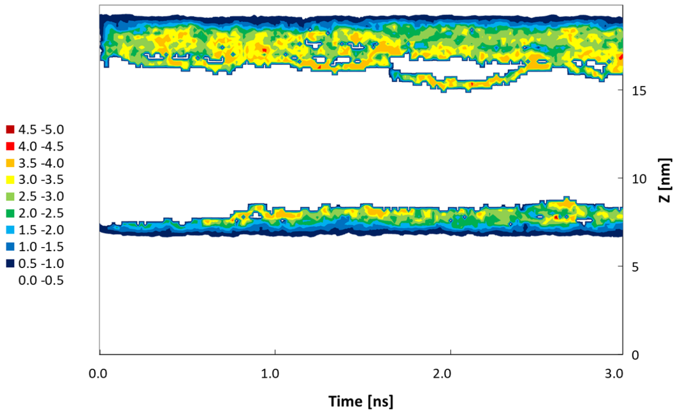

(b) 2-butanol

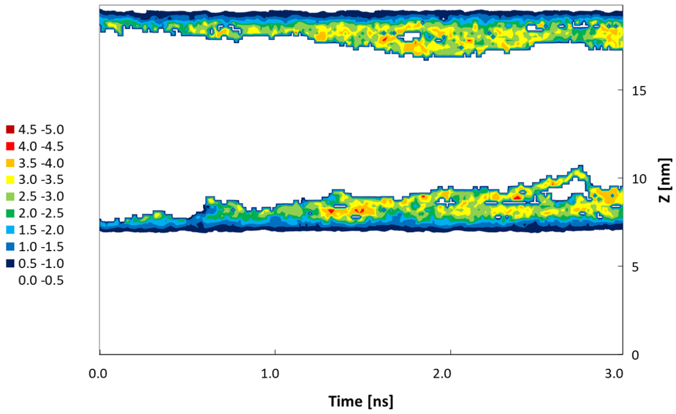

(c) 2-methyl-1-propanol

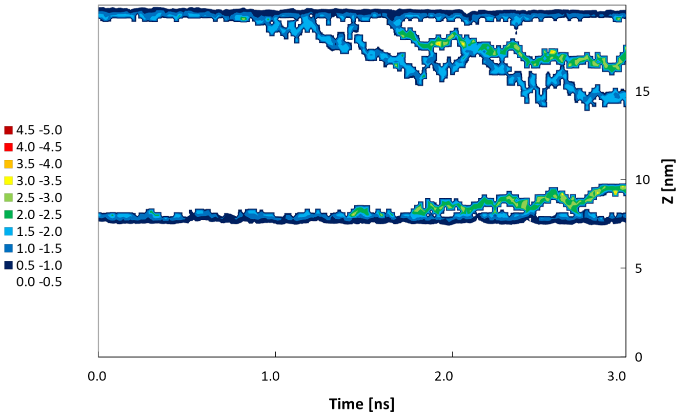

(d) 2-butanone

Fig. 3-6 Time evolutions of number of O_o (oxygen in organic molecules) coordinating to O_w (oxygen in water) in KCl solution/1-butanol,/2-butanol,/2-methyl-1-propanol and/2-butanone systems.

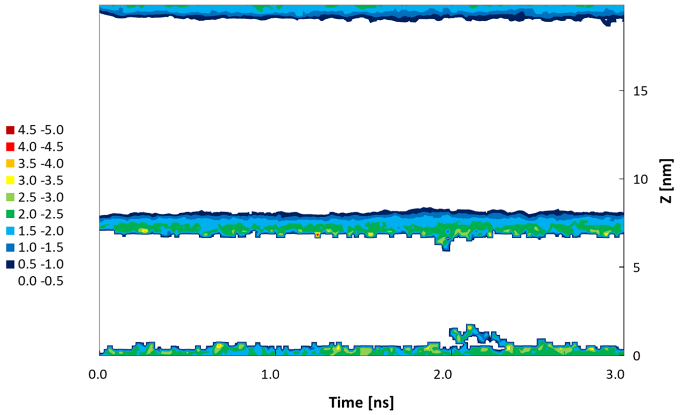

(a) 1-butanol

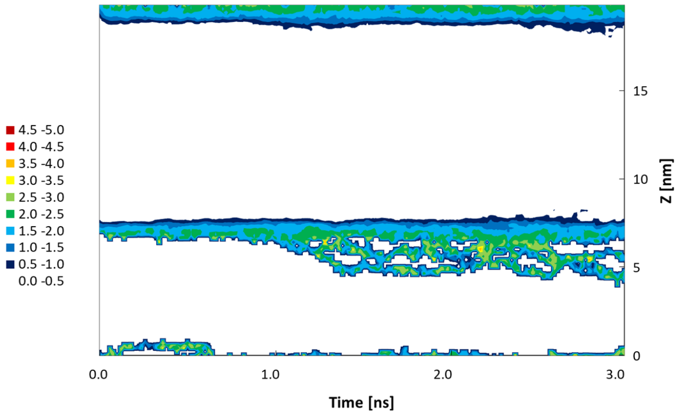

(b) 2-butanol

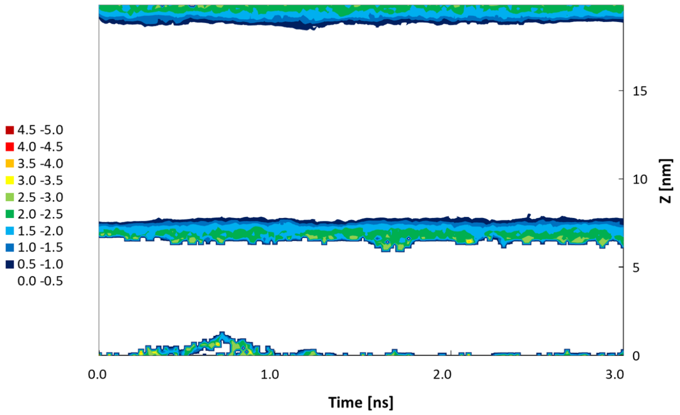

(c) 2-methyl-1-propanol

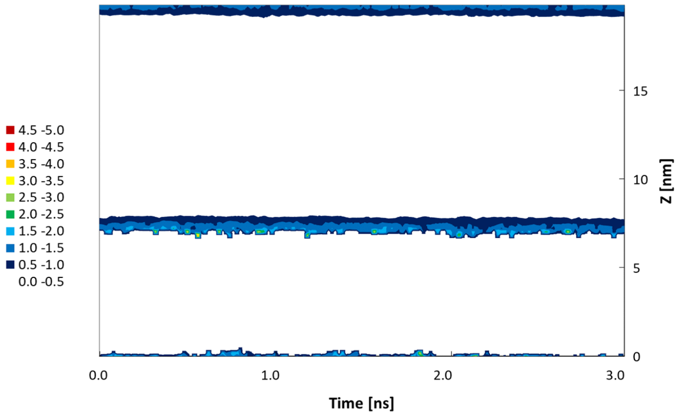

(d) 2-butanone

Fig. 3-7 Time evolutions of number of O_w coordinating to O_o in KCl solution/1-butanol,/2- butanol,/2-methyl-1-propanol and/2-butanone systems.

3.3.3 Force between hydroxyl group and water on the liquid–liquid interface

Figure 3-8 (a) provides time dependences of force between hydroxyl group and water molecule around KCl solution/1-butanol interface. The force of water molecules received from organic solvent in 2-butanone was about half than that in 1-butanol in spite of the fact that water molecules in 1-butanol or 2-butanone received a repulsive force from both hydroxyl and carbonyl groups. This is the root cause that the mutual diffusion between water and 2-butanone was unfavorable phenomena compared to that between water and 1-butanol. The snapshots of the interfacial structure are presented in

Figure 3-9. Water is depicted as molecular surface as function of VMD[28] to show the schematic liquid–liquid interface. And any atoms without O-H of 1-butanol and O=C of 2-butanone are not shown to avoid ambiguity. The mutual diffusion between aqueous solution and organic solvents except for 2-butanone easily takes place from a viewpoint of steric structure. It is difficult to diffuse mutually between aqueous solution and 2-butanone by the effect of orientation of organic solvents to water in the interfacial plane. The attractive force between water and organic solvents was screened with increasing distance from interface since the 2-butanone organized near the interface. This strong configuration in the interfacial region shows the diffusional resistance for steric constraint. These phenomena are in agreement with the tendency supposed from the value of the mutual solubility curve for the relationship between water and each organic solvent on equilibrium state.[29]

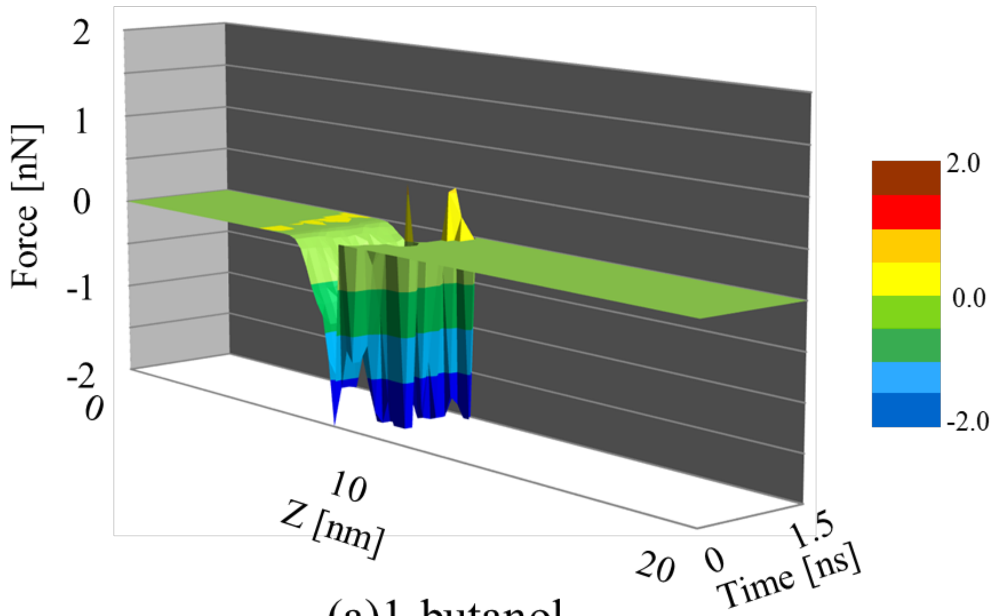

(a)1-butanol

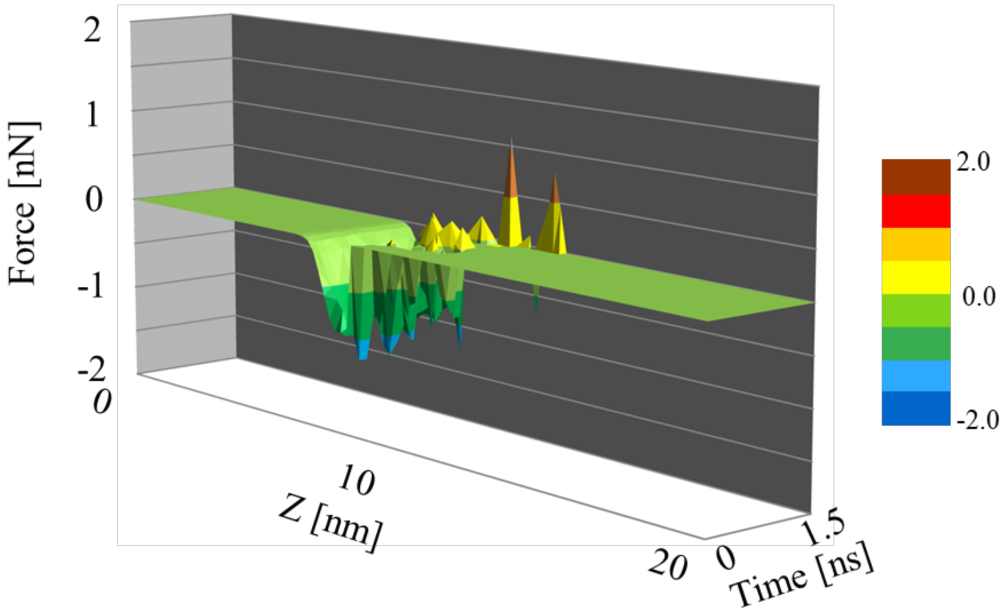

(b) 2-butanone

Fig. 3-8 Time dependences of force between hydroxyl group and water molecule around KCl solution/1-butanol interface and carbonyl group and water molecule around KCl solution/2-butanone interface.

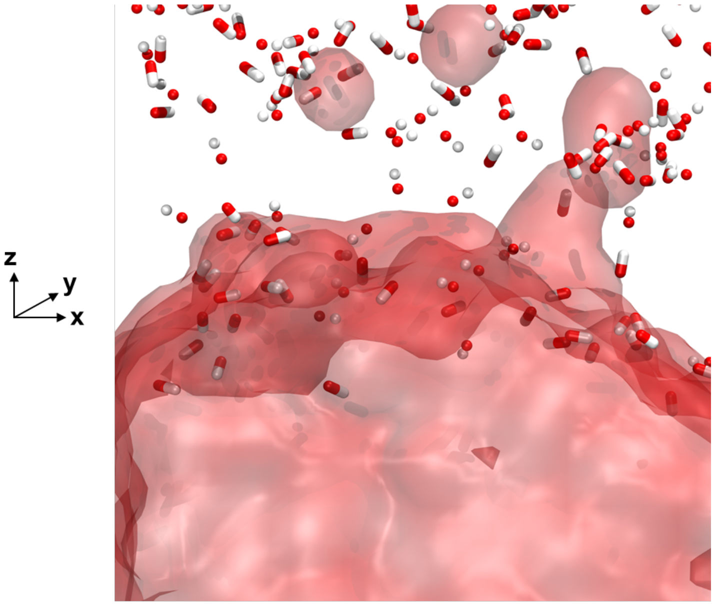

(a) KCl solution/1-butanol

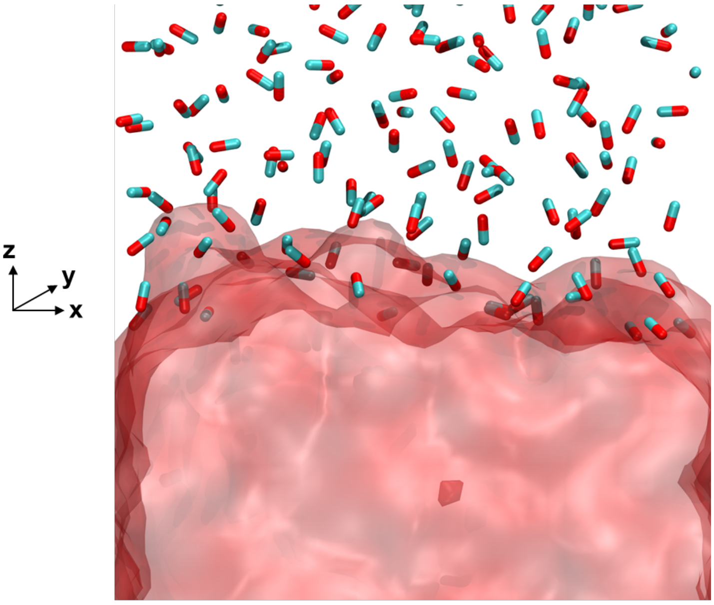

(a) KCl solution/2-butanone

Fig. 3-9 Snapshots of the interfacial structure (a) KCl solution/1-butanol, (b) KCl solution/2-butanone. Water as depicted as molecular surface as function of VMD. Without O-H of 1-butanol and O=C of 2-butanone are not shown to avoid ambiguity.

3.3.4 Clustering behavior affected by different organic solvent

The difference of mechanism for mutual diffusion would affect the particle generation in the interfacial zone. The previous results indicated that water molecules were partitioned into the solution phase and also organic molecules into the organic phase as the amount of addition of the salt increased.[25] We simulated the mutual diffusion under non-equilibrium state after KCl solution contacted with organic phase. The mutual diffusion was obstructed by the salting-out effect as well as the state of equilibrium because the concentration of KCl achieved to saturated solutions for both aqueous solution and organic solvent. The progress of diffusion in the organic phase results in a concentration gradient of water at the interface. Therefore, the coordination number of the solute ions around a water molecule decreases with an increasing degree of dehydration near the interface. The cluster was generated at the interface by associating with solute ions as ionic aggregation in supersaturated solutions. Eventually the nucleation formed as the cluster grew up. Figure 3-10 shows the change of the cluster size ratio with contact time. Cluster is defined as pairing ions within the first minimum peak of radial distribution function of their crystal state during 0.05 ns.[30] The ratio of cluster size changed with the type of solvent. Compared with KCl solution/1-butanol, the clusters generated more locally at the KCl solution/2-butanone interface. This indicates that concentration fluctuation of solute ions is enhanced by 2-butanone near the interface. In the previous experiments[21], the nucleation of KCl at the initial stage of operation time rapidly increased on the liquid–liquid interface. This is attributed to the speed of the dehydration in the mutual diffusion in the interfacial region. It means that the hydration force between K^+ and water molecule is weak. These results revealed that the difference of cluster formation depends on the type of organic solvent.

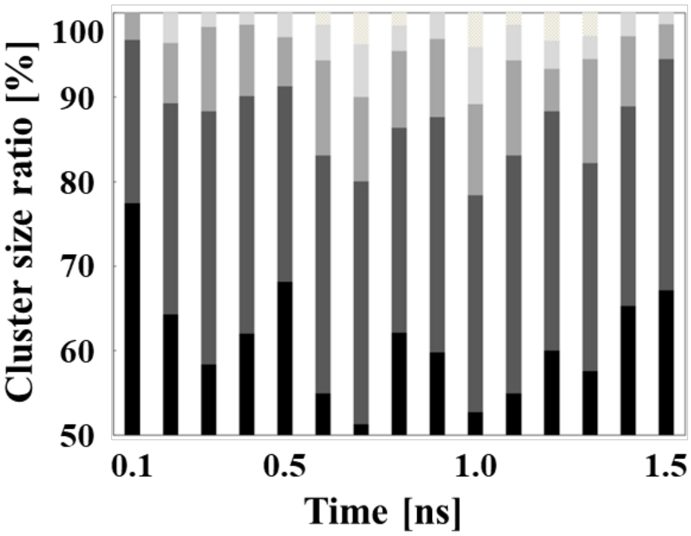

(a) KCl sol. / 1-butanol

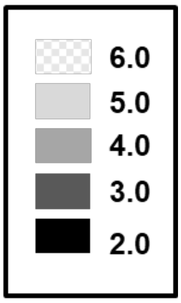

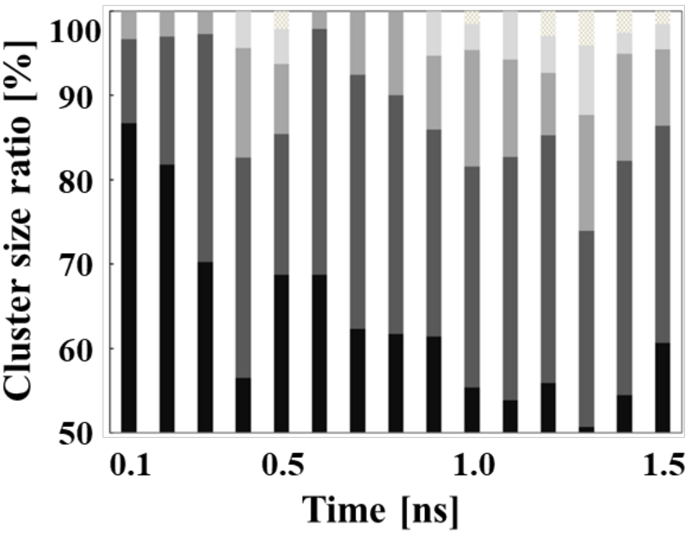

(b) KCl sol. / 2-butanone

Fig. 3-10 Time dependences of cluster size ratio in solution/organic solvent systems. The cluster size is expressed as the number of ions in a cluster.

3.4 Conclusion

Non-equilibrium MD simulations were performed to investigate the effect of organic solvent on the mutual diffusion and ionic behavior near the liquid–liquid interface between KCl aqueous solution and organic solvent (1-butanol, 2-butanol, 2-methyl-1-propanol and 2-butanone). The type of organic solvents affects the mutual diffusion of water and organic solvent from a viewpoint of steric structure. Especially the orientation of 2-butanone solvents to water at the interfacial region obstructs the mutual diffusion of solvent molecules. This difference originates in the ionic force received from water and organic solvent. The difference of mutual diffusion mechanism would affect the particle generation at the interfacial region. Compared with KCl solution/1-butanol, the clusters generated more locally at the KCl solution/2-butanone interface. This indicates that concentration fluctuation of solute ions is enhanced by 2-butanone near the interface.

*This chapter was reproduced and modified from [*J. Mol. Liq.,* 2014, **197**, 243–250], with permission from Elsevier.

References

[1] A. Kitayama, S. Yamanaka, K. Kadota, A. Shimosaka, Y. Shirakawa and J. Hidaka, *J. Chem. Phys.*, 2009, **131**, 174707

[2] M. Mirmehrabi and S. Rohani, *J Pharma Sci*. 2005, **94**, 7, 1560-1576

[3] H. J. C. Berendnsen, J. R. Grigera and T. P. Straatsma, *J. Phys. Chem.*, 1987, **91**, 6269–6271

[4] B. Chen, J. J. Potoff, and J. I. Siepmann, *J. Phys. Chem. B*, 2001, **105**, 15, 3093-3104

[5] J. M. Stubbs, J. J. Potoff and J. I. Siepmann, *J. Phys. Chem. B*, 2004, 108, 17596–17605

[6] J. P. Ryckaert, G. Ciccotti and H. J. C. Berendsen, *J. Comput. Phys.*, 1977, **23**, 327–341

[7] H. C. Andersen, *J. Comp. Phys.*, 1983, **52**, 1, 24-34

[8] I. S. Joung and T. E. Cheatham, *J. Phys. Chem. B*, 2008, **112**, 9020–9041

[9] M. P. Allen and D. J. Tildesley, *Computer Simulation of Liquids*, Oxford University Press, Oxford, 1987

[10] S. L. Outcalt, A. Laesecke and T. J. Fortin, *J. Mol. Liq.*, 2010, **151**, 50–59

[11] A. Rodrı´guez, J. Canosa and J. Tojo, *J. Chem. Eng. Data*, 2001, **46**, 1476-1486

[12] Y. Chabouni and F. Amireche, *J. Chem. Eng. Data*, 2020, **65**, 1679−1694

[13] R. A. Clará, A. C. G. Marigliano, and H. N. Sólimo, *J. Chem. Eng. Data*, 2006, **51**, 1473-1478

[14] A. Kitayama, S. Yamanaka, K. Kadota, Y. Shirakawa, A. Shimosaka and J. Hidaka, *J. Chem. Eng. Jpn.*, 2009, **42**, 346–350

[15] P. A. Fernandes, M.N.D.S. Cordeiro, J.A.N.F. Gomes, *J. Phys. Chem. B*, 1999, **103**, 6290–6299

[16] L. V. Woodcock, *Chem. Phys. Lett.*, 1971, **10**, 257–261

[17] L. Verlet, *Phys. Rev.*, 1967, **159**, 98–103

[18] D. Fincham, *Mol. Simul.*, 1994, **13**, 1–9

[19] H. B. Wang, E. Carlson, D. Henderson and R.L. Rowley, *Mol. Simul.*, 2003, **29**, 777–785

[20] K. Kadota, T. Wake, K. Gonda, A. Kitayama, Y. Tozuka, A. Shimosaka, Y. Shirakawa, and J. Hidaka, *J. Mol. Liq.*, 2014, **197**, 243-250

[21] K. Kadota, Y. Shirakawa, I. Matsumoto, A. Shimosaka and J. Hidaka, *Adv. Powder Technol.*, 2007, **18**, 775–785

[22] K. Kadota, Y. Shirakawa, I. Matsumoto, H. Tamura, A. Shimosaka and J. Hidaka, *Int. J. Phys. Sci.*, 2013, **1**, 27–38.

[23] J. Wang, A.G. Kalinichev and R.J. Kirkpatrick, *Geochim. Cosmochim. Acta*, 2004, **68**, 16, 3351–3365

[24] H. Shinto, T. Sakakibara and K. Higashitani, *J. Phys. Chem. B*, 1998, **102**, 1974–1981,

[25] Z. Li, Y. Tang, Y. Liu and Y. Li, *Fluid Phase Equilib.*, 1995, **103**, 143–153

[26] E. S. Shamay and G. L. Richmond, *J. Phys. Chem. C*, 2010, **114**, 12590–12597

[27] J. L. Rivera, C. Mccabe and P. T. Cumming, *Phys. Rev. E*, 2003, **67**, 011603, 1–10

[28] W. Humphrey, A. Dalke and K. Schulten, J. *Molec. Graphics,* 1996, **14**, 1, 33-38

[29] A. F. M. Barton, *Alcohols with Water Solubility Data Series*, Pergamon Press, New York, 1984.

[30] S. A. Hassan, *J. Phys. Chem. B*, 2008, **112**, 10573–10584

Chapter 4

Clustering of glycine zwitterion in aqueous solution with ethanol as anti-solvent crystallization system

4.1 Introduction

Non-equilibrium behavior of solute and solvent considering intrinsic property and interaction which come from molecules are investigated at molecular level as critical aspect to determine the anti-solvent crystallization mechanism through Chapter 2 and 3. One of the typical issue during process design of crystallization in pharmaceutical industry is unexpected polymorph originated from a change of supersaturation. To investigate the mechanism of polymorph determination during nucleation, Chapter 4 is described about the behavior of solvent and solute which has intramolecular structure as drug like molecule.

Considering a specific level of supersaturation, two nucleation theories are available: the classical nucleation theory (CNT)[1] and two-step nucleation theory (TNT)[2]. Two-step crystallization mechanism, in which nucleation occurs via an amorphous precursor, has been discussed compared with the common CNT during the last decade.[3] In CNT, the nucleation process is assumed to be one step in which a crystal nucleus is generated as it was once a high concentration region of solute molecules exceeding a free energy barrier caused by energy fluctuation. Based on CNT, TNT assumes that there is an additional induction phase forward to form a non-crystalline cluster, and the cluster must overcome the second energy barrier to rearrange into a stable ordered crystalline nucleus. First, solute molecules aggregated as an unstable state, and the solvent surrounding the solutes was removed. Next, the solute structures were simultaneously arranged from disordered aggregates to the crystal one. When the concentration of solutes rapidly increased, the solvent molecules could not be dissociated from the solute, and both the solute and the solvent were pushed together into a confined space. These highly concentrated droplets, containing solutes and solvents that exceed the saturation solubility, were formed in the solvent in the liquid–liquid phase separation (LLPS). The structure ordering provided the thermal stable state for the crystal. In both small and large molecules, LLPS was confirmed in several cases.[4-6] The understanding of the LLPS is key for predicting and optimising conditions for multi-interacted system, such as protein crystallization.

Lutsko et al., considered the LLPS in a microscopic view and reported that the numerical density functional theory of Lennard–Jones (LJ) potential liquids could explain their LLPS and nucleation phenomena corresponding to the TNT.[7] Maeda et al. investigated the behaviour of LJ liquids as a pseudo-anti-solvent system through a classical molecular dynamics (MD) simulation, concluding that such phenomena occurred at molecular level.[8] These works are valuable in understanding the mechanism of LLPS and the effect of the component ratio of an anti-solvent during crystallization. Moreover, their system provides a simple approximation. Molecular packing is accelerated with different ε_{ij} well depth of LJ parameters and an increase in the anti-solvent ratio. These findings suggest that molecular dynamics simulation can shed light on the microenvironment of crystallization and provide insights and understanding of the anti-solvent process. However, few studies have been conducted on an anti-solvent system with a configurational molecule, which has a different intermolecular interaction site. In addition, to the best of our knowledge, little research has been conducted on LLPS for anti-solvent crystallization at a microscopic level.

In this Chapter 4, the simplest amino acid, glycine, was selected as the model compound of the solute. Glycine exists as a zwitterion (NH_3^+–CH_2–COO^-) in normal water as the amphoteric (acid-based) properties from the amino and carboxyl functional groups.[9] Their nucleation and crystal growth behavior, particularly their polymorphs obtained through crystallization, have been investigated for decades.[10-12] For example, discussions on whether glycine forms the cyclic, hydrogen-bonded dimer in water that causes selective crystallization of the α form are available in the literature regarding pH-dependency and the ionic effect on the polymorphism of glycine. Their thermodynamic stability is known in the order of γ, α and β-glycine polymorphs.[13] However, the charge and related hydrogen bonding play a critical role between the molecules in crystallization, thereby complicating the process, which is to be expected of such a simple amino acid structure.

Myerson experimentally observed the concentration dependant diffusivity of glycine molecules in the aqueous solution[14,15] and this indicated the existence of liquid-like clusters and is evidence of TNT. The condition was supersaturated, and it appeared that multiple interaction sites among glycine molecules provided a thermodynamic stable state in the solution as their strong coulomb and hydrogen bond interactions were the key feature during glycine polymorphic selection. Once the system became highly concentrated and dense, freedom of conformational change reduced, and the generation of the crystal structure through molecular interactions became prohibited. Consequently, no crystallization was observed, and even the system had a much larger degree of supersaturation, S (S = 2.7). These findings draw attention to the LLPS in glycine crystallization because of the phenomena to bridge supersaturation state and nucleation which is described in TNT. Hughes et al., performed exploiting the complementarity of the different techniques (solid state-NMR, X-ray, MD simulation and small angle scattering) in order to probe different stages of crystallization processes of glycine clustering. From the small angle neutron scattering, it was suggested that the molecular aggregates present during the early stages of the crystallization process which has larger size than a few molecules has relatively broad distributions of both size and shape, and moreover that the nature of these distributions may also be time-dependent.[16]

Ethanol was also selected as an anti-solvent when it mixed into the glycine aqueous solution as a typical anti-solvent. Zheng et al. reported that the glycine solubility change depends on the concentration of ethanol in the aqueous system.[17] The enthalpies of solvation of glycine monotonically decrease to 0.2 of mole fractions in aqueous solutions of ethanol as listed in Table 4-1.[18] However, glycine-ethanol interactions sharply change and become reversed at higher ethanol concentrations which may happen at local mixing area.

At the beginning of the anti-solvent crystallization, the anti-solvent and solute–solvent came into contact and became a mixture via multi-diffusion. We selected the liquid–liquid interface of glycine aqueous and ethanol as a meaningful system to capture the clustering of glycine/phase separation, which was then analysed via classical MD simulation. Experimentally, the system provided the α, β and γ glycine as anti-solvent crystallizations.[19,20] This provided the study with detailed information of anti-solvent crystallization mechanism at the molecular level from the trajectory data through the multi-diffusion of solvents, which increased supersaturation. Scale limitations of the simulation system did not require consideration of the crystal growth owing to the short time frame compared with the experimental approach. The behavior of glycine as a solute was assumed to change by the diffusion between the good solvent and the anti-solvent.

As mentioned, there are significant works about each molecules and anti-solvent system and glycine crystallization as from bulk solution. However, few studies have been conducted on an anti-solvent system with a configurational molecule, which has a different intermolecular interaction site at a microscopic level. In addition, to the best of our knowledge, little research has been conducted on LLPS for anti-solvent crystallization. Thus, we discuss both the dehydration and structural ordering of solutes during nucleation in such anti-solvent system which has complexed interactions between solute and solvents with considering LLPS in this work. The analysis focuses on the clustering time progression, size, interaction among the solute–solvent molecules and dehydration as the indicator of the structure and behavior of LLPS related to the initial stage of nucleation.

Table 4-1 Enthalpy of solvation of glycine aqueous solution as bulk with different ethanol concentration

Ethanol mole fraction [-]	Enthalpy of solvation [kJ/mol]
0.0052	-121.45
0.0213	-118.99
0.0294	-118.37
0.0466	-116.86
0.0773	-115.27
0.1154	-115.10
0.2268	-115.77

4.2 Method

4.2.1. Simulation condition

Classical MD simulation was performed to investigate the dynamics of the solute and solvents at initial contact. The SPC/E was selected as it is one of the most common water models used in MD simulations.[21] In this study, a combination of the generalized AMBER force field (GAFF) and CNDO charge set, which was modified by Bushuev et al., has been selected as the model of glycine zwitterion ($H_3N–CH_2–CO_2$).[22] The model was implemented as the combination of forcefield and charge set which were well fitted to the transportation properties and their positive solvation enthalpy provided for glycine crystal growth on the crystal surface.[23] Ethanol was modelled with the TraPPE-United Atom (UA) model, which presented a phase equilibrium with water at a wider temperature range and was developed by Maerzke et al..[24] The nonbonded interactions were calculated using the LJ and Coulomb potentials, including van der Waals (vdW) terms and electronic terms. Intramolecular interactions of each interaction site of the molecule were described according to the following equation:

$$U_{nonbonded}(r_{ij}) = 4\varepsilon_{ij}\left[\left(\frac{\sigma_{ij}}{r_{ij}}\right)^{12} - \left(\frac{\sigma_{ij}}{r_{ij}}\right)^{6}\right] + \frac{q_i q_j}{4\pi\varepsilon_0 r_{ij}} \tag{4-1}$$

where U, r_{ij}, ε_{ij}, σ_{ij}, q_i, q_j and ε_0 are potential energy by nonbonded interactions, the interaction site distance, the parameters for LJ potential dept, LJ diameter, partial charges and permittivity of vacuum, respectively. The ε_{ij} and σ_{ij} for different types of atoms were determined using the Lorentz–Berthelot combining rules.[25] Rigid bond lengths were used for bonded interactions. Bond angles and torsion angles of ethanol and glycine were treated using harmonic potential terms according to each force field form.

The glycine aqueous solution and ethanol were allocated to be opposite to each other along the Z-axis as cartesian coordinates, as shown in Figure 4-1. The processes of bringing the solutions to equilibrium were independently performed for 100 ps under the target temperature: 298.15 K via the T-scaling method.[26] The LJ parameters were truncated at 1.4 nm, and the Coulomb force was calculated through Ewald summation to achieve relative accuracy within 6.7×10^{-5} for energy conservation. The cell length was set to have enough distance between the interfaces in the periodic boundary system[27] and yielded liquid densities of the glycine aqueous solution and ethanol at 298.15 K.[28,29] Table 4-2 lists the number of each molecule and concentration of glycine according to the MD simulation system. The temperature was controlled to 298.15 K via ad hoc T-scaling at every time step as an NVT ensemble. The velocity-Verlet algorithm was used to integrate the equations of motion.[30] The all models were used in combination with the SHAKE and RATTLE algorithm to provide rigid bonds of molecules.[31,32], The trajectory data were stored every 1 ps and analysed for 5 ns throughout the total simulation time (t). The simulation of glycine zwitterions of bulk aqueous solution was equilibrated for 500 ps in the 3.20 × 3.20 × 8.06 nm cell as same as in Fig. 4-1 separately.

Table 4-2 List of classical molecular dynamics (MD) simulations for the system of glycine aqueous solution and ethanol

Initial state of glycine zwitterion aqueous solution	Number of molecules			Concentration of glycine aqueous solution (C) [mol kg^{-1}]
	Water	Glycine zwitterion	Ethanol	
Undersaturated	2400	127	1372	2.94
Saturated	2400	144	1372	3.33
Supersaturated	2400	161	1372	3.72

4.2.2. Analytical method

4.2.2.1 Visualization

All trajectory data were visualised via VMD[33] to discuss the molecular behavior of the simulation. Hydrogen bonds were also depicted using a VMD function.

4.2.2.2 Self-diffusion coefficient

The self-diffusion coefficient, *D*, was calculated from the long-time limit of the mean-square displacement according to Einstein's relationship:

$$D = \lim_{t\to\infty}\frac{1}{6t}\langle|\vec{r}(t) - \vec{r}(0)|^2\rangle \tag{4-2}$$

Where $\vec{r}(t)$ and $\vec{r}(0)$ represent the positions of the centre of mass of the molecule at times t and 0, respectively.

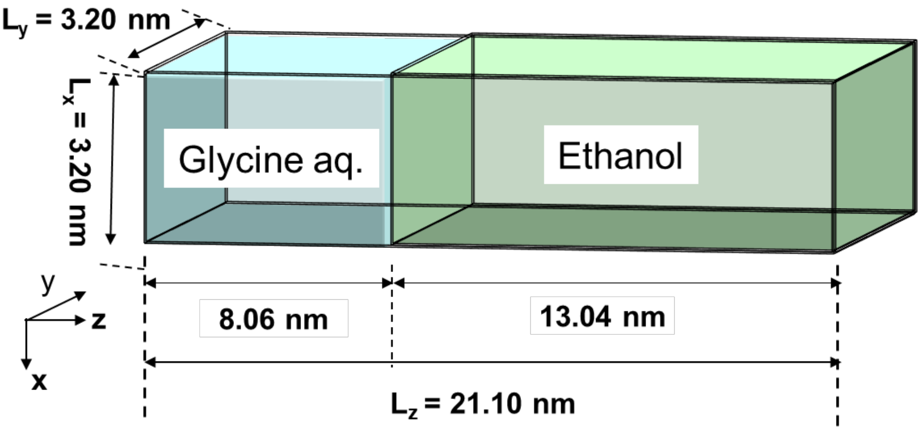

Fig. 4-1 Basic cell used in the classical molecular dynamics (MD) simulation for the binary system of the glycine aqueous solution at C = 3.33 mol kg^{-1} and ethanol (Cell length of Z axis, L_z was adjusted with each concentration of the glycine aqueous solution).

4.2.2.3 Cluster of glycine zwitterions

The cluster of glycine zwitterions is defined as follows. Based on radial distribution functions (RDFs), the distance criterion was set at 6 Å, where $g_{N\text{-}N}$ (r) showed the first negative peak with another zwitterion. The RDFs of the glycine zwitterion system as bulk aqueous solution are shown in Figure 4-2. To consider the lifetime of the glycine cluster, the threshold of a lifetime was set to 5 ps, maintaining the distance criteria mentioned in the literature, where the lifetime of hydrogen bonds was estimated to be ~1‑4 ps.[34] Semilog plots were used to highlight the existence of large size cluster.[35] The average angle (θ), between vectors connecting the carbon atoms ($H_2C \rightarrow CO_2$) in the glycine cluster was calculated which are frequently used for structural analysis of glycine.[22,36] Regarding hydrogen bonding, herein, as initial criteria, the maximum distance of 2.2 Å was used to define hydrogen bonding between the hydrogen atom connected to the nitrogen atom and the oxygen atom of the clustering glycine molecules. The angles of N–H···O were analysed following Hamad et al.'s work.[37] Angle distribution of the hydrogen bond between glycine–glycine zwitterions as bulk solution at C = 3.33 mol kg^{-1} is shown in Figure 4-3.

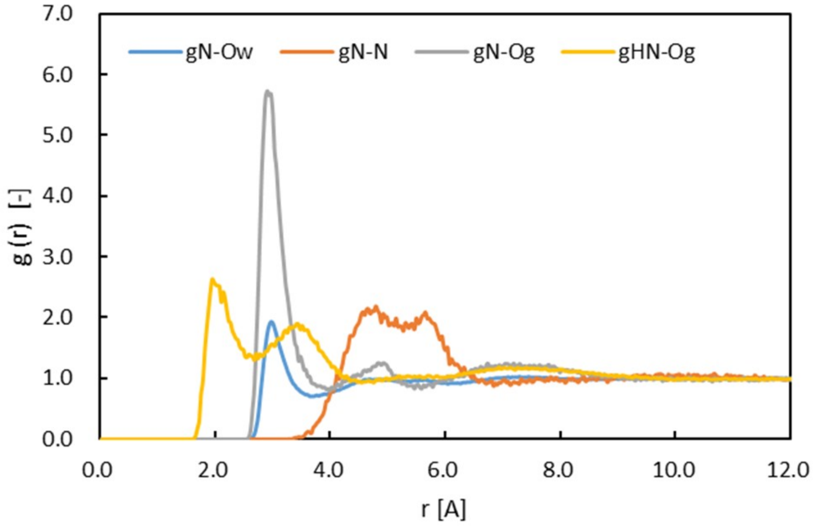

Fig. 4-2 Radial distribution function, g(r) of N (nitrogen) -O_w (oxygen of water), N-N, N-O_g (oxygen of glycine) and HN (hydrogen bonded to N) -O_g of glycine zwitterion aqueous solution at C = 3.33 mol kg^{-1}.

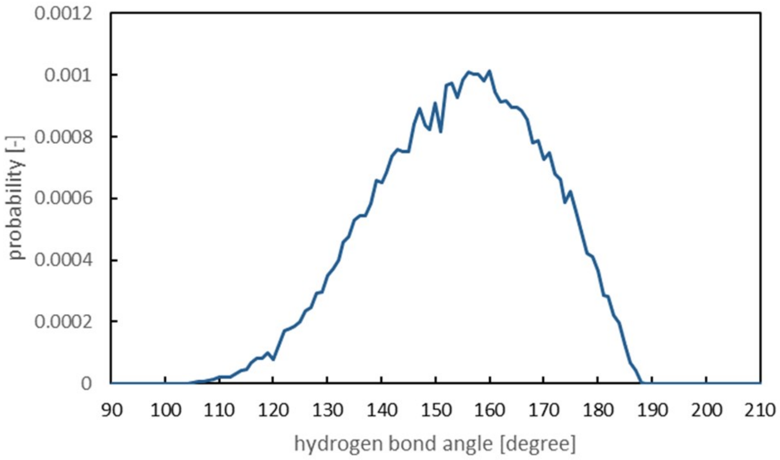

Fig. 4-3 Angle spectra of hydrogen bond (HN-N…O_g) of glycine-glycine cluster in C = 3.33 mol kg^{-1} glycine aqueous solution as bulk.

4.2.2.4 Coordination number of glycine zwitterion

The coordination number of glycine zwitterions was defined by the number of oxygen atoms (O_w) of water around the nitrogen atoms (N) of glycine. The hydration shell was estimated as the first negative peak of RDF of $g_{N\text{-}Ow}$ (r) at 3.6 Å from the bulk glycine aqueous simulation run (Fig. 4-2 shows the RDFs.), and the number of oxygen atoms (O_w) was integrated until the range to calculate the coordination number. The numbers were averaged every 20 ps and obtained for each slab by dividing the whole simulation cell into 100 slabs.

4.3 Results and discussion

4.3.1 Simulation validity

As the bulk system of glycine zwitterions in an aqueous solution, the diffusion coefficient was confirmed by their dependency on the solute concentration calculated for 0.5 ns. The diffusion coefficients and tendency on the glycine zwitterion concentration were in accordance with previous MD simulation and experimental values, as shown in Figure 4-4.[22,37,38] The self-diffusion coefficients were reduced according to the elevation of the glycine concentration of an aqueous solution for both of the values from the experiments and MD simulation. At a nearly saturated concentration (C = 3.33 mol kg^{-1}), the value constantly remained larger than 0.4×10^{-9} m^2 s^{-1} compared with the experiment. However, a discrepancy was observed in the literature, which could be managed as all values were on the same order of magnitude.[22,23,36] This work maintained sufficient accuracy to not aim for the quantitative accuracy of diffusivity.

The density profiles, which averaged at t = 0.0–0.1 ns for each molecule in the slab divided by 100 to the Z cell length, are shown in Figure 4-5 as the initial state of the whole system. The density of the glycine aqueous phase and the ethanol phase matched with experimental density[24,28] at the instant contact of the anti-solvent system.

Both density profiles showed a sigmoid curve, and the interface was assumed to be located at approximately Z = 8 nm of the system, as intended. Even for 0.1 ns, each molecule was moved opposite the phase, slightly after the contact. In the C = 3.72 mol kg^{-1} system, less multi-diffusion was confirmed compared with the C = 2.94 and 3.33 mol kg^{-1} system. This difference originated from different surface tensions of the solution, which are dependent on the glycine concentration,[39] even when the interface is not an equilibrated structure. The coordination number of the bulk glycine aqueous solution was estimated to be 3.88, and these values approached the experimental value of 3.0 ± 0.6[40].

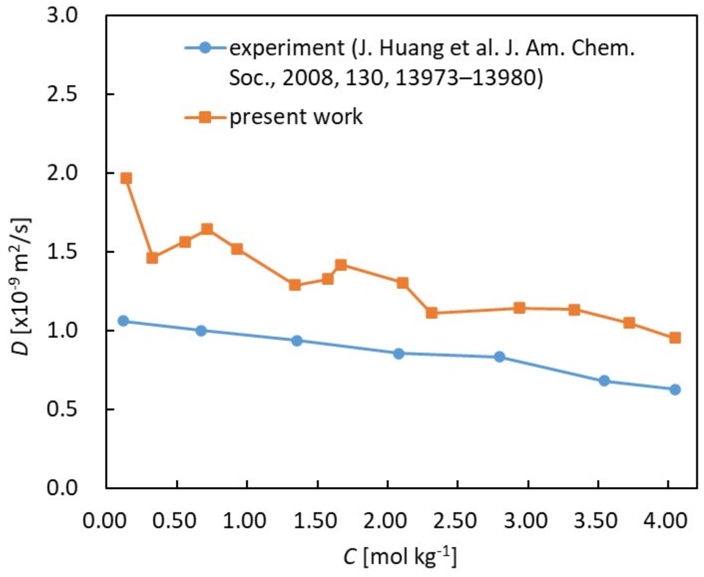

Fig. 4-4 Self-diffusion coefficient of glycine zwitterions in the aqueous solution with various solute concentrations.

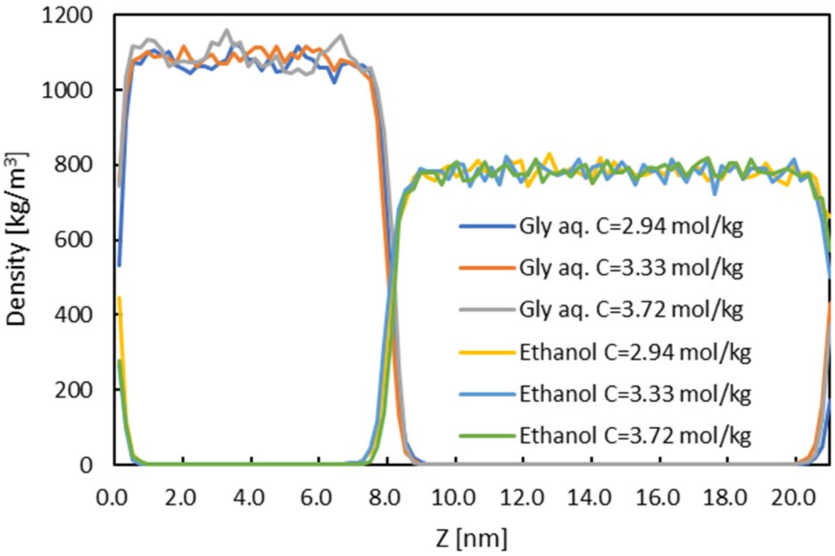

Fig. 4-5 Density profiles of different concentrations of the glycine aqueous solution and ethanol along the Z axis at t = 0.0–0.1 ns.

4.3.2 Time progression of the system

Figures 4-6 (a), (b) and (c) show snapshots of the of glycine zwitterion aqueous solution and ethanol system at t = 0.0, 2.5 and 5.0 ns each at C = 2.94, 3.33 and 3.72 mol kg^{-1} of glycine zwitterion aqueous solution respectively. Glycine was depicted basically as a zwitterion, and water and ethanol are illustrated as transparent surfaces of molecules. At t = 0.0 ns, glycine zwitterion molecules were spread in the aqueous phase without segregation. After t = 5.0 ns, glycine zwitterions had clearly aggregated in the aqueous phase with the progression of time, and finally, a large cluster can be observed at approximately Z = 2 nm in the snapshot. In addition, the glycine cluster can rarely be observed in the upper side of Z = 8 nm. This suggests that the reduction of the concentration due to the diffusion of glycine to the ethanol phase can be neglected when considering the crystallization in this time frame. The critical nucleus size of glycine in the aqueous solution was experimentally estimated by Kamano et al.,[41] and the value was 1.05 nm, which theoretically comprised 44.9 glycine molecules. According to the CNT, the aggregates, which were below this value, must be unstable and dissolved in the solution again.

However, Bushuev et al. reported that the mean lifetime of glycine clusters was 13.1 and 108.3 ps with the same forcefield of glycine based on their bulk MD simulation results.[22] Thus, the crystallization of glycine could potentially proceed through the formation of pre-nucleation clusters, which are thermodynamically stable solutes. The following section characterises each molecule and glycine zwitterion aggregates via mutual diffusion in such a rapid supersaturated region.

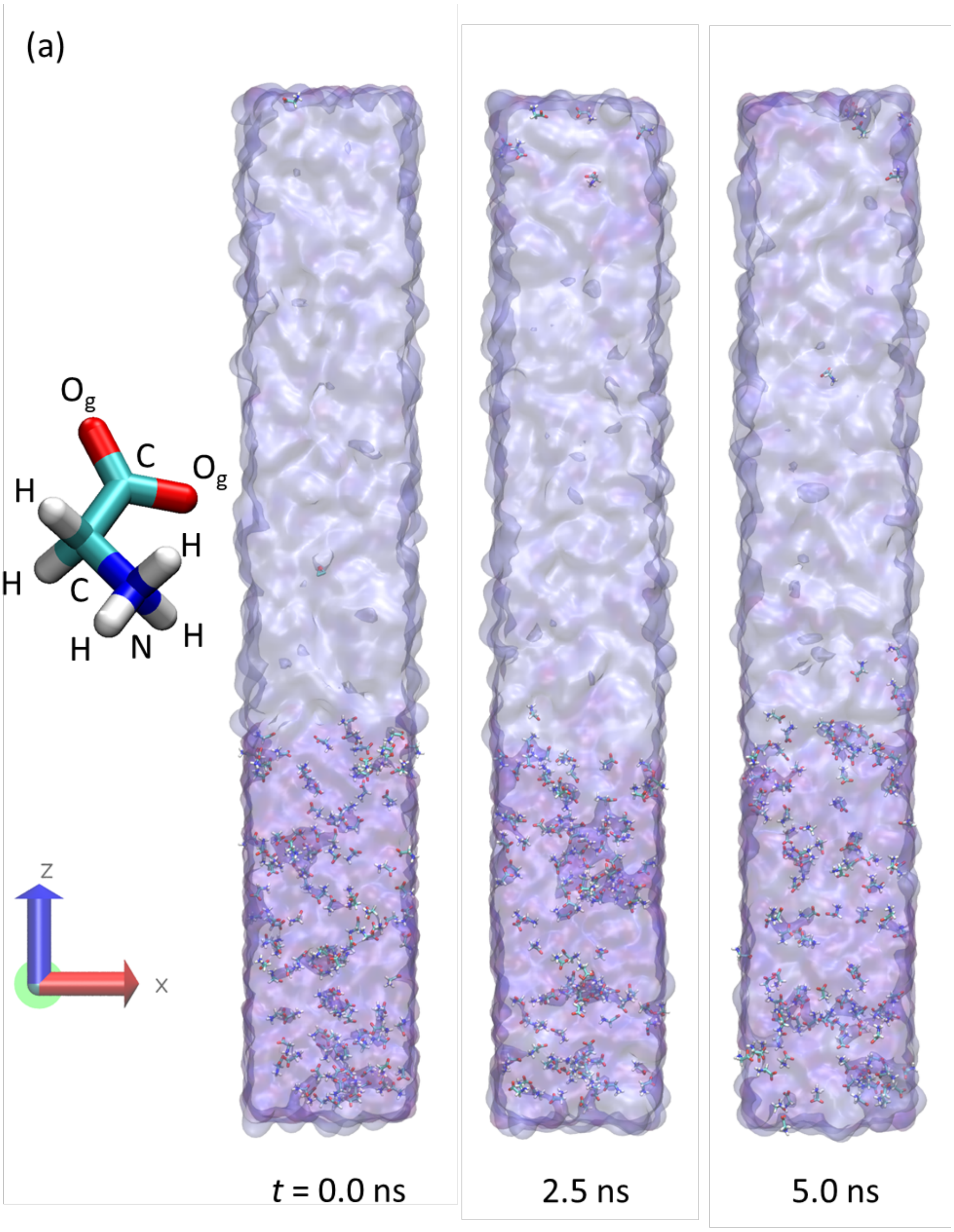
(a)
O$_g$
C
O$_g$
H
H
H
C
H
N
H
z
x
t = 0.0 ns
2.5 ns
5.0 ns

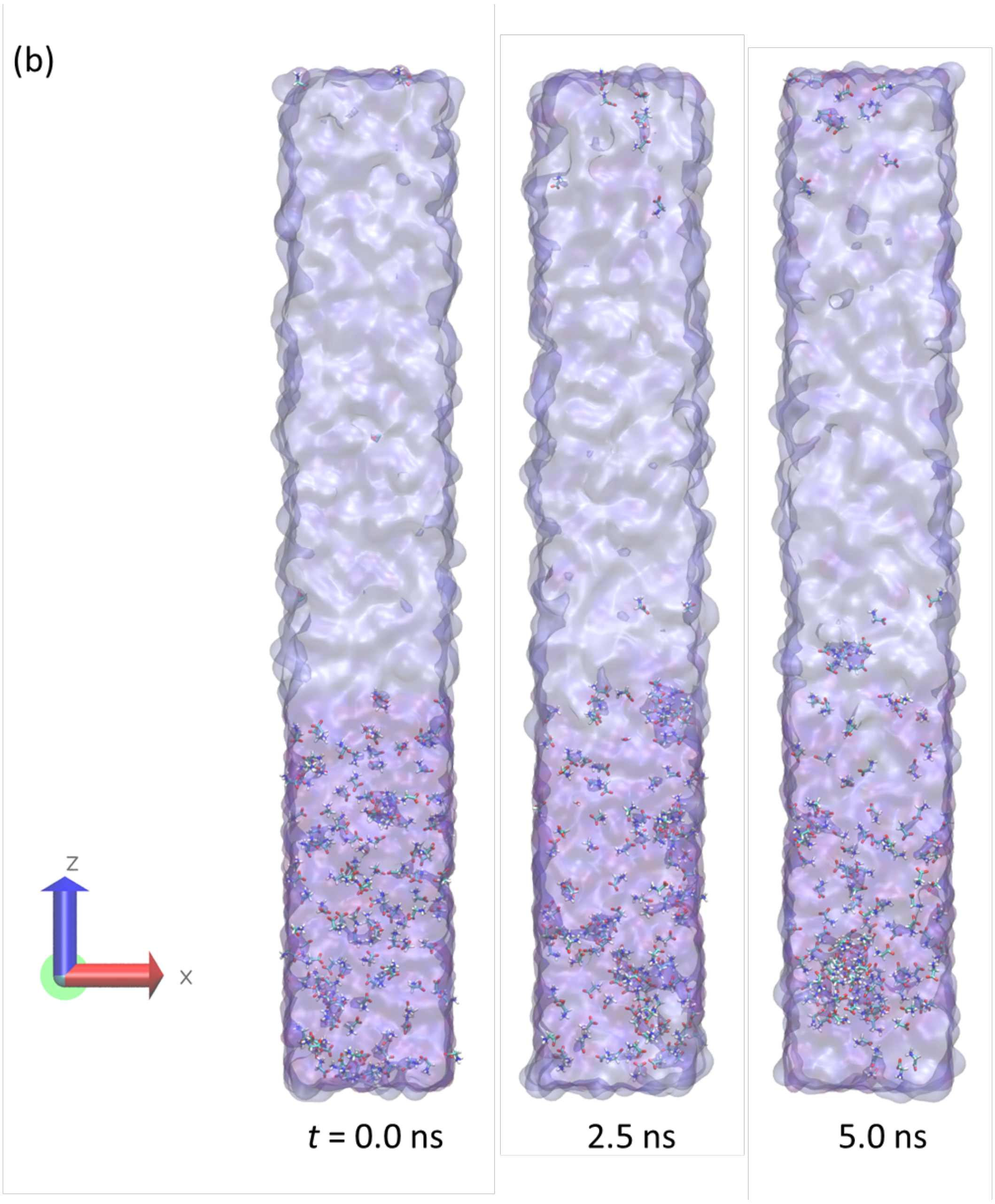
(b)
z
x
t = 0.0 ns
2.5 ns
5.0 ns

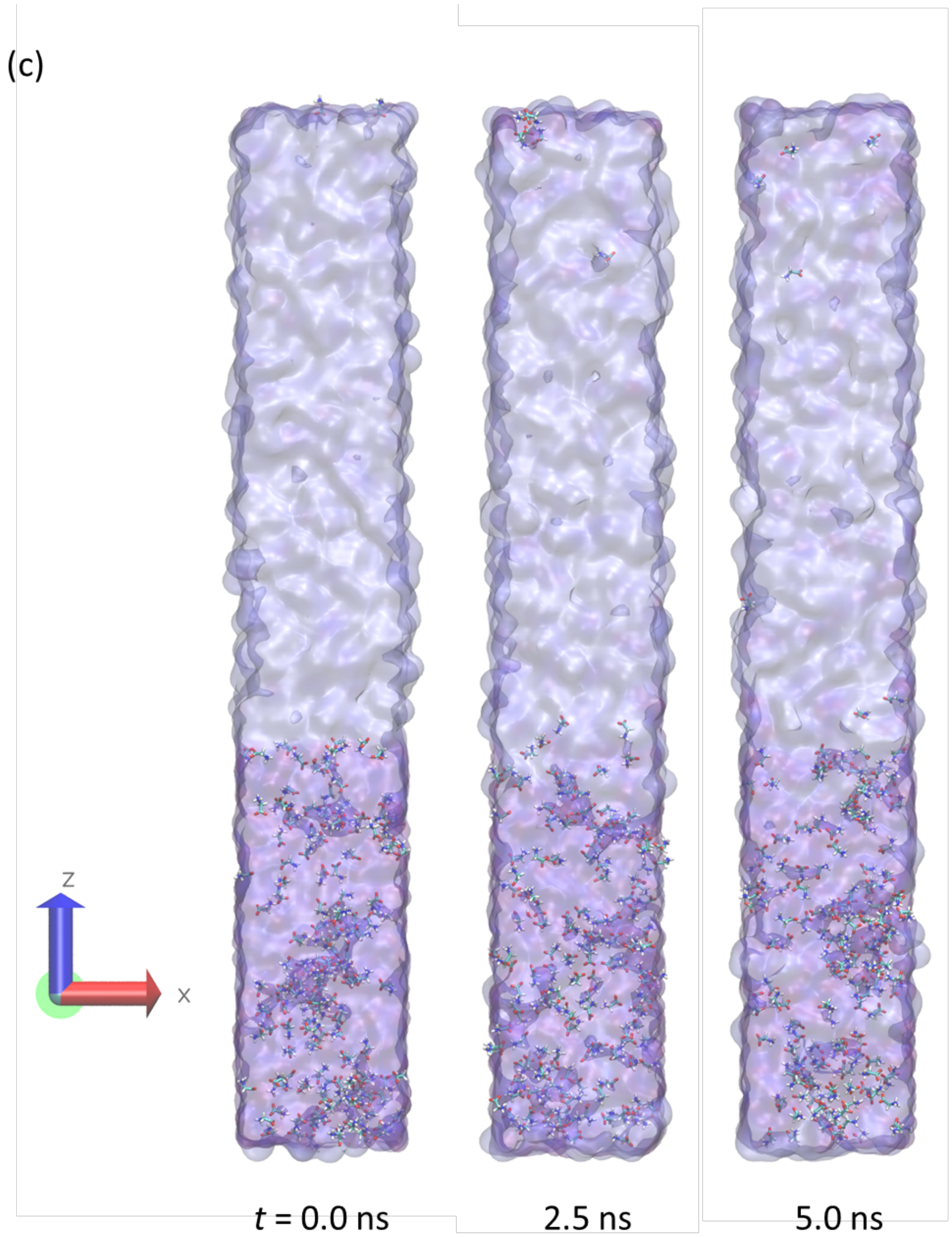

Fig. 4-6 Snapshots of the glycine aqueous solution and the ethanol system at t = 0.0, 2.5 and 5.0 ns at (a) C = 2.94, (b) C = 3.33, and (c) C = 3.72 mol kg^{-1}. Water and ethanol are not shown to avoid ambiguity. Color scale of atoms in packing: C (cyan), N (blue), O (red) and H (white).

4.3.3 Cluster size

The number of clusters increased with time, and the glycine concentration was based on the paired cluster of N–N of glycine, as described in the analytical method shown in Figure 4-7. In the case of C = 3.33 mol kg^{-1}, which had begun at the saturated situation, the cluster primarily comprised a dimer as the number basis. The increase in the solute concentration clearly affected the aggregation of glycine zwitterions. More paired clusters were initially observed in the supersaturated condition (C = 3.72 mol kg^{-1}). In contrast, in the undersaturated condition (C = 2.94 mol kg^{-1}), the cluster number fluctuated and did not significantly increase, even after t = 5.0 ns. In saturated and supersaturated condition, larger clusters have appeared and increased with time progression, as shown in Figure 4-8 which have semilog plots of the average number of a given cluster size. In three different concentration systems, when the logarithm of the number observed is linear with cluster size over a range of cluster sizes at t = 0.0-0.4 ns. However, in forming and breaking the cluster, the large cluster (approximately cluster size over 25) number increased and the probability is deviated from the logarithm line which based on single exponential free energy barrier to nucleation finally at t = 4.6-5.0 ns in saturated and supersaturated condition. Thus, this deviation shows one of the evidences not to follow CNT, especially that the large cluster shall follow TNT as shown in the snapshots of the glycine aqueous system in Fig. 4-6. However, dimers (n=2) and trimers (n=3) did not significantly increase with the time evolution and all concentrations of the glycine aqueous solution. This tendency agreed with the experimental results, revealing that the fractions of glycine molecules belonging to dimers and trimers weakly depended on the solute concentration.[42] This indicated that the larger cluster size needs higher supersaturation to maintain the cluster size.[43] The neighbouring area of the glycine cluster had been highly supersaturated owing to an increase in anti-solvent molecules through diffusion.

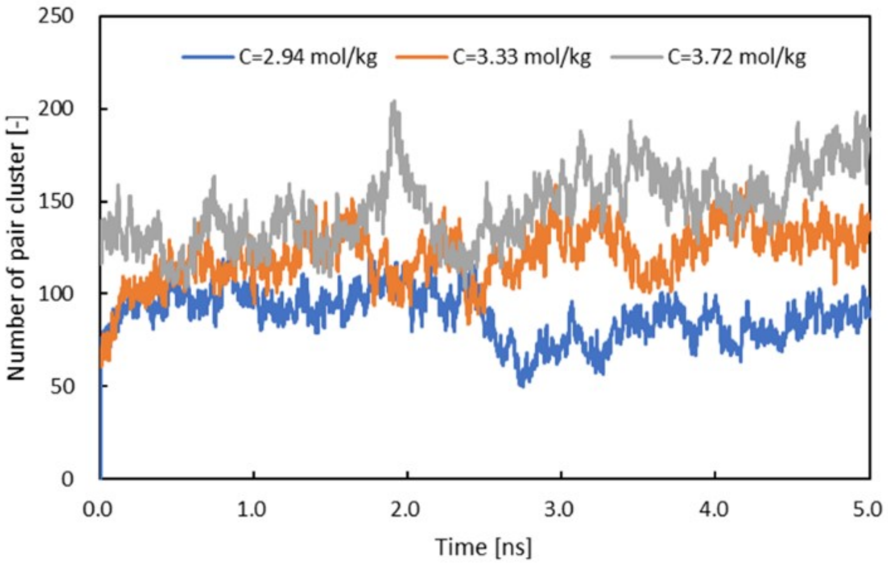

Fig. 4-7 Clustering behavior of the system: time progression of the number of paired clusters on C = 2.94, 3.33 and 3.72 mol kg^{-1} of the glycine solution.

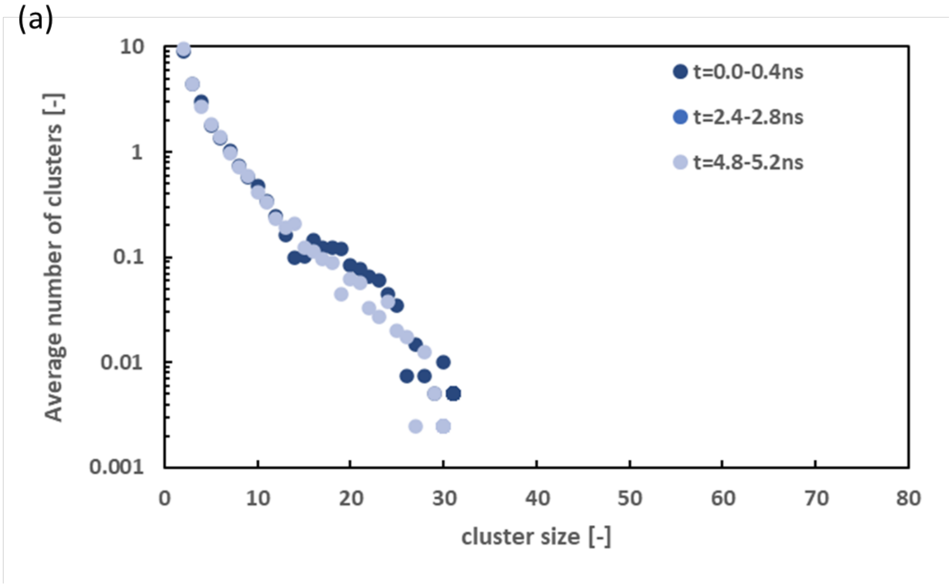

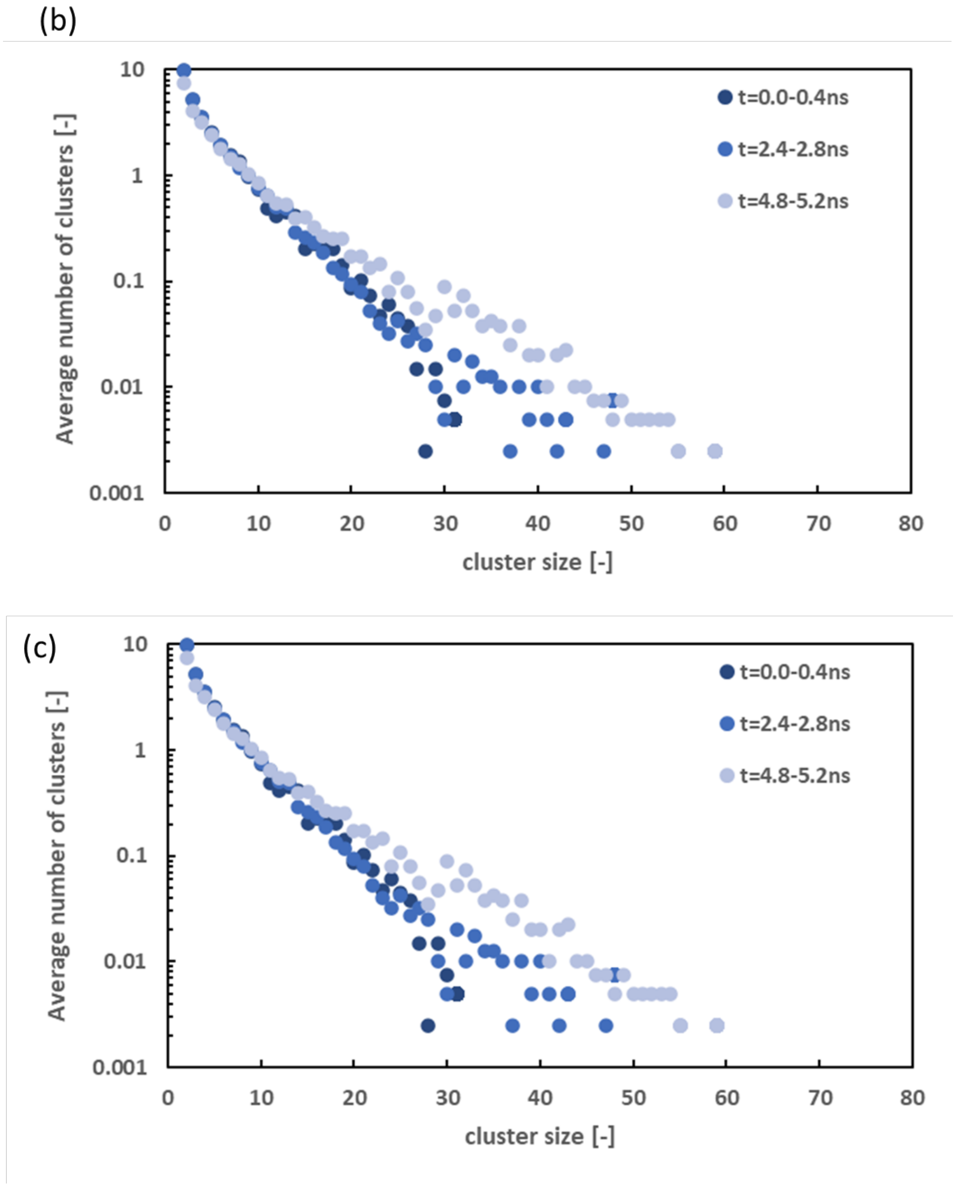

Fig. 4-8 Clustering behavior of the system: semilog histograms of the average number versus cluster size on (a) C = 2.94, (b) C = 3.33 and (c) C = 3.72 mol kg^{-1} .

4.3.4 Density profile along the Z axis (the normal to initial interface)

Average density profiles of each molecule were calculated at t = 4.9–5.0 ns with the same procedure in “Simulation validity” section. The mutual diffusion of water and ethanol molecules from each phase to the opposite phase was confirmed using their density profiles, as shown in Figure 4-9 (a). The density of ethanol maintains the bulk density in the whole range of the ethanol phase even after t = 5.0 ns. According to the progression of mutual diffusion, the densities were equivalated at their bulk values. The diffusion of molecules began through the initial interface at approximately Z = 0 and 8 nm and spread from each side. Majority of the glycine zwitterions were not moved to the ethanol phase because of less solubility which formed a high potential energy barrier. This movement, which dehydrated the glycine zwitterions, was suggested by the positive (glycine zwitterion) and negative (water) peaks on the similar Z axis location, and less glycine zwitterion moved to organic phase with water. The penetration amount of ethanol into the aqueous solution side increased with time and reached about 0.05–0.30 as a mole fraction at t = 5.0 ns, as shown in Fig. 4-9 (b). Bazi et al. reported a decrease in solubility with an increase in the ethanol mass percentage in the crystallization medium.[42] Drawing from the literature,[13,42] the solubility at the time of mole fraction = 0.05–0.30 was estimated to be approximately 67–167 g/100 g, and the supersaturation in the same region was considered to have reached as maximum 2–3-fold (S = 2–3) that of the saturated solution. Fig. 4-9 (a) shows that the glycine concentration in the Z-axis direction maintains a high state in near the center portion of the aqueous phase. Supported by these experimental results, cluster formations in the present simulation system conclude that the penetration of ethanol to the glycine aqueous solution decreased the solubility near glycine and caused supersaturation.

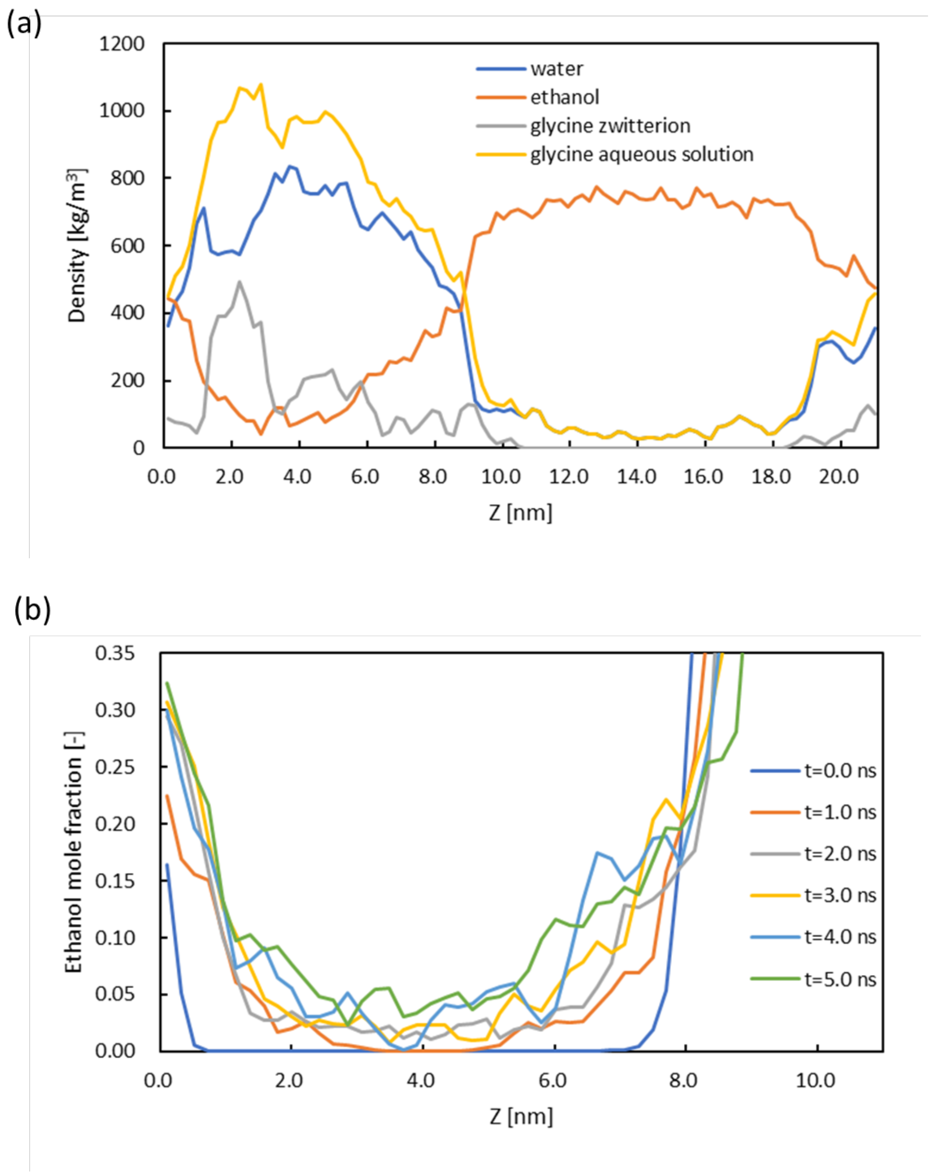

Fig. 4-9 Profiles along to Z axis (a) Density of each component at t = 5.0 ns of glycine aqueous solution at C = 3.33 mol kg^{-1} and ethanol (b) Mole fraction of ethanol at t = 0.0 – 5.0 ns by every 1.0 ns.

4.3.5 Dehydration behavior of glycine zwitterion

To investigate the effect of the anti-solvent on ethanol from the solute side, coordination numbers of N-O$_w$ of the glycine zwitterions are shown in Figure 4-10 at C = (a) 2.94, (b) 3.33 and (c) 3.72 mol kg^{-1} of glycine aqueous solution. Dehydration from the glycine molecule fluctuated depending on time. However, the average value of the hydration number (coordination number of water to zwitterion) clearly decreased and spread to a wider range of Z axis with the time evolution, which is illustrated as a green area expansion in the aqueous phase. From the time point t = 1.0 to 5.0 ns, the continuous dehydration provided by mutual diffusion between water and ethanol is described in Fig. 4-10. The tendency between the cluster position and the dehydrated area was located at a similar point, suggesting that dehydration leads to the clustering of zwitterions. However, according to the Bushuev et al.,[22] the clusters of glycine zwitterion, which were strongly hydrated entities, exhibited a liquid-like character. The following section highlights the behavior of the clusters based on an evaluation of their structure.

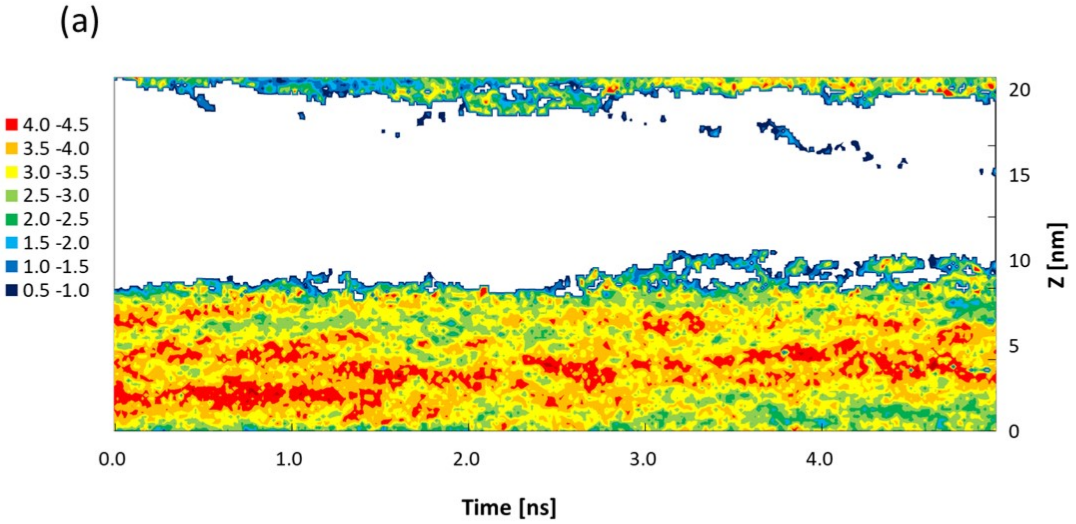

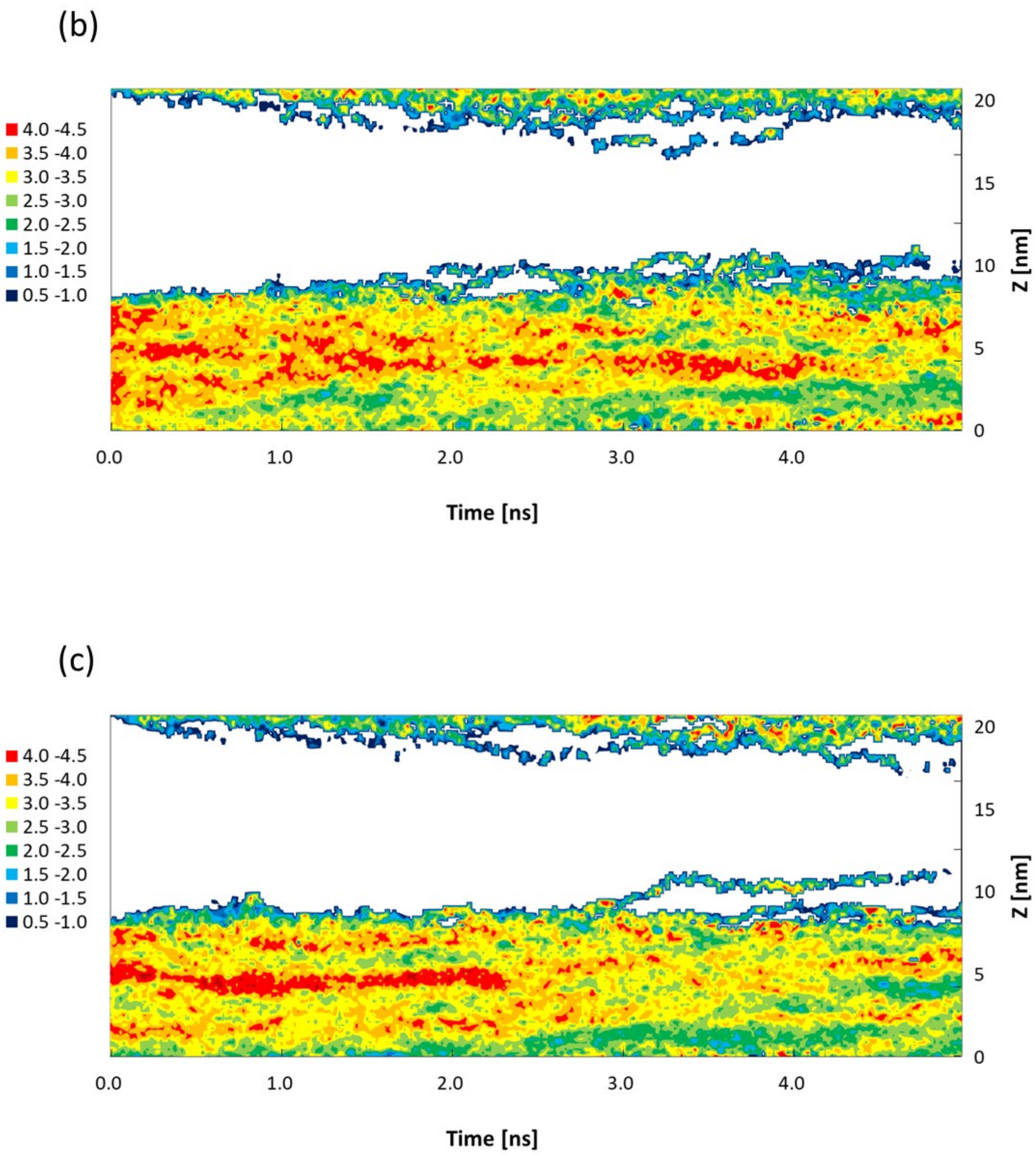

Figure 4-10 Coordination number of N–O_W vs. time (t = 0.0–5.0 ns) at (a) C = 2.94 mol kg^{-1}, (b) C = 3.33 mol kg^{-1}, and (c) C = 3.72 mol kg^{-1} of glycine aqueous solution. The color legends are shown in left side of figure.

4.3.6 Structure of glycine zwitterion cluster

Two types of hydrogen bonds can be formed between zwitterionic glycine in an aqueous solution: NH···O_g and CH···O_g bonds. These bonds play a major role in determining the glycine crystal structure. However, the CH···O_g interaction was much weaker compared with the NH···O_g interaction, as described in Yani et al.,'s work.[34] As shown in Table 4-3 and Figure 4-11, hydrogen bonding parameters and hydrogen bonds among polymorphs are different between the α, β and γ polymorphs.[43] The parallel arrangement of the C–C vectors is also a distinctive feature of the γ-polymorph.

Figure 4-12 shows the increase of number of hydrogen bonds per molecules to cluster size = 5 and the number was saturated at about 0.2 over the size = 5. This result indicates that the hydrogen bond network among glycine clustering molecules tends to propagate in a form of 5 glycine molecules as a structured one unit.

The hydrogen bonds NH···O_g between glycine–glycine zwitterion were analyzed by observing their hydrogen bond angles with similar density distributions of glycine zwitterion, as shown in Figure 4-13 (a) according to the Z axis with two different criteria of angle (140 degree < angle < 160 and 160 degree < angle). Despite the angle of the hydrogen bond, the profiles were similar compared with the glycine density.

The profiles of the hydrogen bond and density profile of each molecule and the cluster formation mechanism in this system can be explained as follows. First, ethanol flowed into the aqueous phase. Then, the solubility of ethanol immediately decreased, dehydrating the glycine molecules to obtain more bond energy to be stable in the supersaturation state.

Two possible types of dimerization by hydrogen bonds can be formed between zwitterionic glycine molecules: cyclic and open dimers. The cyclic dimer is often discussed as one of the single units of the α polymorph.[37] In contrast, an open dimer is assumed to be the unit of all polymorphs, particularly γ polymorphs owing to their structure and stable thermodynamic state.

The C–C vector of the glycine–glycine zwitterion cluster was analysed for the polymorphic change in the clusters. As shown in Fig. 4-13 (b), regardless of the number of hydrogen bonds in Fig. 4-13 (a), clusters have a higher value of the C–C vector angle with higher ethanol mole fraction, indicating an ordered structure of the cluster. Higher value indicates opposite direction of each C–C vector of the molecules which consists cluster and suggests the structure is cyclic mode. This provides a conclusion that cluster shifts to more structured mode by certain amount of anti-solvent (over 0.1 mole fraction) and oppositely cluster maintains liquid like structure in less amount of anti-solvent even the area significantly dehydrated and densified with glycine. As discussed about the initial stages of $CaCO_3$ nucleation by Henzler et al., solvent mediation is also key phenomena to define the polymorph from amorphous precursor.[44] In experiments, during anti-solvent crystallization of glycine, the transformation between the β and α forms or the γ form occurs via a solution-mediated transformation rather than an α solid-state transformation. The solution-mediated transformation simultaneously occurs via dissolution of the β form glycine crystals with the nucleation and growth of the α or γ form crystals. Therefore, this shift of cluster to structured mode by anti-solvent needs to be further discussed how the impact of the change leads to the nucleation and precipitated polymorph.

Considering the anti-solvent system in the present work, the probability change of dimer mode (cyclic/open), caused by confirmation restriction (energy barrier) by organic solvent and a high concentration environment, suggests a change of cluster structure which related to potential polymorphism as precursor. Most of cluster size did not reach the critical nucleation size due to limited simulation time and simulation box size. However, the over critical nucleation size clusters which deviated from exponential relation of free energy barrier exist as a state of LLPS due to high supersaturation, suggesting that a change has already occurred at the cluster stage, which produced a structural difference and is not CNT.

Table 4-3 List of hydrogen bond (N-H…O_g) of glycine alpha and gamma polymorph

polymorph	Distance H…O_g [A]	Distance N…O_g [A]	Angle of N-H…O_g [degree]
α	2.413	2.953	115.74
	2.186	3.080	156.29
	1.794	2.778	167.51
	1.888	2.854	168.7
γ	1.941	2.807	159.89
	1.934	2.802	163.29
	2.121	2.983	173.5

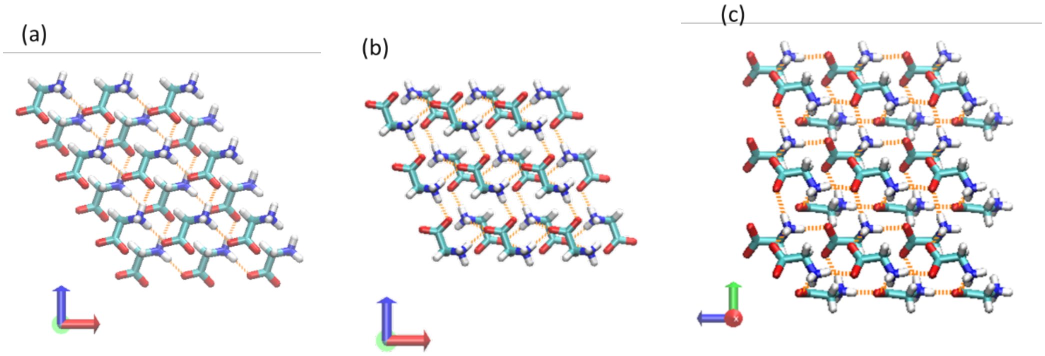

Fig. 4-11 Hydrogen bonding between the glycine crystal of each (a) α, (b) β and (c) γ polymorph. The hydrogen bonds which angles are over 140 degree between glycine molecules are depicted in orange.

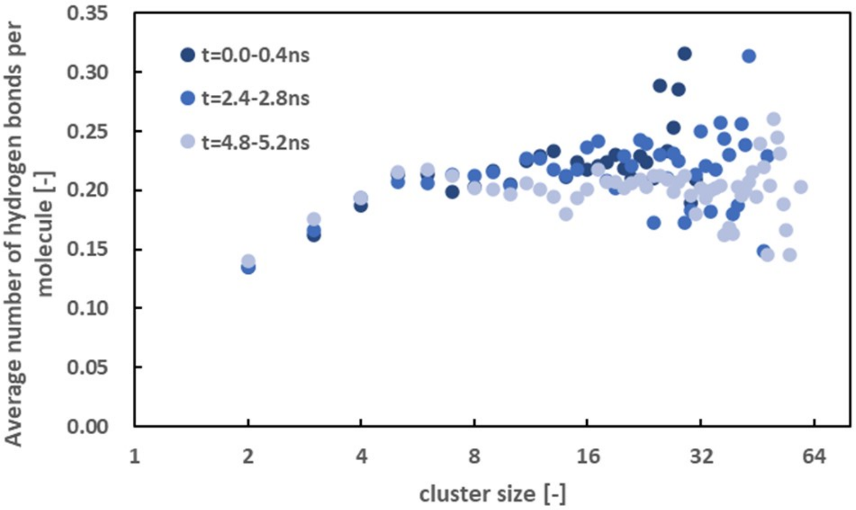

Fig. 4-12 Average number of hydrogen bonds per molecule vs. cluster size at C = 3.33 mol kg^{-1} of glycine aqueous solution.

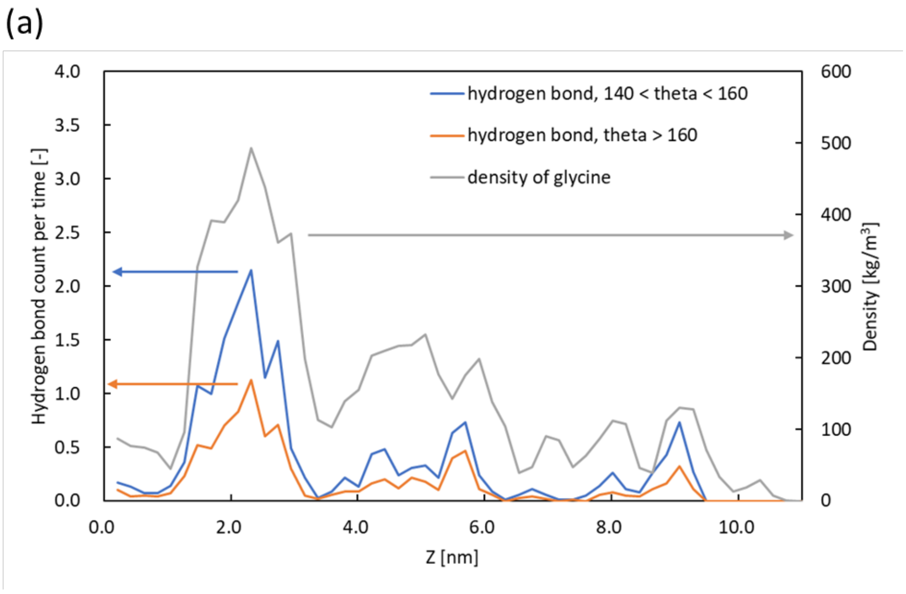

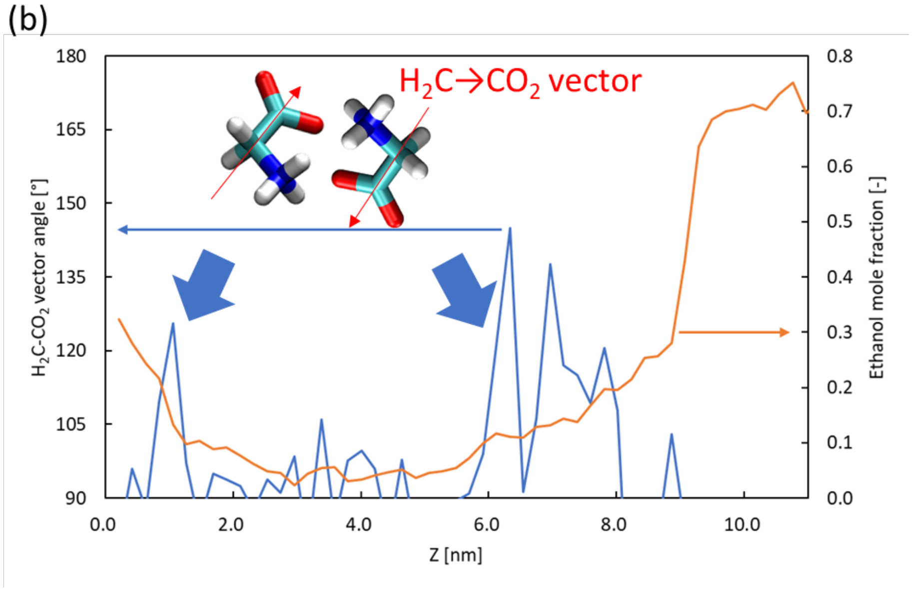

Fig. 4-13 (a) Hydrogen bond and density position profiles of glycine according to the Z axis at t = 5.0 ns., (b) $H_2C \rightarrow CO_2$ vector angle of glycine cluster and ethanol mole fraction according to the Z axis at t = 5.0 ns.

4.4 Conclusion

We investigated glycine zwitterion clustering behavior, with respect to time progression and structural change in the clusters through classical MD simulation to understand nucleation phenomena in LLPS. By observing the behavior of precursors, called clusters, which occur at a stage prior to nucleation, we clarified the clustering of glycine zwitterions as LLPS as a model case of the two-step nucleation theory. The MD simulations focused on the changes in cluster size, number and hydrogen bonding based on the increase in supersaturation due to the invasion of the anti-solvent. The simulation with the reported potential and charge sets showed consistency with the physical properties and provided the data as the instant of contact for the glycine aqueous solution and ethanol.

According to the progression of dehydration, glycine zwitterions primarily formed clusters in the aqueous phase as the poor solvent flowed in, and their size increased. The logarithm of average number of clusters was observed with over a range of cluster size and the number of hydrogen bonds were saturated with regardless the cluster size. In parallel with the increase in size, a structural change from liquid like to a cyclic dimer occurred in the high supersaturated region where the proportion of the poor solvent was high. The increase of the C–C vector angle of glycine in such a highly supersaturated region supported the structural changes. This evidences the structural change of cluster in the LLPS and potential impact to polymorphism determination at the cluster stage.

A more generic understanding of nucleation can be gained as the system in the present work has used the simplest amino acid and ethanol for a typical organic molecule. The structural change which depends on anti-solvent ratio might related to the origin of one of intrinsic complexities of anti-solvent crystallization and suggests importance of micro level uniformity of good and anti-solvents. In the future, considering the free energy barriers[45] based on CNT and TNT and fluctuations by solvent-mediated can shed light on the organization of LLPS and cluster formation from a quantitative thermodynamic perspective.

*This chapter was reproduced and modified from [*CrystEngComm*, 2020, **22**, 5182-5190], with permission from Royal Society of Chemistry.

References

[1] D. Erdemir, Alfred Y. Lee, and A. S. Myerson, *Accounts Chem. Res.*, 2009, **42**, 5, 621-629

[2] D. Kashchiev, *J. Cryst. Growth*, 2020, **530**, 125300, 1-13

[3] S. Karthika, T. K. Radhakrishnan and P. Kalaichelvi, *Cryst. Growth Des.*, 2016, **16**, 6663−6681

[4] S. Supriya, S. Sushmitha, and K. Srinivasan, *Cryst. Growth Des.*, 2019, **19**, 6315−6323

[5] G. A. Ilevbare and L. S. Taylor, *Cryst. Growth Des.*, 2013, **13**, 1497−1509

[6] A. C. Dumetz, A. M. Chockla, E. W. Kaler and A. M. Lenhoff, *Biophys. J.*, 2008, **94**, 570–583

[7] J. F. Lutsko, *Science Advances*, 2019, **5**, 4, eaav7399

[8] K. Maeda, T Miki, K. Itoh, K. Arafune, T. Yamamoto, and K. Fukui, *J. Mol. Liq.*, 2015, **209**, 1–5

[9] W. Tang, H. Mo, M. Zhang, J. Gong, J. Wang, and T. Li, *Cryst. Growth Des.*, 2017, **17**, 5028−5033

[10] G. Albrecht, R. B. Corey, *J. Am. Chem. Soc.*, 1939, **61**, 1087-1103

[11] K. Park, J. M. B. Evans, and A. S. Myerson, *Cryst. Growth Des.*, 2003, **3**, 991-995

[12] C. Parks, A. Koswara, F. DeVilbiss, H. H. Tung, N. K. Nere, S. Bordawekar, Z. K. Nagya and D. Ramkrishna, *Phys. Chem. Chem. Phys.*, 2017, **19**, 5285--5295

[13] A. Bouchard, G. W. Hofland and G. J. Witkamp, *J. Chem. Eng. Data*, 2007, **52**, 1626-1629

[14] Y. C. Chang, A. S. Myerson, *AIChE J.*, 1986, **32**, 1567-1569

[15] Y. C. Chang, A. S. Myerson, *AIChE J.*, 1987, **33**, 697-699

[16] C. E. Hughes, S. Hamad, K. D. M. Harris, C. R. A. Catlow and P. C. Griffiths, *Faraday Discuss.*, 2007, **136**, 71–89

[17] Z. Cao, Y. Hu, J. Li, Y. Kai and W. Yang, *Fluid Phase Equilibria*, 2013, **360**, 156–160

[18] V. I. Smirnov and V. G. Badelin, *Russian Journal of Physical Chemistry*, 2003, **77**, 5, 713-71

[19] I. Weissbuch, V. Yu. Torbeev, L. Leiserowitz and M. Lahav, *Angew. Chem. Int. Ed.*, 2005, **44**, 3226–3229

[20] M. Matsumoto, Y. Wada, S. Maesawa, T. Hiaki, K. Onoe, *Adv. Powder Technol.*, 2019, **30**, 707–713

[21] H. J. C. Berendsen, J. R. Grigera, and T. P. Straatsma, *J. Phys. Chem.*, 1987, **91**, 6269-6271

[22] Y. G. Bushuev, S. V. Davletbaeva and O. I. Koifman, *CrystEngComm*, 2017, **19**, 7197-7206

[23] D. W. Cheong and Y. D. Boon, *Cryst. Growth Des.*, 2010, **10**, 5146-5158

[24] K. A. Maerzke, N. E. Schultz, R. B. Ross and J. I. Siepmann, *J. Phys. Chem. B*, 2009, **113**, 6415-6425

[25] M. P. Allen and D. J. Tildesley, *Computer Simulation of Liquids*, 1987, Oxford University Press

[26] L. V. Woodcock, *Chem. Phys. Lett.*, 1971, **10**, 3, 257-261

[27] K. Kadota, T. Wake, K. Gonda, A. Kitayama, Y. Tozuka, A. Shimosaka, Y. Shirakawa, and J. Hidaka, *J. Mol. Liq.*, 2014, **197**, 243-250

[28] J. B. Dalton and C. L. A. Schmidt, J. Biol. Chem., 1933, 103, 549−578

[29] J. A. Dean, *LANGE'S HANDBOOK OF CHEMISTRY 10th Ed*, McGraw-Hill, New York, 1961

[30] L. Verlet, *Phys. Rev.*, 1967, **159**, 98-103

[31] J. P. Ryckaert, G. Ciccotti, H. J. C. Berendsen, *J. Computer Phys.*, 1977, **23**, 3, 327-341

[32] H. C. Andersen, *J. Compt. Phys.*, 1983, **52**, 1, 24-34

[33] W. Humphrey, A. Dalke and K. Schulten, J. *Molec. Graphics,* 1996, **14**, 1, 33-38

[34] Y. Yani, P. S. Chow, and R. B. H. Tan, *Cryst. Growth Des.*, 2012, **12**, 4771−4778

[35] M. J. Servis, D. T. Wu, J. C. Braley, *Phys.Chem.Chem.Phys.*, 2017, **19**, 11326-11339

[36] A. I. Jion and R. Rajagopalan, *CrystEngComm*, 2014, **16**, 6224

[37] S. Hamad, C. E. Hughes, C. R. A. Catlow and K. D. M. Harris, *J. Phys. Chem. B*, 2008, **112**, 7280–7288

[38] J. Huang, T. C. Stringfellow and L. Yu, *J. Am. Chem. Soc.*, 2008, **130**, 13973–13980

[39] D. M. Rodríguez and C. M. Romero, *J. Chem. Eng. Data*, 2017, **62**, 3687-3696

[40] Y. Kameda, H. Ebata, T. Usuki, O. Uemura, and M. Misawa, *Bull. Chem. Soc. Jpn.* 1994, **67**, 3159

[41] Y. Kamano, K. Kadota, A. Shimosaka, Y. Shirakawa, J. Hidaka, *J. Mol. Liq.*, 2014, **200**, 474–479

[42] W. E. Bazi, C. Porte, I. Mabille, J. L. Havet, *J. Crystal Growth*, 2017, **475**, 232–238

[43] K. Renuka Devi and K. Srinivasan, *CrystEngComm*, 2014, **16**, 707–722

[44] K. Henzler, E. O. Fetisov, M. Galib, M. D. Baer, B. A. Legg, C. Borca, J. M. Xto, S.

Pin, J. L. Fulton, G. K. Schenter, N. Govind, J. I. Siepmann, C. J. Mundy, T. Huthwelker, J. J. De Yoreo, *Sci. Adv.* 2018, **4**, eaao6283, 1-11

[45] R. Innocenti Malini, C. L. Freeman, J. H. Harding, CrystEngComm, 2019, **21**, 6354–6364

Chapter 5

Diffusion mechanism and release profile of a multivitamin from TiO_2 hollow particles

5.1 Introduction

In our research group, the particle morphology by limiting the particle generation field to the micro droplet interface has been controlled as application of liquid–liquid interfacial phenomena.[1] Specifically, a spherical interface is formed by using an inkjet nozzle that is able to discharge minute and uniform droplets, and a particle is precipitated along the droplet's interface. As one of the applied pharmaceutical derivatives, uniform spherical hollow particles of titanium oxide (TiO_2) is obtained by applying the sol-gel method to this particle preparation.[2,3] This particles has a potential to show sustained release by encapsulating drug substance to their hollow space as a part of component of transdermal drug delivery system.[4]

In this Chapter 5, to elucidate the release mechanism of drug substances from hollow particles as one of the liquid–solid interfacial phenomena, vitamin C (VC) and vitamin E (VE) were selected as drug substances which are known to have good and poor water solubility.[5,6] The encapsulation process, characterization of obtained particles and sustained release behavior and related diffusion mechanism of the encapsulated drug substances were investigated compared with the results of each single and multi-components.

5.2 Materials and methods

5.2.1. Materials

Titanium tetraisopropoxide (TTIP) (95%), hexane (97%), hydrochloric acid (HCl), acetonitrile (99%), DL-a-tocopherol acetate (VE derivative), 0.1 mol/L-potassium hydroxide solution (KOH) and 0.1 mol/L-nitric acid (HNO_3) were purchased from Nacalai Tesque, Inc. (Kyoto, Japan). L(+)-ascorbic acid 2-sulfate disodium salt dihydrate (VC derivative) was purchased from FUJIFILM Wako Pure

Chemical Corporation (Kyoto, Japan). TTIP was selected as the starting precursor for the TiO_2 particles for the sol-gel process. Hexane was also selected as an organic solvent to form the immiscible liquid–liquid interface with water. Acetonitrile was used to control the reaction rate using the miscibility to water. Both hexane and acetonitrile were sufficiently dehydrated by molecular sieves before the particle synthesis.

5.2.2. Preparation of TiO_2 particles via sol-gel process with the inkjet nozzle

The TiO_2 particles were prepared using a previously made interfacial sol-gel processing preparation.[1] Six milliliters of TTIP was added to 64 mL of hexane and dissolved by agitating for 10 min. The concentration of water was adjusted to 9.09 vol% by adding acetonitrile, and the pH of the solution was adjusted to 4.0 by adding HCl. Sol-gel processing was used to prepare the TiO_2 particles using the inkjet nozzle (IJHB-1000; Microjet Co., Ltd.) and inkjet driver (IJHC-10; Microjet Co., Ltd.). The diameter of the inkjet nozzle was 80 μm. The droplets from the inkjet nozzle was observed using a light microscope (Moticam 1000; Shimadzu Rika Co., Ltd.) at 0.2 ms intervals via a blue diode. The aqueous solution was dropped using the inkjet nozzle into the TTIP solution at 500 drops/s for 30 min. After preparation, the suspension was filtered using a membrane filter with a 0.1 μm pore size. The TiO_2 particles were washed with ethanol and dried in a desiccator at 25 ± 5 °C for 1 day.

5.2.3. Preparation of TiO_2 particles encapsulating vitamin C and E

An immersion method was used to encapsulate both vitamin C and E inside the TiO_2 hollow particles.[4] The solutions of 80 mL were mixed in an ethanol–water solution (1:1, v/v). The VC derivative (0.08 g) was added to the ethanol–water solution and this solution was placed for 10 min in a reduced pressure environment that was maintained with a vacuum pump. TiO_2 particles (0.1 g) were added to the VC derivative solution. The solution was placed for 10 min in the reduced pressure environment again to allow the VC derivative solution to permeate the TiO_2 hollow particles. The solution permeated into the hollow space of the particles through the process, and the particles sunk. The mixtures of paticles and solution were allowed to rest for 30 min; then, the supernatant solution was removed. The obtained particles are referred to as the VC sample. The same immersion procedure was performed using the VE derivative and both VC and VE derivatives. The obtained particles are referred to as the VE sample and the VC + VE sample, respectively.

5.2.4 Characterization of TiO_2 particles

The surface morphologies of the TiO_2 particles were observed by scanning electron microscopy (SEM; VE7800; Keyence Co., Ltd.). The TiO_2 particles were sputter-coated with gold before observation with the sputtering equipment (E-1045; Hitachi High-Technologies Corporation, Tokyo, Japan). The inner structure of the TiO_2 particles was examined by cutting particles with an ion milling apparatus (E-3500; Hitachi High-Technologies Corporation) and observing the cross sections by SEM. Obtained TiO_2 hollow particles were embedded into an epoxy resin (C, H, O). The resin with the particles was cut by treatment with ion milling for making cross-section samples. The encapsulation of the VC derivative in the TiO_2 hollow particles (VC sample) was analyzed by elemental sodium and sulfur mapping using an energy dispersive X-ray spectrometer (EDS; EMAX ENERGY EX-420; Horiba Corporation, Japan) that was connected to a field emission-type scanning electron microscope (SU8020; Hitachi High-Technologies Corporation). The acceleration voltage was adjusted to 5 kV and the cutting of the TiO_2 particles was performed for 6 h. All samples were covered with resin to remove the air bubbles via a degassing treatment. The TiO_2 particles were sputter-coated with gold before observation using the sputtering equipment as described above. The encapsulation of the VE derivative inside the TiO_2 hollow particles (VE sample) was analyzed by elemental carbon mapping in the same manner. The pore characteristics of the TiO_2 particles were investigated using Barrett-Joyner-Halenda (BJH) method with nitrogen adsorption analyzer (Micromeritics, Tristar3000).

5.2.5 Release test

The release behavior of the VC derivative from the TiO_2 particles was evaluated by the dialysis bag method using distilled water as the release media.[7–14] The VC sample or the VC + VE sample (50 mg) were added to the dialysis bag with 5.0 mL of distilled water. The dialysis bag was placed in 200 mL of distilled water at 37 ± 0.5 °C and stirred at 100 rpm. Then, 5 mL of release media was removed, and 5 mL of fresh distilled water was added at sampling time. The release test was performed for 12 h. The VC derivative concentration was determined by a UV–vis spectrophotometer (JASCO, V-570) from the peak area between 240 and 265 nm.[15] The release behaviors of the VE derivative from the VE sample or the VC + VE sample were evaluated in the same manner. At this time, ethanol was used as the release medium. The VE derivative concentration was determined by UV–vis spectrophotometer from the peak area between 265 and 290 nm.[16]

5.2.6 Potentiometric titration method

After the drug substances were encapsulated by the immersion method, the surface charge of the TiO_2 particles was obtained by the potentiometric titration method.[17,18] Each step of this method are described as following procedure. First, 0.02 M KOH aqueous solution was prepared, and the pure sample (only the TiO_2 hollow particles; 0.0625 g) was added. Then, 0.2 mL of 0.1 M HNO_3 aqueous solution was added dropwise to achieve the obtained suspension over the course of 1 h. The volume of the added HNO_3 aqueous solution and pH values of the solution were recorded. The titration was terminated when 20 mL of HNO_3 aqueous solution was added. Blank titration was performed in the same manner with the same solution but without the pure sample (only the TiO_2 hollow particles). This procedure was performed at room temperature. The surface charge σ was calculated from Eq. 5-1.

$$\sigma = \mathrm{M} \cdot \mathrm{F} \cdot \Delta\mathrm{V}/\mathrm{m} \cdot \mathrm{S} \qquad (5\text{-}1)$$

where ΔV [l] is the difference between the titrant volumes of the suspension and the blank at a given pH value, M [mol/l] is the concentration of the titrant solution, F is the Faraday constant (96,500 C/mol), m [g] is the particle mass, and S [m^2/g] is the specific surface area of the particles.

5.2.7 Calculation of the diffusion coefficient

The effective diffusion coefficient was determined to estimate the diffusion mechanism of the drug substances from the TiO_2 hollow particles. The diffusion rate per unit area, N_A [lg/(cm^2・s)], of a porous solid can be expressed by Eq. 5-2, [19–21]

$$N_A = -\mathrm{D}_e \frac{dC_A}{dx} \qquad (5\text{-}2)$$

where D_e [cm^2/s] is the effective diffusion coefficient, C_A [μg/ml] is the concentration of component A, and x [cm] is the distance. Furthermore, for pore diffusion, a relational expression (Eq. 5-3) is established between D_e, and the general diffusion coefficient, D_0.

D_0 can be expressed by Eq. 5-4.

$$D_e = (\varepsilon/q)D_0 \tag{5-3}$$

$$\frac{1}{D_0} = \frac{1}{D_{AB}} + \frac{1}{D_{KA}} \tag{5-4}$$

$$D_{KA} = \frac{2}{3}\sqrt{\frac{8RT}{\pi M_A}} \cdot a \tag{5-5}$$

where ε is the porosity, q is the tortuosity, D_{AB} [cm^2/s] is the molecular diffusion coefficient, D_{KA} [cm^2/s] is the Knudsen diffusion coefficient, M_A is molecular weight of component A, and a is pore radius. As a note, the above calculations are assumed for a parallel pore model with relatively uniform are arranged in parallel with arbitrary tortuosity (tortuosity = 2) based on pore diameter compared to more porous TiO_2.[22] The diffusion coefficients of the VC, VE, VC + VE samples were obtained using these equations, and the experimental values were obtained by the release test. By comparing these values, a diffusion mechanism from the TiO_2 hollow particles was estimated.

5.3 Results and discussion

5.3.1 Formation mechanism of TiO_2 particles during inkjet process

The formation mechanism of TiO_2 hollow particles by inkjet nozzle briefly described because the formation mechanism of TiO_2 particles in inkjet process was demonstrated.[1] The hydrolysis of TTIP and the diffusion of acetonitrile into hexane co-occurred at the interface between hexane-TTIP solution and acetonitrile-water solution as previously illustrated.[1] The liquid droplet from inkjet nozzle constricted under the effect of diffusion of acetonitrile into hexane. The size of droplet would be reduced due to the hydrolysis and polycondensation at liquid–liquid interface, where the boundary of liquid–liquid interface constricts. Therefore, the nucleation and crystal growth of TiO_2 particles occurred within the confined space of the droplets of HCl solution.[23] This formation mechanism would lead to promotion of the agglomeration of TiO_2 crystals within the droplets. Consequently, the particle size of TiO_2 become larger. In general, the high hydrolysis rate of titanium alkoxide causes uncontrolled precipitation.[24] However, the hydrolysis rate of titanium alkoxide could be controlled adequately with hexane–water/acetonitrile interface by inkjet nozzle because the obtained particles showed mono dispersed particle size distribution.

5.3.2 Effect of encapsulating VC and VE derivatives on particle morphology

SEM images of the pure (only TiO_2 hollow particles), VC, VE, and VC + VE samples are shown in Fig. 5-1(a), (b), (c), and (d), respectively. Both the pure (TiO_2 hollow particles) and the VC samples were uniform spherical particles. Upon encapsulation of the hydrophilic VC derivative, there was little influence on the particle morphology. Similar results were obtained by comparing the pure (TiO_2 hollow particles) and VE samples, and there was little influence on the particle morphology by encapsulation of the hydrophobic VE derivative. Furthermore, upon encapsulating, the VC and VE samples also showed uniform spherical morphologies. Encapsulation of the VC and VE derivatives did not affect their particle morphologies via the present preparation. Moreover, no samples were found to be hollow structures. These results suggest that the prepared structure can hold substances within the TiO_2 hollow particles regardless of their hydrophilic and hydrophobic properties.

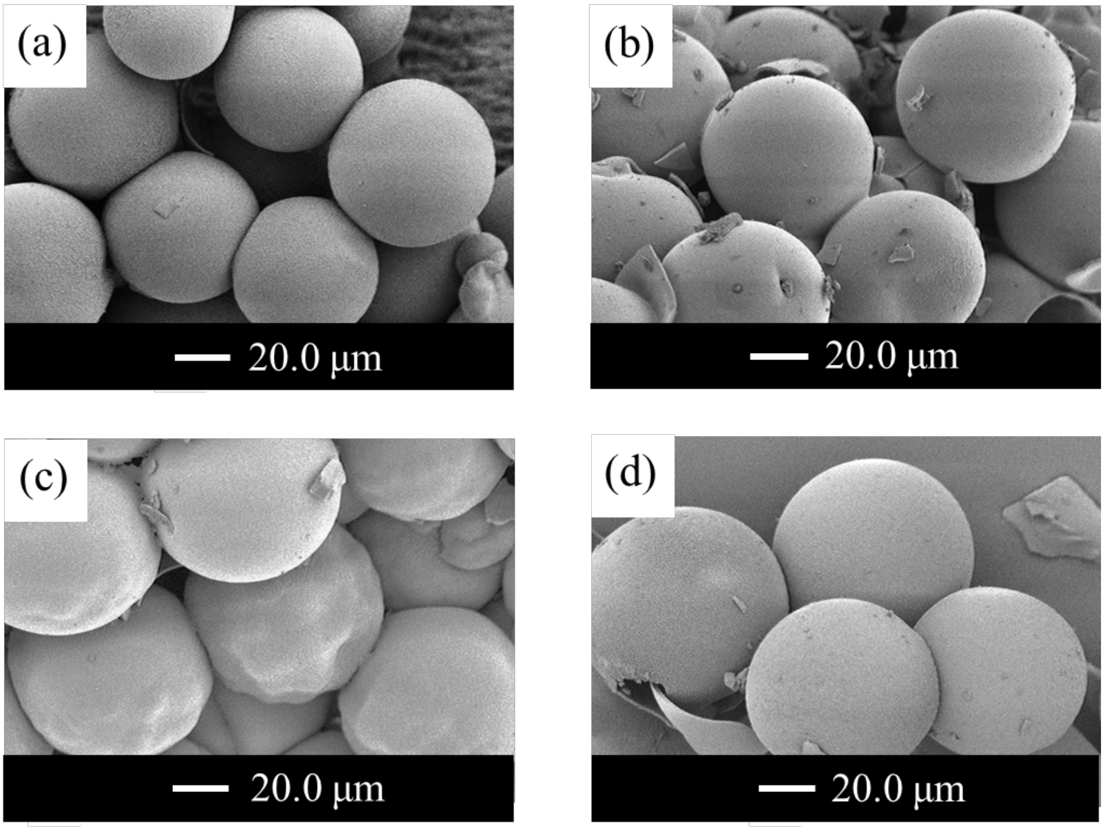

Fig. 5-1 SEM images of the (a) pure sample (only TiO_2 hollow particles), (b) the VC sample, (c) the VE sample and (d) the VC + VE sample

5.3.3 Encapsulation of VC and VE derivatives into TiO_2 hollow particles

Cross-sectional SEM images of the pure TiO_2 hollow particles), VC, and VE samples that were cut by the ion milling apparatus and element mapping of the inner surfaces are shown in Figure 5-2 (I) and (II), respectively. For the VC sample, we encapsulated the VC derivative with more sodium and sulfur, which are components of the VC derivative, than were detected in the pure sample (TiO_2 hollow particles only). Therefore, the VC derivative (water-soluble vitamin) adhered to the inner wall surface of the particles in the VC sample prepared via this process. Similarly, for the VE sample, we encapsulated the VE derivative with more carbon, which is a component of the VE derivative, than was detected in the pure sample (TiO_2 hollow particles only). Therefore, the VE derivative (oil-soluble vitamin) also adhered to the inner wall surface of the particles in the VE sample that was prepared via this process. Figure 5-3 shows SEM images and point analyses of particle surface of pure sample and VE sample by using EDS. It is impossible to simultaneously evaluate both components by element mapping because the carbon used for evaluating the VE derivative is also present in the VC derivative; however, we assumed that both the VC and VE derivatives were encapsulated in the VC + VE sample based on the above results. Encapsulation yield is mentioned in next Section 5.3.4.

Furthermore, encapsulation with VC and VE derivatives was confirmed by evaluating the release from the samples using UV–vis spectroscopy. The UV spectra of the release of the VC derivative from the VC and VC + VE samples and of the release of the VE derivative from the VE and VC + VE samples was evaluated and is shown in Figure 5-4 (I) and (II), respectively. Peaks were detected at approximately 254 nm, which is within the absorption wavelength region of the VC derivative, in the VC and VC + VE samples. Therefore, this confirmed that the VC derivative was encapsulated in the VC and VC + VE samples. As shown in Fig. 5-3 (II), peaks were detected at approximately 285 nm, which is within the absorption wavelength region of the VE derivative, in the VE and VC + VE samples. Therefore, the VE derivative was also encapsulated in the VE and VC + VE samples.

Based on these results, it was suggested that the VC and VE derivatives can be separately and simultaneously encapsulated into the TiO_2 hollow particles via the immersion method.

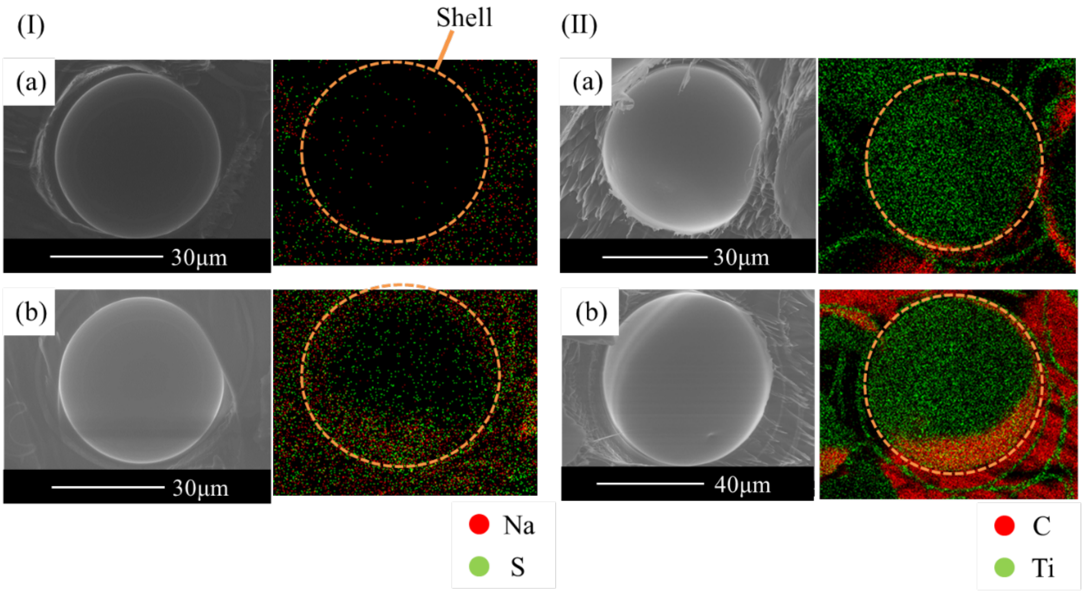

Fig. 5-2 SEM images and color mapping using EDS cross sections of (I) sodium and sulfur mapping of (a) the pure sample (only TiO_2 hollow particles) and (b) the VC sample, (II) carbon mapping of (a) the pure sample (only TiO_2 hollow particles) and (b) the VE sample.

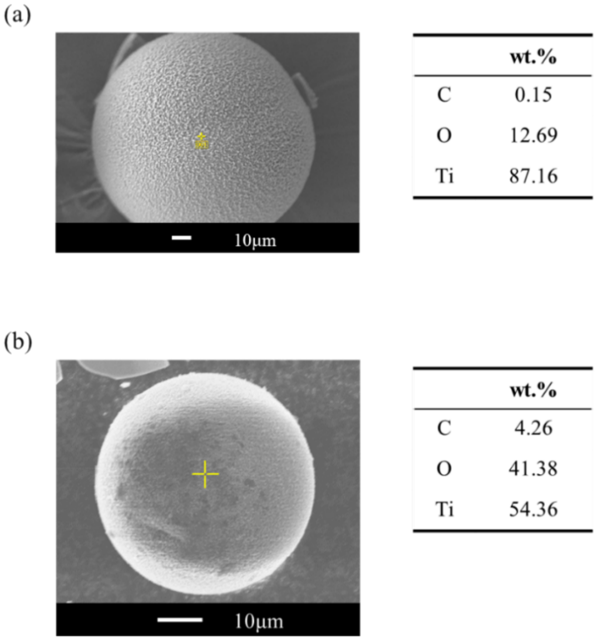

(a)

	wt.%
C	0.15
O	12.69
Ti	87.16

(b)

	wt.%
C	4.26
O	41.38
Ti	54.36

Fig. 5-3 SEM images and point analyses of particle surface of (a) sample (pure), (b) sample (VE) by using EDS.

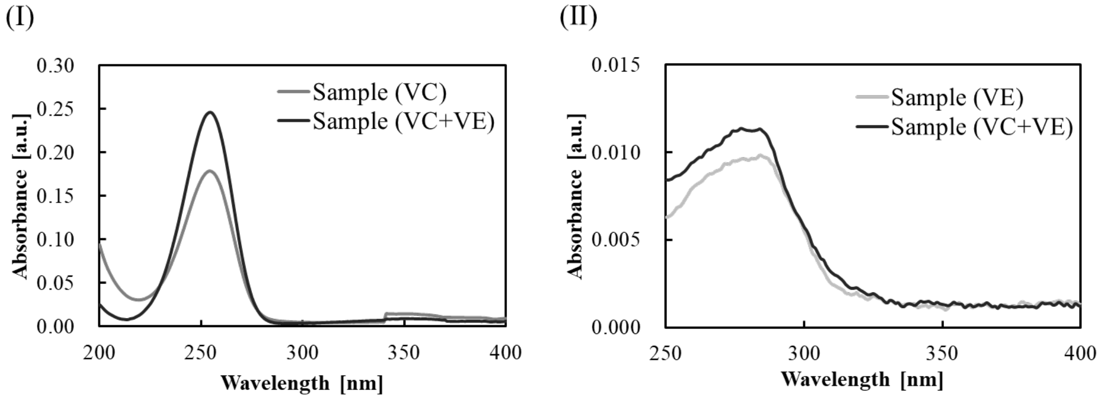

Fig. 5-4 UV–vis adsorption spectra of (I) the VC derivative in the VC sample and in the VC + VE sample and of (II) the VE derivative in the VE sample and in the VC + VE sample.

5.3.4 Sustained release of multivitamins from TiO_2 particles

The release behavior of the VC derivative in the VC and VC + VE samples and the release behavior of the VE derivative in the VE and VC + VE samples are shown in Figure 5-5 (I) and (II), respectively. As shown in these figures, for all samples, it was confirmed that the encapsulated drug substances were gradually released, and all samples exhibited sustained release. In addition, upon comparing the sample that encapsulates the single components and the multicomponent. Interestingly, it was confirmed that the release rate of the multicomponent was higher than that of the single component in the cases of both VC and VE derivatives. Based on the release rate, the yield of each component was calculated and shown in the Table 5-1. The VC amount in the multi component was increased compared the yield of single component clearly. This is discussed from the viewpoint of the surface state of the TiO_2 particles in next Section 5.3.5.

Table 5-1 Encapsulation yield of each sample based on release

Component	VC		VE	
	VC	VC+VE	VE	VC+VE
Encapsulated yield [%]	4.34	6.78	1.11	0.78

5.3.5 Surface characteristics of TiO_2 particle

The titration curve obtained via potentiometric titration is shown in Figure 5-6. The curve of the TiO_2 suspension was coincident with the blank curve on the acidic side from the isoelectric point. The isoelectric point is at a pH of approximately 4 and is on the weakly acidic side. The surface charge density of the TiO_2 hollow particles at an arbitrary pH was calculated, and the relationship is shown in Figure 5-7. As shown in Fig. 5-7, the absolute value of the surface charge density of TiO_2 is larger on the basic side than on the acidic side. This indicates that the Coulomb repulsion is large and the dispersibility is high on the basic side.[25] Then, the pH value of the immersion solution was measured to determine the state of the particle surface at the time of encapsulation of the drug substances on the three samples. As a result, the pHs of each sample were as follows: for the VC sample, pH 8.05; for the VE sample, pH 7.56; and for the VC + VE sample, pH 7.79. The magnitude relation of the pH value was VE sample <VC + VE sample <VC sample. As shown in Fig. 5-7, the surface charge densities, σ, at the time of encapsulation of the drug substances via the immersion method were as follows: for the VC sample, -0.605; for the VE sample, -0.568; and for the VC + VE sample: -0.586. On all oxides, positively charged sites that adsorb anions dominate at low pH and when σ is positive,[26] and negatively charged sites that adsorb cations dominate at high pH and when σ is negative.[27] σ was 0 or less for all our samples, and the surface of the TiO_2

particles at the time of encapsulation of the drug substances was negatively charged. However, there was a difference in σ for each sample, and the surface state of the particles was slightly different. Specifically, the σ values were in the order of VC sample < VC + VE sample, and the VC derivative existed as an anion in solution, which was easier to adsorb to the VC + VE sample than to the VC sample. The VC + VE sample had a larger adsorption amount of VC derivative on the particle surface. With this increase in adsorption amount, the release amount was increased, and the release rate became faster based on Fick's law of diffusion.

Figure 5-8 (a-1) and (a-2) show the schematic diagram of the particle surface for the VC and the VC + VE samples, respectively. As shown in Fig. 5-8 (a-1), in the VC sample, it was assumed that VC derivatives could exist as two states in solvation and hydrogen bond with on the surface because VC derivatives exist in the distilled water as anions. The phenomena could induce collisions between molecules and collision with the pore wall, and these VC derivatives would be diffused. As shown in Fig. 5-8 (a-2), in the VC + VE sample, VE derivatives, which are hydrophobic compound, stay on the surface, whereas VC derivatives, which are hydrophilic compound, dissolved in the distilled water. The phenomena indicated almost as if the hydrophobic membrane of VE may form on the surface of TiO_2. In the VC + VE sample, VC derivatives hardly interacted with the surface of TiO_2. Therefore, the release rate of the VC derivative from the VC + VE sample was faster than from the VC sample.

The release rate of the VE derivative from the VC + VE sample was faster than from the VE sample as follows. A schematic diagram of the particle surfaces for the VE and the VC + VE samples is shown in Fig. 5-8 (b-1) and (b-2), respectively. As shown in Fig. 5-8 (b-1), in the VE sample, it was assumed that VE derivatives could diffuse in solvation of VE derivatives with ethyl group. The hydroxyl group around VE derivatives may induce the hydrogen bond with O- in the surface of TiO_2. As shown in Fig. 5-8 (b-2), in the VC + VE sample, because the VE derivatives cannot adsorb on the hydroxyl group adsorbed by the VC derivatives, there must be molecules adsorbed via intermolecular interactions as well as free molecules.[28] These free molecules from the VE derivative are more easily released than molecules adsorbed via intermolecular interactions. Therefore, the adsorption states of the VE derivatives differ between the VE and VC + VE samples, and this difference affected the release rate. These results indicated the adsorption amount and release rate of the VC and VE derivatives were influenced by the particle surface that was modified by the presence of many drug substances.

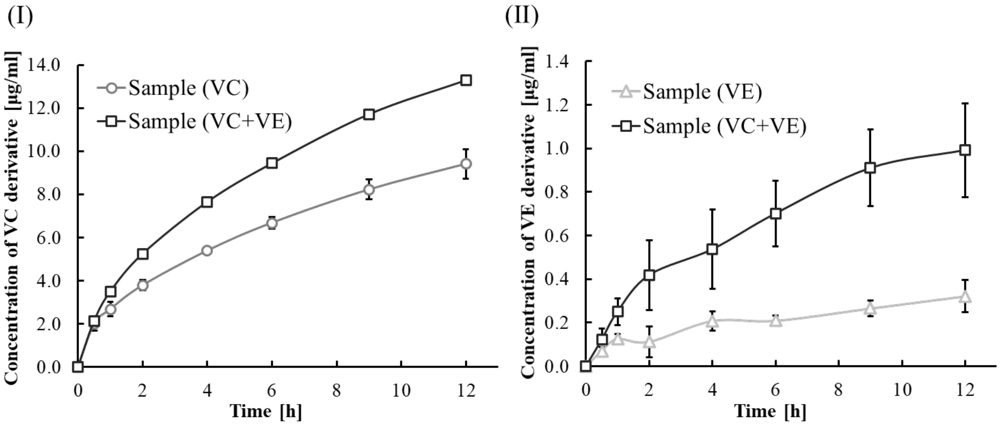

Fig. 5-5 The release profile of (I) the VC derivative from the VC sample and from the VC + VE sample and of (II) the VE derivative from the VE sample and the VC + VE sample.

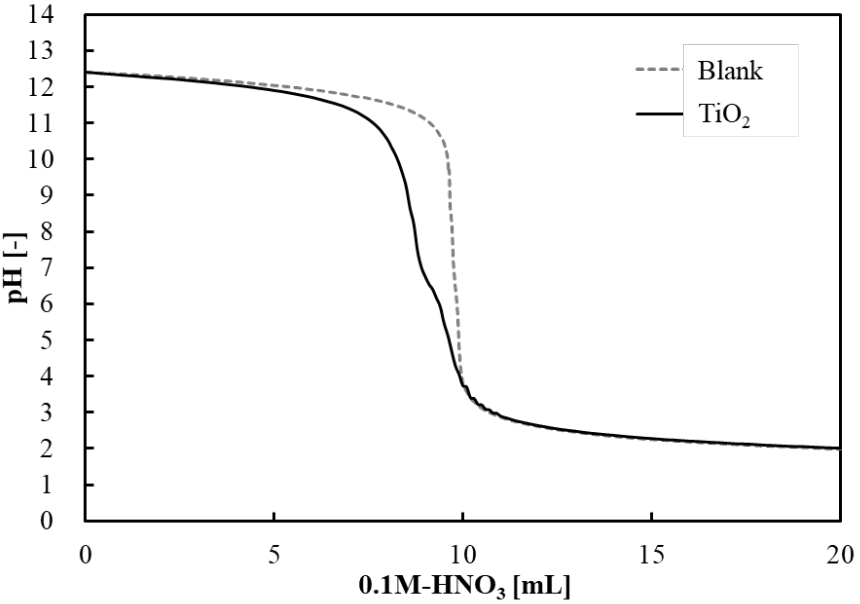

Fig. 5-6 Titration curves of the blank and TiO$_2$ hollow particles.

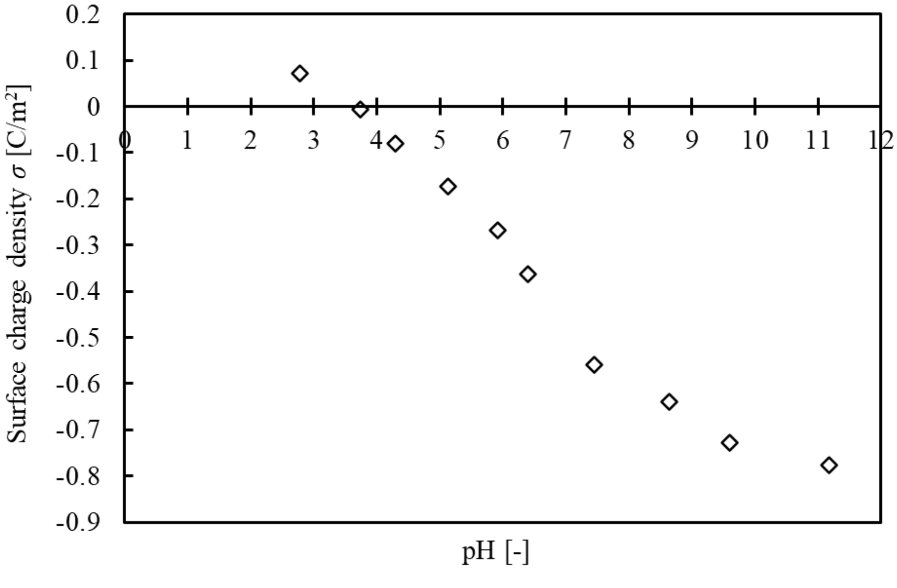

Fig. 5-7 Dependence of surface charge density of the TiO$_2$ hollow particles on pH of the aqueous solution.

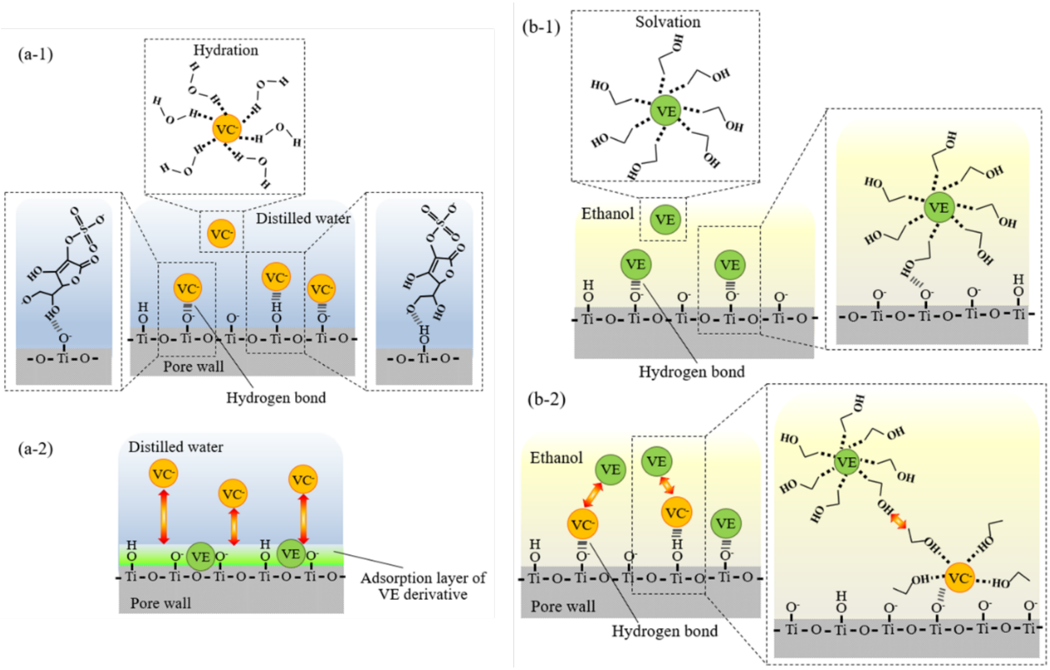

Fig. 5-8 Adsorption states of the drug substances on the particle surface of (a-1) the VC sample and of (a-2) the VC + VE sample. (b-1) the VE sample and of (b-2) the VC + VE sample.

5.3.6 Diffusion mechanism of the vitamins from TiO$_2$ hollow particles

The effective diffusion coefficient D_e, the molecular diffusion coefficient D_{AB}, and the Knudsen diffusion coefficient D_{KA} are shown in Table 5-2 for each sample. The value of VC derivative D_e in VC and VC + VE sample were 8.403×10^{-13} and D_e in VE and VC + VE sample were 1.671×10^{-13} and 11.56×10^{-13} cm^2/s, respectively; whereas that of VE derivative 4.431×10^{-13} cm^2/s, respectively. The effective diffusion coefficient of VC derivative was larger than that of VE derivative. This tendency may be attributed to the difference between hydrophilic and hydrophobic properties. Additionally, the value of effective diffusion coefficient in multicomponent was always higher than that in single component. As shown in Table 5-2, we confirmed that D_e corresponded to the results of the sustained release tests for all samples. (the release rate of the VC derivative was faster than that of the VE derivative. The release rate of the sample encapsulating the multicomponent was faster than those of the samples that encapsulates the single components.). The value of Knudsen diffusion coefficient in VC and VE derivative was 2.684 × 10^{-3} and 2.264 × 10^{-3} cm^2/s, respectively. In all samples, D_{KA} was larger than D_{AB}. This result can lead to a relation of D_0 nearly equal to D_{AB} according to Eq. 5-4, indicating that the molecular diffusion of the vitamins is dominant. Therefore, the effect of collisions between molecules was greater than the effect of collision with the pore wall. This result corresponded to the molecular diffusion in the liquid. This is because the TiO_2 particles have very small pores (approximately 3 nm); thus, few of the drug substance molecules were present in the pores. Based on these results, the diffusion mechanism of the drug substances from the TiO_2 particles was presumed for the VC, VE and VC + VE samples. Schematic diagrams of the diffusion mechanisms for each sample are shown in Figure 5-9 (I), (II) and (III), respectively. The difference in the number of vitamin molecules in the pores in each sample is caused by the difference in the molecular sizes of the VC and VE derivatives. Specifically, the VE derivative is larger than the VC derivative, and the number of molecules that can exist in the pores occurs in the following order: VE sample <VC + VE sample <VC sample. The smaller the number of molecules that are in the pores, the greater the impact of collision with the pore walls. Therefore, the VE derivative's molecules in the VE sample were mostly influenced by the collision with the pore wall, and those diffused as shown in Fig. 5-9 (II). As for the D_{AB} of the VE sample was the smallest of all samples, and the VE sample was mostly dominated by Knudsen diffusion. However, for the VC and VC + VE samples, the influence of collisions between molecules was due to more molecules being in the pores than in the VE sample, and the drug substances were

diffused, as shown in Fig. 5-9 (I), (III). For the VC + VE sample, we assumed that the collisions between different components occur in addition to collisions between the same components for the two vitamin derivatives with their different molecular sizes to exist together. As discussed with Fig. 5-8, the VE derivatives cannot adsorb on the hydroxyl group adsorbed by the VC derivatives, there have to be molecules adsorbed via intermolecular interactions. As a result, the ratio occupied by the molecular diffusion was larger than the sample encapsulated with the single component. Based on the above discussion, the diffusion of the vitamin derivatives in the pores largely depended on the relationship between the pore size and the molecular size of the drug substances.

Table 5-2 Diffusion coefficients of each vitamin derivative

Release component Sample	VC		VE	
	VC	VC+VE	VE	VC+VE
D_e [× 10^{-13} cm^2/s]	8.403	11.56	1.671	4.431
D_{AB} [× 10^{-13} cm^2/s]	7.712	10.61	1.533	4.066
D_{KA} [× 10^{-3} cm^2/s]	2.684		2.264	

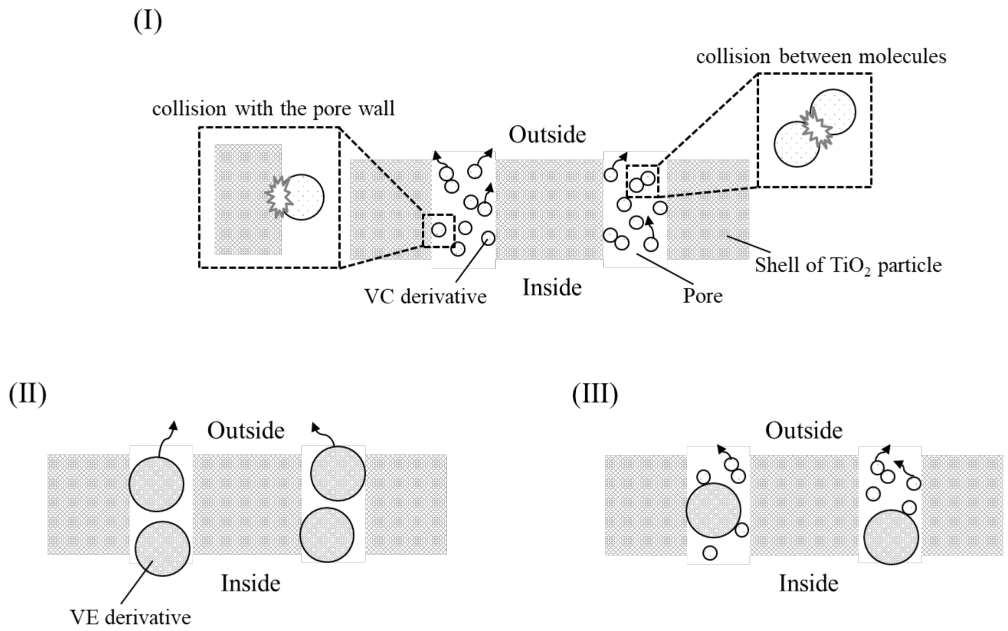

Fig. 5-9 Diffusion mechanism of (I) the VC sample, (II) the VE sample and (III) the VC + VE sample.

5.4 Conclusion

Chapter 5 describes the preparation of TiO_2 hollow particle encapsulation of two drug substances, a water-soluble vitamin and an oil-soluble vitamin, with sustained release and the diffusion mechanism of their drug substances from the obtained particles. The TiO_2 hollow particles were prepared via the inkjet process utilizing the liquid–liquid interface of the fine liquid droplets as the generation site of the particles. two drug substances were simultaneously encapsulated into the TiO_2 hollow particles via the immersion method. This encapsulation did not affect the particle shape. In addition, the adhesion of the two drug substances onto the outer and inner surfaces of the particles was confirmed by element analysis and analysis by UV–vis spectrophotometry. According to the sustained release test, the obtained particles exhibit sustained release.

Based on the sustained release test results, the particles encapsulating the VC and VE derivatives released their drug substances faster than the particles encapsulating the single components separately. This is because of the difference in the adsorption amount and adsorption state of the drug substances, which was caused by differences in the particle surfaces at the time of encapsulating via the immersion method. The diffusion mechanism for the drug substances differs for each sample because of the difference in the molecular sizes of the drug substances.

*This chapter was reproduced and modified from [*Adv. Powder Technol.,* 2019, **30**, 2989–2996], with permission from Elsevier.

References

[1] K. Kadota, H. Tamura, Y. Shirakawa, Y. Tozuka, A. Shimosaka, J. Hidaka, *Chem. Eng. Res. Des.*, 2014, **92**, 2461–2469

[2] T. Tanaka, K. Kadota, Y. Tozuka, A. Shimosaka, Y. Shirakawa, *Ceram. Int.,* 2016, **42**, 9963– 9971

[3] Y. Tominaga, K. Kadota, K. Oshima, A. Shimosaka, M. Yoshida, Y. Shirakawa, *J. Ceram. Soc. Jpn.,* 2019, **127**, 254–262

[4] Y. Tominaga, K. Kadota, A. Shimosaka, M. Yoshida, K. Oshima, Y. Shirakawa, *J. Crystal Growth*, 2018, **490**, 11–18

[5] A. C. Galvão, W. S. Robazza, A. D. Bianchi, J. A. Matiello, A. R. Paludo, R. Thomas, *J. Chem. Thermodynamics*, 2018, **121**, 8-16

[6] M. D. Dubbs and R. B. Gupta, *J. Chem. Eng. Data*, 1998, 43, 590-591

[7] K. Jono, H. Ichikawa, Y. Fukumori, Y. Uwamino, *Adv. Powder Technol.*, 1998, **9**, 363–375

[8] S. Wang, X. Wang, H. Xu, H. Abe, Z. Tan, Y. Zhao, J. Guo, M. Naito, H. Ichikawa, Y. Fukumori, *Adv. Powder Technol.* 2010, **21**, 268–272

[9] J.-X. Wang, Z.-H. Wang, J.-F. Chen, J. Yun, *Mater. Res. Bull.*, 2008, **43**, 3374–3381

[10] W. Hanson, Theoretical concepts, in: *Handbook of Dissolution Testing*, Pharmaceutical Technology Publications, 1982

[11] Y. Toomari, H. Namazi, *Int. J. Polym. Mater. Polym. Biomater.*, 2016, **65**, 10, 487–496

[12] E. Lason´ , E. Sikora, J. Ogonowski, M. Tabaszewska, Ł. Skoczylas, *Colloid. Surf. A.*, 2016, **510**, 87–92

[13] S. Huang, J. Wang, Q. Shang, *J. Biomater. Sci., Polym. Edit*, 2017, **28**, 2, 194–206

[14] N. D. Stebbins, M.M. Moy, J.J. Faig, K.E. Uhrich, *J. Bioact. Compat. Polym.*, 2017, **32**, 2, 196–208

[15] X.-H. Wei, Y.-P. Niu, Y.-Y. Xu, Y.-Z. Du, F.-Q. Hu, H. Yuan, *J. Bioact. Compat. Polym.,* 2010, **25**, 3. 19–335

[16] M. Murakami, Y. Morita, T. Koide, H. Saito, T. Tanimoto, *Bull. Natl. Inst. Health Sci.,* 2003, **121**, 068–070

[17] L. S. Cerovic, S.K. Milonjic, D. Bahloul-Hourlier, B. Doucey, *Colloid. Surf. A.*, 2002, **197**, 147–156

[18] K. C. Akratopulu, C. Kordulis, A. Lycourghiotis, *J. Chem. Soc., Faraday Trans.*, 1990, 86, **20**, 3437–3440

[19] R. T. Yang, R.T. Liu, *Ind. Eng. Chem. Process Des. Dev.*, 1979, **18**, 2, 245–249

[20] O. Šolcová, H. Šnajdaufová, P. Schneider, *Chem. Eng. Sci.* 2001, **56**, 17,

5231–5237

[21] Y. Nakasaka, T. Tago, K. Yano, Y. Masuda, *Zeolite*, 2011, **28**, 47–54

[22] M. Grujić-Brojčin, S. Armaković, N. Tomić, B. Abramović, A. Golubović, B. Stojadinović, A. Kremenović, B. Babić, Z. Dohčević-Mitrović, M. Šćepanović, *Materials Characterization*, 2014, **88**, 30-41

[23] S. Nagamine, A. Sugioka, Y. Konishi, *Mater. Lett.,* 2007, **61**, 444–447.

[24] V. Loryuenyong, K. Angamnuaysiri, J. Sukcharoenpong, A. Suwannasri, *Ceram. Int.*, 2012, **38**, 2233–2237.

[25] B. Tyliszczak, A. Sobczak-Kupiec, K. Bialik-Was, W. Kasprzyk, *J. Nanosci. Nanotechnol.*, 2012, **12**. 9312–9318.

[26] H. Tamura, *Resource Process.*, 1998, **45**, 4, 276–281.

[27] H. Tamura, R. Furuichi, *J. Jpn. Soc. Anal. Chem.* 1991, **40**, 11, 635–640.

[28] M. Otsuka, *J. Surf. Sci. Soc. Jpn.* 2001, **22**, 1, 36–45.

Chapter 6

Assessment of amorphization behavior of a drug during co-grinding with an amino acid

6.1 Introduction

In Chapter 6, the ball milling process of drug substance and amino acid is described as solid–solid interfacial phenomena affecting particle characteristics which is difficult to observe experimentally. New drug candidates tend to have low solubility, and currently over 75% of drug candidates fall into Class II of the Biopharmaceutics Classification System (BCS).[1] Low solubility limits the therapeutic efficacy of these drug candidates. Therefore, several approaches to addressing this problem have been reported.[2,3] Although salt formation and co-crystallization greatly improve solubility and dissolution profiles, ideal salt candidates are difficult to identify for drug candidates that contain ionic bonds. In contrast, amorphization is theoretically applicable to all drugs, where the dissolution rate of disordered drugs could be enhanced by their increased energy.[4] It has been reported that the amorphous state can be produced in several ways, such as vapor condensation, supercooling liquid, precipitation from solution, and disruption of the crystalline lattice.[5] However, this means unexpected amorphous state can be generated under several situations, such as jet-milling. Also the high-energy state of a compound derived from amorphization is chemically and physically unstable, resulting in re-crystallization or the generation of impurities during storage.[6] Several co-amorphous drug–drug and drug-excipient systems have been studied to overcome the issues.[7,8] As one of the sophisticated way, drug–drug systems could be administered in combination therapy but may not be practical due to the high dose required for one drug. In contrast, drug-excipients may be widely applicable as an alternative to the use of polymers, with drug–amino acid systems being a particularly promising combination.[9,10] Amino acids have a low molecular mass and can increase the drug load in the formulation due to interactions between their functional groups and the drug. Intimate mixing of an amorphous drug and amino acid at the molecular level has been attempted by quench cooling, ball milling, cryo-milling, and spray drying.[11,12] Ball milling is a widely used process for amorphizing drugs by solely using mechanical force in which ball–ball and ball–wall friction provides local intense energy to the raw materials.[13] In planetary ball milling, centrifugal forces are alternately synchronized since the bowl and disc turn in opposite directions and ball–ball and ball–wall frictional energy likely dominates the mechanochemical reaction during grinding.[14] The amorphization of drugs by ball milling is complicated by the coupling of mechanical and chemical phenomena at the molecular scale since each molecule is different due to thermal or photochemical reactions.[15] The effect of an amino acid on the amorphization mechanism remains unknown, as most previous studies have focused on the physicochemical properties and improvements in dissolution behavior provided by the amorphous state, not on the amorphization process by ball milling.[16]

Balls in a planetary ball mill are moved along the wall by centrifugal force and this force increases as the rotation speed of the mill increases.[17] Friction is produced by differences in speed between a ball and the wall of the vessel and this frictional energy acts on the samples being milled. Increasing revolution speed increases the Coriolis force (rotation bias force) applied to the balls and they detach from the wall.[18–20] Ball behavior during planetary ball milling was previously modeled using DEM and an appropriate geometrical relationship for the motion of a ball in the grinding mill.[21,22]

In this Chapter 6, discrete element method (DEM) simulations was conducted to investigate the relationship between frictional energy and the amorphization of a drug with an amino acid during ball milling. Indomethacin (IMC) was selected as a model poorly water-soluble drug as it has been widely studied by various amorphization techniques.[23,24] Cystine (Cys2) is an amino acid dimer whose disulfide bond is easily broken and may form reactive radicals when strongly impacted.[25,26]. The amorphous state is achieved by ball milling by disrupting the crystalline state of the raw materials however it is difficult to predict the frictional energy during ball milling due to the complex non-linear motion of balls in the closed system.[27,28]. Consequently, DEM simulation was performed to estimate the frictional energy as an input parameter during ball milling.[29] Changes in the amorphization of IMC and Cys2 were determined simultaneously by collecting X-ray powder diffraction (XRPD) spectra before and after milling and analyzing by principal component analysis (PCA). The results allowed estimation of the amorphization of IMC with Cys2 during co-grinding from the relationship between the frictional energy and the PCA score. The involvement of radical formation in the amorphization of IMC with Cys2 was investigated by electron spin resonance measurements.

6.2 Materials and Methods

6.2.1. Materials and Preparation of ground samples

Indomethacin (IMC) and cystine (Cys2) were purchased from Nakarai Tesque, Inc. (Japan). The effect of the molar ratio of IMC and Cys2 on amorphization was investigated by using several combinations of the two compounds and measuring their X-ray powder diffraction (XRPD) diffractograms (Supplementary Fig. S1). Most experiments were conducted using a 1:1 molar ratio (1.180 g IMC and 0.794 g Cys2).[30] IMC and Cys2 were mixed in a mortar before co-grinding and stored in a desiccator at 20%RH (controlled by silica gel) at room temperature. A planetary ball mill, Pulverisette 7 from Fritsch GmbH (Germany), was used for grinding at room temperature. Eight YTZ balls (10 mm diameter) were placed in the 45 mL zirconia vessel and the revolution rate was 1:-2. This ratio provided effective grinding regardless of the rotation speed, based on the calculated critical speed ratio.[31] Grinding time was defined as the total time and was conducted in 10 min intervals to avoid over-heating the milling vessel. The maximum rotation speed was 600 rpm and the maximum grinding time was 10 h. Ground samples were analyzed by XRPD, Fourier transform-infrared spectroscopy (FT-IR), and dissolution tests, as described below.

6.2.2. X-ray powder diffraction (XRPD)

XRPD analyzes were performed on 20.0 mg samples at a 200-mA current and a 40-kV voltage using Cu-Ka radiation (l = 0.15418 nm) on a SmartLab diffractometer (Rigaku Corporation, Japan). The scan range was 2θ= 5–45° at a rate of 4.0° /min with a 0.01° step interval.

DEM software (DEM solutions, EDEM) was used to predict planetary movement of a ball in the milling vessel. The method was used to simulate ball motion and analyze the energy generated from collision and friction between balls within the planetary ball mill.[32] The mechanical properties used in DEM simulation are shown in Table 6-1.[33] The Voigt model provides the elastic relationship between the contact force and displacement of the particles, allowing two contacting particles to slip relative to each other, thereby introducing ball–ball and ball–wall frictional forces. The mass of the raw materials was relatively small compared to the mass of the balls and therefore had little effect on the movement and energy of the balls, despite occupying an appreciable volume inside the mill. Dynamic behavior calculated using the force on the balls, and the locations of the balls in the milling vessel during grinding, were simulated for 10 min. The number of ball–ball and ball–wall contacts was counted. The frictional energy per second (specific frictional energy, E_f) was calculated according to the following equation:

$$E_f = \frac{1}{WT}\sum_{j=1}^{n_c} \mu_D F_n \, u_j \tag{6-1}$$

where W is the loading amount of the balls, T is the simulation time, μ_d is the dynamic frictional coefficient, F_n is the normal contact force between ball–ball and ball–wall, N_c is the contact time, and u_j is the tangential component of relative displacement at each.

6.2.3. ESR (Electron spin resonance)

Electron spin resonance (ESR) was analyzed by using ESR spectrometer (JEOL Co., Tokyo, Japan). About 30 mg of samples was put into a quartz ESR tube (φ = 5 mm). The optimized conditions were shown in Table 6-2.[34]

6.2.4 FT-IR (Fourier transform-infrared spectroscopy)

The IR spectra of samples were collected using an FT/IR-6100 from JASCO Corporation (Japan). The measurements were performed on samples pelletized with KBr at a 1:40 weight ratio after mixing and milling using a pestle and mortar. Scans were obtained from 400 to 4000 cm^{-1} at 4 cm^{-1} resolution and 30 scans were averaged per spectrum.

Table 6-1 Parameter settings for DEM simulation

Object	Setting parameter	Set value	unit
Ball	Density of particle	6000	kg/m^3
	Poisson's ratio	0.30	-
	Young's modules	210	GPa
	Coefficient of restitution	0.899	-

milling	Coefficient of static friction	0.220	-
	Coefficient of rolling friction	1.0 x 10^{-5}	-
	Number of balls	8	EA
	Diameter of particle	10.0	Mm
	Rotation speed	200, 250, 300, 400, 600	rpm
	Mill diameter	40.0	mm
	Mill depth	40.0	mm
	Revolution radius	70.0	mm
	Rotation-to revolution speed ratio	1.00 : (-) 2.00	-

Table 6-2 Optimized analytical conditions of ESR measurement

Setting parameter		Set value	unit
Microwave	Power	1	mW
	Frequency	9.448	GHz
Magnetic field	Center field	336.0	mT
	Sweep width	10	mT
Signal channel	Modulation frequency	2.50	kHz
	Modulation width	2.0	mT
	Time constant	0.03	s
	Sweep time	1	min
Temperature		Ambient	°C

6.2.5 Dissolution test

Dissolution tests were performed at a paddle rotation speed of 50 rpm in a 900-mL vessel using an NTR-8000AC (Toyama Sangyo, Japan). The concentration of IMC in the sample was measured at 5, 10, 15, 30, 45, 60, 120, and 180 min. Each 5.0 γ-IMC sample was mixed with 900 mL purified water at 37.0 ± 0.5 °C. Samples (2 mL) were removed at each time point and filtered through a 0.2 mm PTFE filter. Samples (10 mL) were analyzed by HPLC with acetonitrile: phosphoric acid (0.1%) = 70 : 30 as the mobile phase at a flow rate of 1.0 mL/min. Column temperature was set to 40 C and IMC was detected by UV at 320 nm.

6.2.6 Statistical analysis

One way analysis of variance was used to compare the mean dissolution rate after 180 min of mixing of untreated IMC, the IMC/ Cys2 physical mixture, and ground IMC. A value of $P < 0.05$ was considered significant throughout the study.

PCA was performed on the XRPD spectra. First, all spectra were centered and scaled to maximum intensity. PCA was used to help interpret differences in the XRPD spectra of samples prepared using different milling conditions. Prior to PCA, a standard normal variant transformation was performed on the spectra to remove intensity differences unrelated to sample composition and the spectra were then mean-centered. PCA was performed on the spectral range from 16 to 32° using JMP® ver. 11 statistical software (SAS Institute Japan Ltd.).

6.3 Results and discussion

6.3.1. XRPD analysis of the structural change of IMC following co-milling with Cys2

Figure 6-1 shows the XRPD patterns of untreated IMC, Cys2, the IMC/Cys2 physical mixture, and IMC and Cys2 separately ground at 600 rpm for 3 h. All XRPD patterns were normalized to the maximum intensity of the first peak for each spectrum. The XRPD patterns of untreated IMC and Cys2 were fitted well with the patterns of the γ-form of IMC with the space group P-1 in the triclinic crystal system, and with the hexagonal form of Cys2 with the non-centrosymmetric space group $P6_122$.[35,36] The specific first and second peaks due to IMC and Cys2 appeared at $2\theta = 21.9$ and 26.7 (IMC),18.9 and 28.5 (Cys2) degrees, respectively. The IMC and Cys2 peaks gradually decreased compared with the first specific peak before grinding, as shown in Fig. 6-1. The relative intensities of the IMC peaks remained essentially unchanged after grinding at 600 rpm for 3 h (Fig. 6-1), whereas comparable grinding resulted in the Cys2 peaks broadening throughout the spectrum, indicating that the crystallinity of Cys2 gradually decreased or converted into the amorphous state. The Cys2 peaks at 18.9 and 28.5° derive from the (0001) plane normal to the c-axis of the crystal.[37] This plane might be maintained by N—H···O hydrogen bonds between the charged $—COO^-$ and $—NH_3^+$, a major structural characteristic of zwitterionic amino–acid crystals.[38] The 79.84 kJ/mol by Aceves-Hernandez et al.[39]. Several IMC peaks at $—COO^-$ and $—NH_3^+$ interaction energy was estimated to be 11.6 and 21.9° were previously identified in the diffraction plane at (110) and (21-1), respectively.[35] These peaks are related to the interactions between molecules and an estimated bond energy of 66.72–93.30 kJ/mol.[40] The difference in hydrogen bond strength between IMC and Cys2 may be due to differences in their crystallinity following impact during grinding. Figure 6-2(a) shows the XRPD patterns of IMC/Cys2 before grinding (initial) and after co-grinding at a mill rotation speed of 200, 250, 300, 400, and 600 rpm for 3 h. Fig. 6-2(b) shows the XRPD patterns of IMC/Cys2 co-ground at 400 rpm for 0.5, 1, 2, 3, 5, and 10 h. The XRPD patterns in Fig. 6-2(a) and (b) changed from sharp to broad peaks, indicating that crystalline IMC was gradually converted into an amorphous state as the rotation speed of the mill and the grinding time increased, although all spectra showed that some IMC crystals remained. The intensities of the first and second peaks in IMC and Cys2 crystals decreased but did not show an amorphous halo pattern in each spectrum, again indicating residual crystallinity in the IMC/Cys2 system. More severe conditions would be required to obtain completely amorphous IMC/Cys2. The reduction in crystallinity of each sample type was determined by calculating the degree of crystallinity from the XRPD spectra using the representative peaks intensity at 21.9 and 26.7° for IMC and at 18.9 and 28.5° for Cys2 and Eq. 6-2.

$$\text{crystallinity} = 1 - \frac{peak\ intensity,\ xmin}{peak\ intensity,\ 0min} \tag{6-2}$$

Figure 6-3 shows the degree of crystallinity of (a) IMC and (b) Cys2 following single (individual) grinding and co-grinding at 400 rpm for 0.5, 1, 2, and 3 h, where the degree of crystallinity of IMC or Cys2 was calculated using Eq. 6-2. The amorphization of IMC during co-grinding with Cys2 progressed faster than during single grinding whereas the amorphization of Cys2 progressed more slowly during co-grinding than during single grinding. These results suggested that Cys2 promotes the amorphization of IMC during co-grinding. As mentioned above, IMC has a cyclic dimeric structure formed amino groups that can form hydrogen bonds and therefore might through O—H…O=C hydrogen bonds. Cys2 has carboxylic and affect the dimeric structure of crystalline IMC during the co-grinding process. This result is discussed further in the following section.

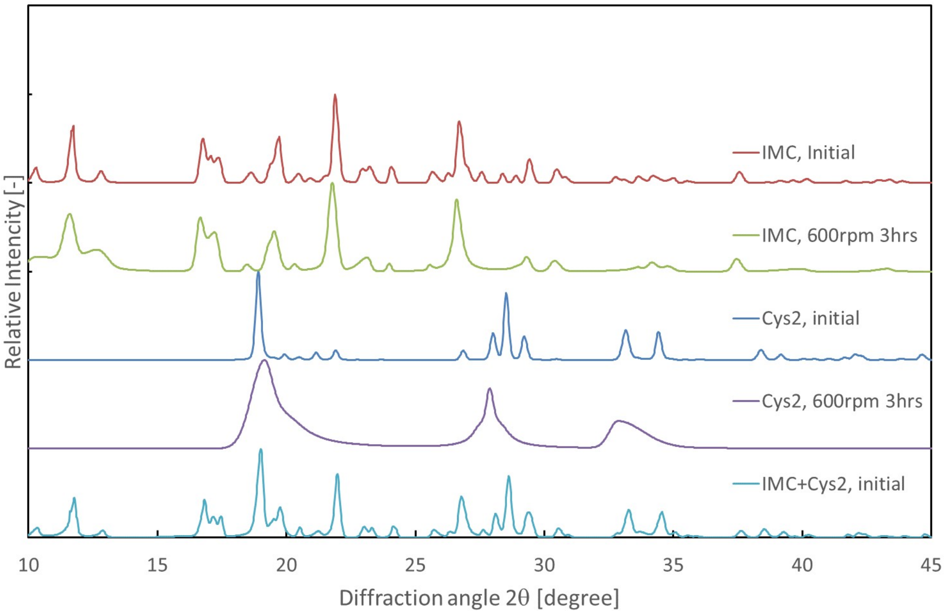

Fig. 6-1 XRPD patterns for untreated IMC, Cys2, the physical mixture of IMC/Cys2, and IMC and Cys2 ground at 600 rpm for 3 h.

(a)

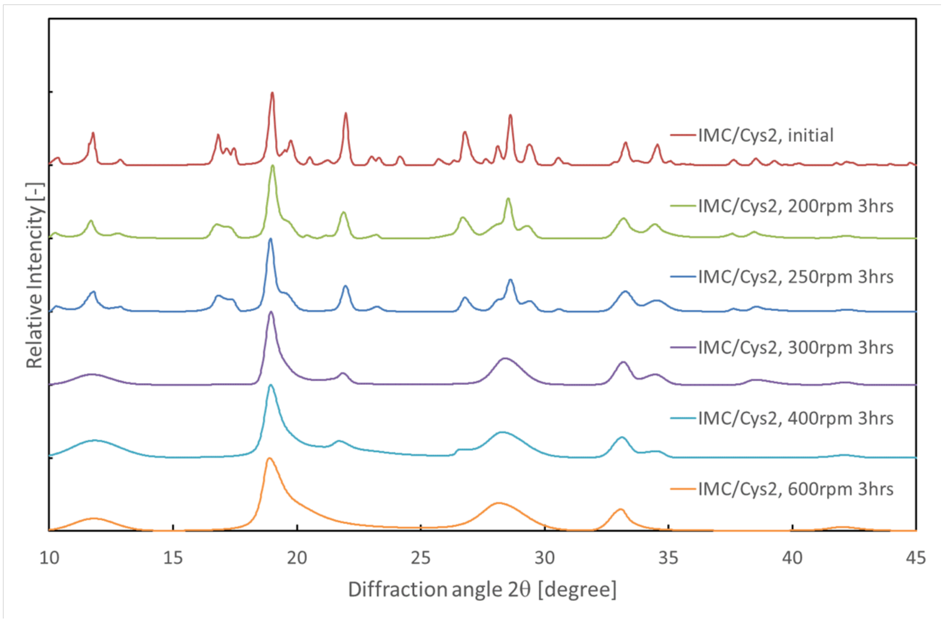

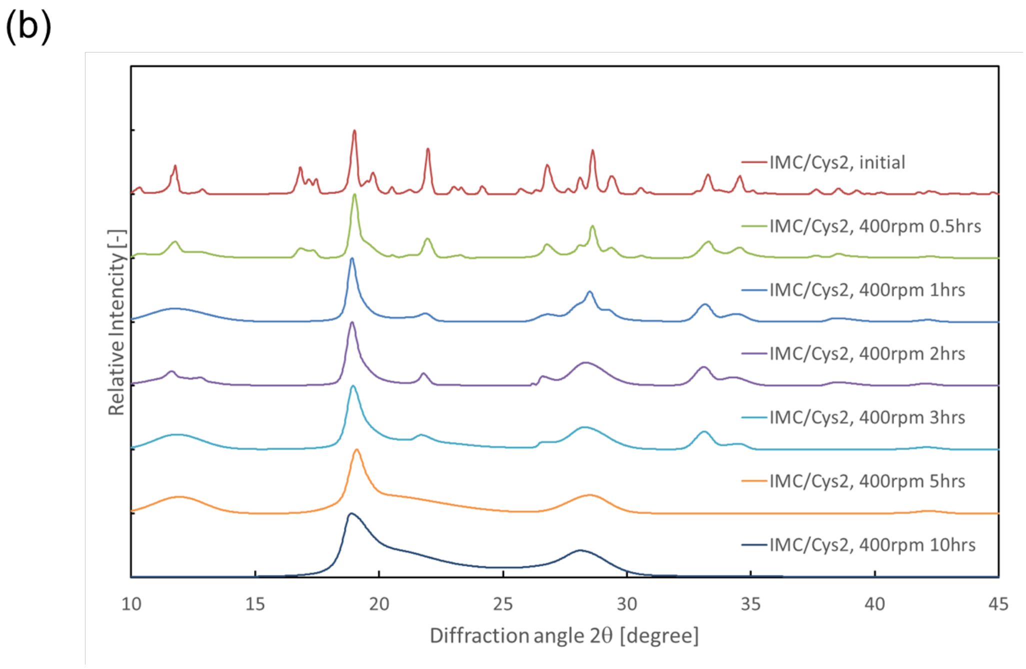

Fig. 6-2 XRPD patterns of IMC/Cys2 co-ground (a) at 200, 250, 300, 400, and 600 rpm for 3 h, (b) at 400 rpm for 0.5, 1, 2, 3, 5, and 10 h.

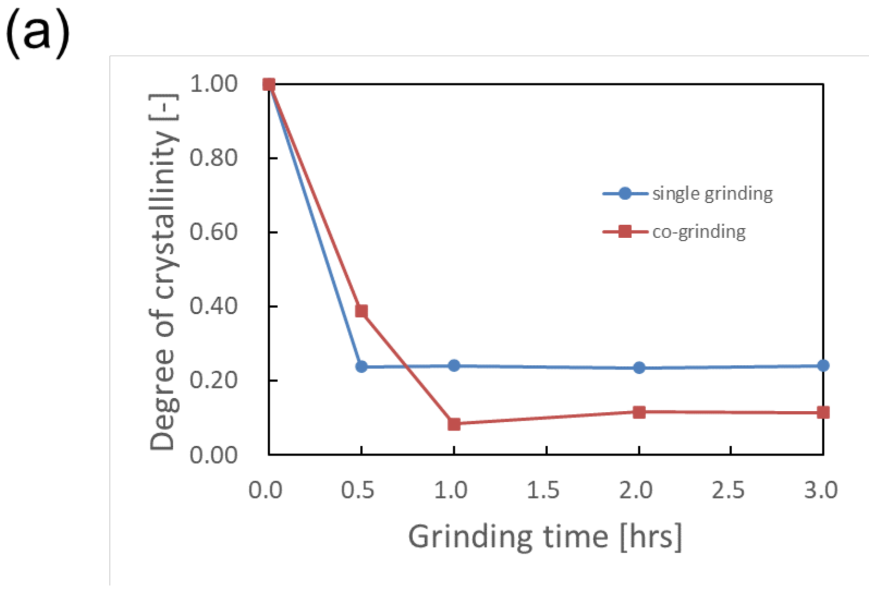

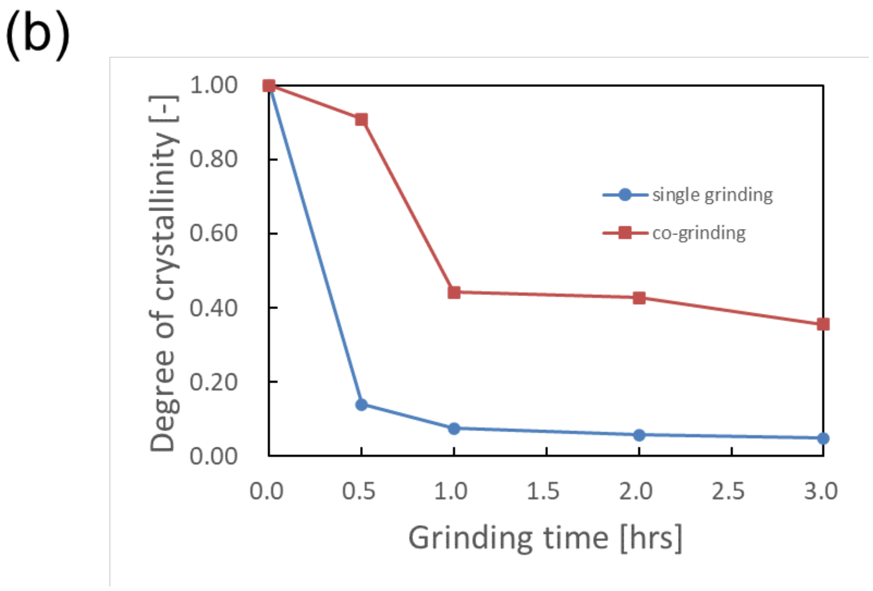

Fig. 6-3 Comparison of the degree of crystallinity of (a) IMC and (b) Cys2 between single grinding and co-grinding at 400 rpm for 0.5, 1, 2, and 3 h.

6.3.2 Amorphization of IMC with Cys2 as analyzed by DEM simulation

The results correlated well with the results of stimulated grinding and the input energy estimated by DEM simulation.[41,42]. Figure 6-4 shows (a) the total number of contacts between a ball and a ball-wall with time and (b) the distribution of the tangential force between a ball and a ball/wall averaged per time step in the DEM simulation. As shown in Fig. 6-4(a), the total number of contacts between a ball and a ball/wall increased linearly with grinding time, irrespective of the rotation speed of the mill. However, the correlation with the rotation speed of the mill was complicated due to the intricate movement of the balls in the mill. As the rotation speed increases, the number of contacts per unit time increases due to the increased speed of the balls, even though the distance between the balls increases. Therefore, the maximum number of contacts was obtained at 600 rpm. The distribution of the tangential force shifted to a higher mean value and became broader as the rotation speed of the mill increased (Fig.

6-4(b)). Mio et al.[28] reported that the number of contacts remained constant during milling at a specific rotation speed, and that the rotation speed of the mill affects the impact energy of the balls, resulting in the high energy imparted to the balls during milling within a specific critical ratio. Guzman et al.[33] demonstrated a distribution in translational velocity in the grinding vessel. However, the differences of the translational velocity support the argument for calculating the average kinetic energy of each ball as the average kinetic energy for the model. The specific energy transferred to the powdered sample is critical for amorphization and describes the maximum amount of energy which can be supplied to the raw material during one collision.[18].

The relationship between frictional energy and amorphization was clarified by calculating the specific frictional energy for each rotation speed of the mill by DEM simulation. The simulation included non-linear behavior of the balls because of a good indicator to free from specific settings of parameters.[42] Figure 6-5 shows the parabolic relationship between the revolution speed of the mill and specific frictional energy of a planetary ball mill as calculated by DEM simulation. This specific frictional energy acts momentarily and constantly to advance the amorphization of crystalline IMC and Cys2 during grinding. As described in the XRPD the amorphous state of IMC/Cys2 was physically stable and the amount of amorphous material increased as the impact from grinding increased. The total frictional energy was calculated as the summation of the time required to amorphize each material and the input energy due to impact.

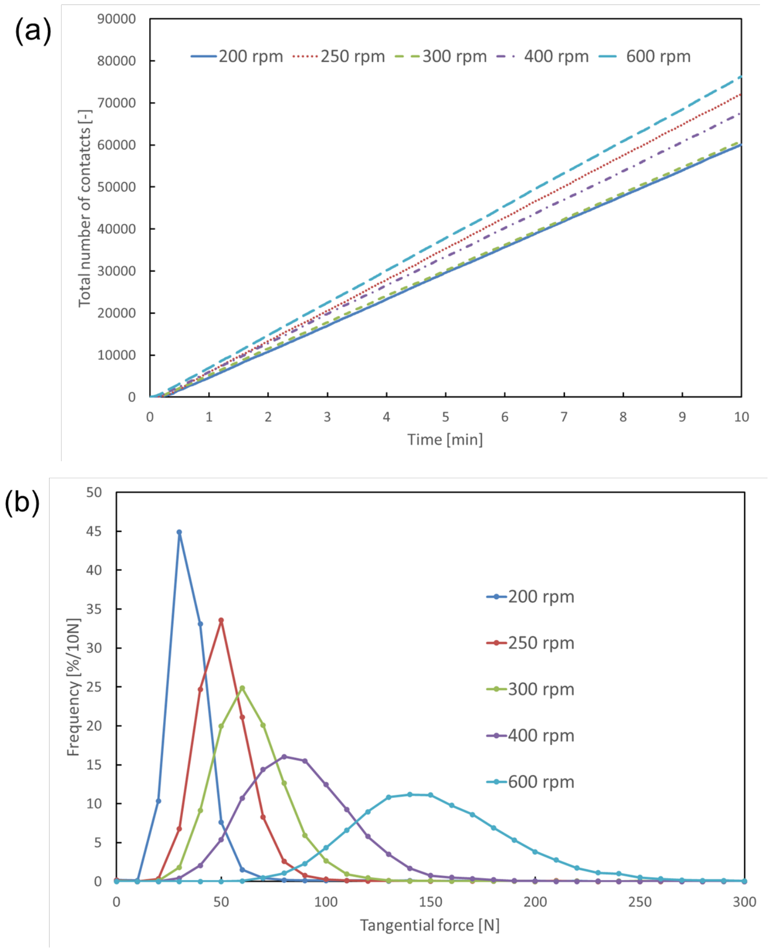

Fig. 6-4 DEM simulation results, (a) Total number of contacts and (b) Tangential force distribution at different rotation speeds of the mill.

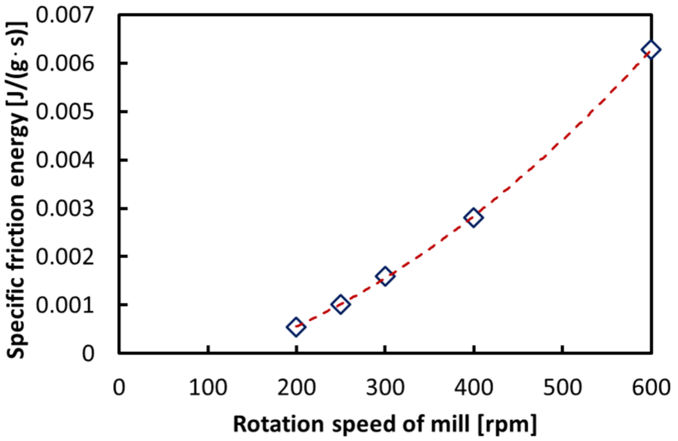

Fig. 6-5 Specific frictional energy, E_f, estimated by DEM simulation as a function of the rotation speed of the mill.

6.3.3 Principal component analysis (PCA)

PCA is a fundamental tool in exploratory data analysis and can help reveal trends in the data. Wise and Gallagher described PCA as a favorite tool of chemometricians for compressing data and extracting information and noted that PCA identifies combinations of variables or factors that describe major trends in a data set.[43] The amorphization of each material during co-grinding was clarified by analyzing all XRPD spectra of the physical mixture of IMC/Cys2 and of the co-ground samples by PCA. The results for the XRPD data indicated that IMC/Cys2 samples were composed of 2 principal components (PCs) that explained about 80% (1st: 59.5% and 2nd: 19.1%) of the variance in the data set from $2\theta = 16^{\circ}$ to 32° the XRPD spectra. Figure 6-6(a) shows the loading of the 1st PC, 2nd PC, and of the XRPD spectra of untreated IMC and of untreated Cys2. The loading profiles indicated that each PC was characterized by the peaks in the XRPD spectra. Loading of 1st PC has profile to make a negative pair for IMC and Cys2 peaks. The values of the 1st and 2nd PCs were calculated as linear combinations of the XRPD spectra pretreated by a standard normal variant treatment and these loadings. Broader spectra, as seen for amorphized samples, provide higher values. Therefore, the score of the 1st PC was mainly related to the degree of amorphization of the IMC/Cys2 system. In the same way, the loading profile of the 2nd PC was similar to spectra of untreated IMC positively. Therefore, 2nd PC score indicated for likelihood of IMC.

Fig. 6-6(b) shows the relationship between the 1st PC score and the total ratio of the amorphous state vs. the total frictional energy as calculated by DEM simulation. The total ratio of the amorphous state, a, was calculated from the following equation and compared with the values calculated from the XRPD spectral data:

$$\alpha = \frac{I^a_{IMC}+I^a_{Cys2}}{I^b_{IMC}+I^b_{Cys2}} \tag{6-3}$$

where I_a is the peak intensities of the initial state, I_b is the peak intensities after co-grinding, I_{Cys2} is the averaged peak intensity of the Cys2 first and second peaks, and I_{IMC} is the averaged peak intensity of the IMC first and second peaks. The 1st PC score increased as the total frictional energy increased. The adjusted coefficient of determination between the total frictional energy and the 1st PC score is 0.895, which is sufficient to show linearity. The value of a rose logarithmically with the total frictional energy and the coefficient between the total frictional energy and logarithmic a was 0.379. IMC had anisotropic mechanical properties and amino acids are typical examples of molecular solids with directional intermolecular interaction.[44,45] Co-grinding triggered IMC and Cys2 to adopt the amorphous state when the specific frictional energy surpassed the yield stress of the γ-form of the IMC and Cys2 crystals. As mentioned in the previous section, the total frictional energy reflects frictional force distribution and grinding time. Thus, the linearity between the total frictional energy and the 1st PC means that even the frictional force at 200 rpm was sufficient to initiate amorphization. The difference between the linearity of the 1st PC and a and the total frictional energy can be explained by the different range of the XRPD spectra used to calculate the degree of the amorphous state. As mentioned above, a was only considered with intensity of first peaks of IMC and Cys2 crystals. However, changes from the crystalline to the amorphous state were evident in the XRPD spectra. PCA suggested that the degree of amorphization of the IMC/Cys2 system during co-grinding in the planetary ball mill progress as 1st PC score according to the total friction energy shown in Fig. 6-6(b). Figure 6-7 shows the score plots for each co-grinding condition, with the

1st PC as the horizontal axis and the 2nd PC as the vertical axis for different rotation speeds (400 and 600 rpm) and times. The 1st PC score increases with longer grinding time and faster rotation speed whereas the 2nd PC score approached 0, indicating loss of IMC crystallinity. The 2nd PC score then increased as the total frictional energy increased. In other words, first IMC, then Cys2, lost crystallinity. The increase in the 2nd PC score reflects the remaining IMC crystallinity. These results show that amorphization of the IMC/Cys2 system is described by the trajectory for the 1st and 2nd PC and is not a self-reversible process during co-grinding due to the high friction in the mill, as shown in Fig. 6-4. The differences in the amorphization process between IMC and Cys2 described in the previous sections are also supported by the PCA scores and are consistent with the XRPD diffractograms. XRPD diffractograms in theory provide significant information based on mechanistic theory but statistical approaches are also useful for understanding the re-crystallization processes of complex systems from the amorphous state.[13]

6.3.4 Amorphization progression of IMC with Cys2 by ESR and FT-IR analysis

Figure 6-8 shows the ESR signals of the ground Cys2, ground IMC, and co-ground IMC with Cys2 samples by changing the grinding time at a revolution speed of 600 rpm. As the Cys2 samples ground with an increase in grinding time, the change in ESR signals were gradually observed as previously paper.[31] There was a little change in the ESR signals of ground IMC samples until 60 min, suggesting that tiny radical formation by grinding IMC until 60 min generated. However, the ESR signals indicated radical formation were almost the same regardless of grinding time after 60 min. Similarly, there was a little change in the ESR signals of ground IMC with Cys2 samples with an increase in grinding time although there was no major change in the ESR signals of single ground Cys2 samples. This result suggested that the radical formed from Cys2 may be related to the amorphized progression of IMC. It was reported that mechanical energy caused the decrease in the crystallinity of cellulose with radical formation, indicating that the radical formation during grinding may be related to the amorphization in the mechanochemistry.[46] Figure 6-9 shows the FT-IR spectra of untreated IMC, untreated Cys2, ground IMC, ground Cys2, the physical mixture of IMC/Cys2, and IMC/Cys2 co-ground at 400 rpm for 10 h. Spectroscopic techniques can detect solid-state changes at the molecular level. The peaks due to the γ-form of IMC are between 1695 and 1716 cm^{-1} and arise from the adsorption frequencies of the C¼O stretching vibration of benzoyl and carboxylic acid in the cyclic dimer.[44] Cys2 presents peaks at 1298, 1338, 1408, 1584, and 1620 cm^{-1} due to the characteristic adsorption frequencies of amide and carboxylic groups (NH_3^+ and COO^-).[47] Löbmann et al. reported that the FT-IR spectrum of amorphous IMC exhibits broader, less intense, and shifted peaks compared to the γ-form crystal and may be due to a range of molecular conformations and intermolecular bonding arrangements in the amorphous form.[48] In the present study, no new peaks were observed in the physical mixture and co-ground IMC/Cys2, indicating that no new intermolecular or intramolecular bonds were formed during co-grinding. However, the peak intensities at 1695 and 1716 cm^{-1} (from 1695 to 1681 cm^{-1}, and from 1716 to 1710 cm^{-1}) following decreased and peaks due to C=O shifted to lower wave number the amorphization of the γ-form of IMC in the presence of Cys2. This shift was previously reported.[41] Also, a shoulder peak at 1735 cm^{-1} arising from non-hydrogen bonded acid C=O was observed.[49] These results suggest that IMC in co-ground IMC/Cys2 becomes partially amorphous and monomers were released from their dimeric form. Acid and amide functional groups of IMC formed hydrogen bonds with the carboxylic acid of Cys2 rather than self-dimerize, as indicated by the increased intensity of the 1615–1635 cm^{-1} peak due to C=O bonding observed in ground Cys2. This suggests that IMC and Cys2 potentially interact via carboxylic bonds and may explain why Cys2 enhances the amorphization of IMC during co-grinding. There is no change in the IR spectrum of ground IMC alone, suggesting that the crystallinity of IMC is unchanged in the absence of an excipient. The potential interaction supported the leading of the amorphization of IMC than of Cys2 mentioned in the previous section as change of 1st PC score. Remaining IMC dimers were potentially detected as an increase in the 2nd PC score. 2nd PC score might capture these changes of interaction around dimers of IMC. The co-ground IMC/Cys2 samples therefore likely contained an amorphous fraction. And mode change of IMC dimer from the point of intermolecular interaction view.

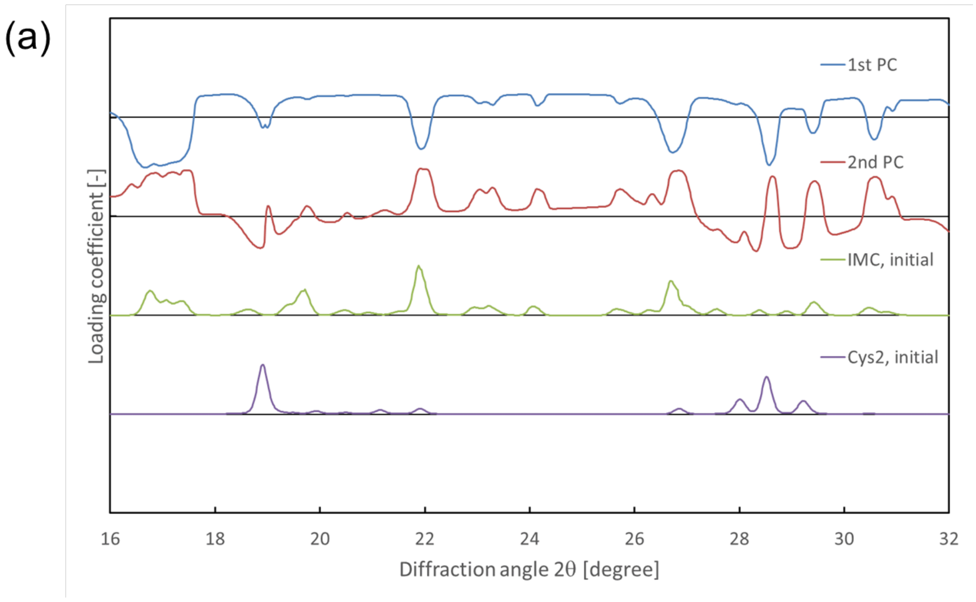

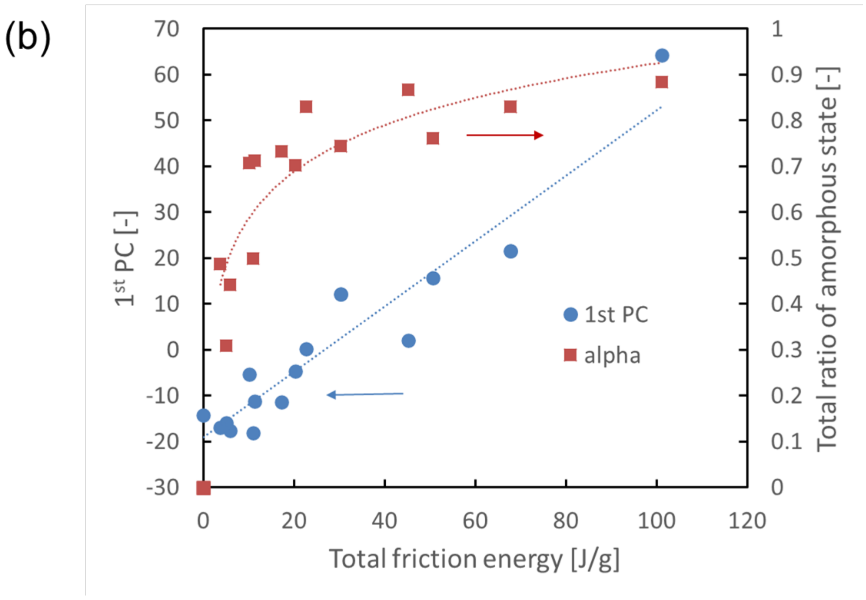

Fig. 6-6 PCA results, (a) Loading plot of the 1st PC and 2nd PC and (b) 1st PC score and total ratio of the amorphous state as a function of the total frictional energy as calculated by DEM simulation.

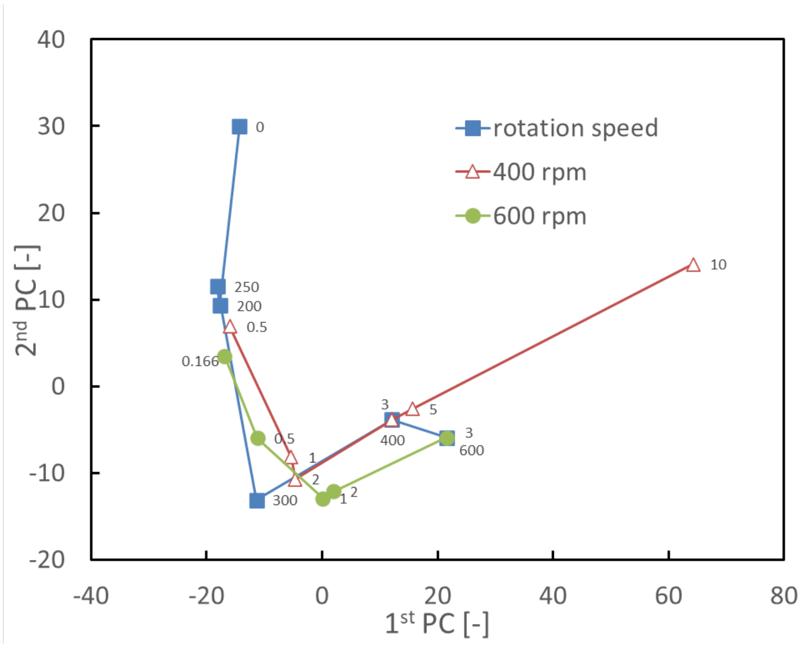

Fig. 6-7 PCA results, Score plot of the 1st PC and 2nd PC calculated using the XRPD spectra for different rotation speeds, grinding time at 400 rpm, and grinding time at 600 rpm.

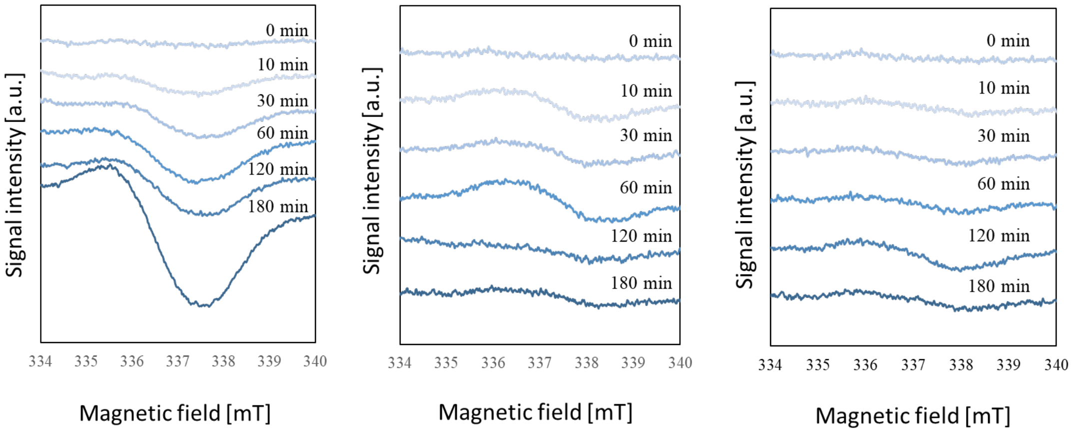

(a) (b) (c)

Fig. 6-8 ESR spectra of ground samples as time passes (a) ground Cys2 samples, (b) ground IMC samples, and (c) co-ground IMC with Cys2 samples.

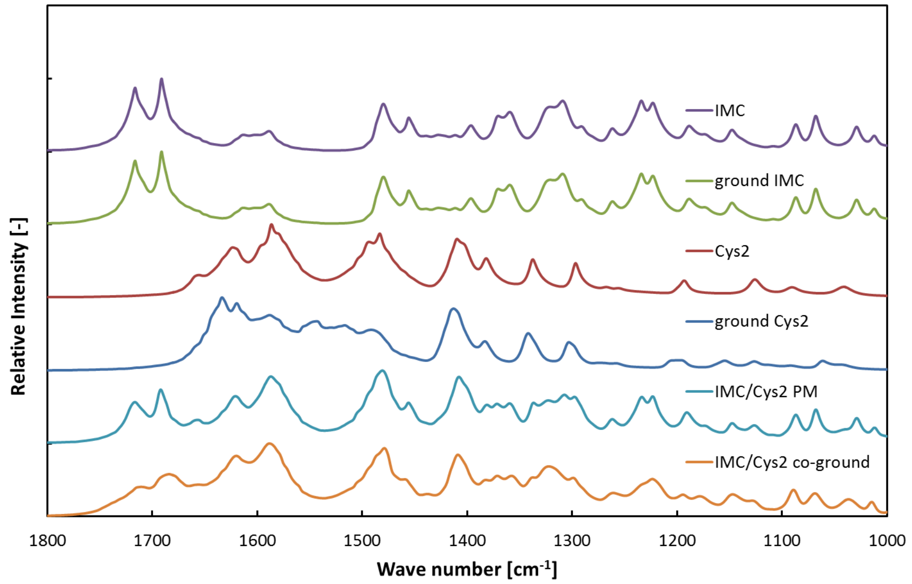

Fig. 6-9 FT-IR spectra of untreated IMC, ground IMC, untreated Cys2, ground Cys2, the physical mixture of IMC/Cys2, and co-ground IMC/Cys2.

6.3.5 Dissolution test

Dissolution tests were performed for untreated IMC, ground IMC, the physical mixture of IMC/Cys2, and co-ground IMC/Cys2 (Fig. 6-10). IMC has a low solubility of 0.937 g/L at 25°C[50] and Cys2 has a low solubility of 0.163 g/L in water at pH 7.0, 25°C.[51] Ground IMC and co-ground IMC/Cys2 were prepared at 400 rpm for 10 h. The dissolution profiles of untreated IMC and singe-ground IMC (400 rpm, 10 h) were similar, although single-ground IMC converted partially into the amorphous state. The physical mixture of IMC/Cys2 showed a higher dissolution rate than untreated IMC, attributed to the increase in solubility of IMC by the addition of Cys2. However, the dissolution rate of co-ground IMC/ Cys2 was double that of untreated IMC and resulted in significant interaction (P-value < 0.05) between Cys2 with IMC due to grinding.

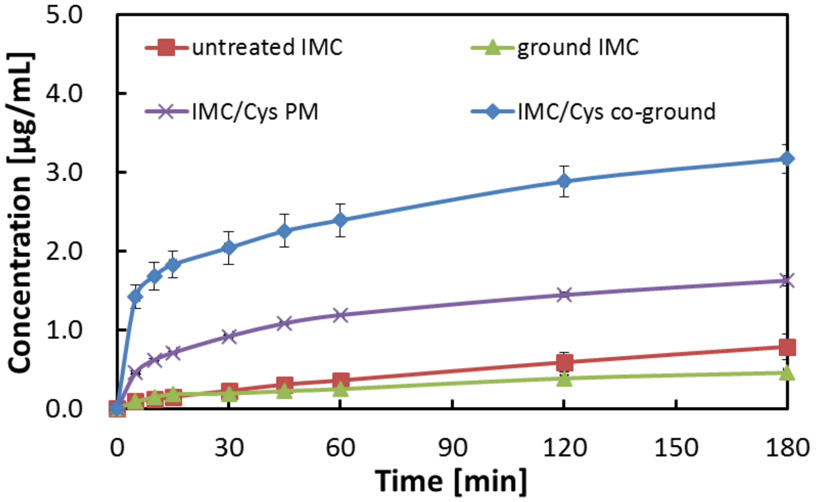

Fig. 6-10 Dissolution profile of untreated IMC, ground IMC, the physical mixture, and IMC/Cys2 co-ground at 400 rpm for 10 h.

6.4 Conclusion

Amorphization during co-grinding by planetary ball milling was studied using IMC and Cys2. XRPD, ESR, FT-IR, and dissolution tests suggested that the amorphization of IMC was enhanced by Cys2. PCA provided two PCs that captured approximately 80% of the system variation; combined with the XRPD spectra, the results showed that there are two phases to amorphization and the phase change depends on the total frictional energy as calculated by DEM simulation. The degree of amorphous IMC in an IMC/Cys2 sample is reflected in the 1st PC score and the difference in amorphization between IMC and Cys2 is reflected in the 2nd PC score during co-grinding. Designing a process allowing control of the amorphous content during co-grinding by ball milling requires an assumption of the total frictional energy, which would be a useful tool for analyzing as indicator without considering machine related parameters. Further understanding of the amorphization mechanism of drugs with an amino acid at the molecular level will require other approaches, such as systematic computational modeling, although we could explain the increase in the amorphous state of IMC with Cys2 using DEM and PCA.

*This chapter was reproduced and modified from [*J. Ind. Eng. Chem.,* 2018, **62**, 436-445], with permission from Elsevier.

References

[1] H. D. Williams, N. L. Trevaskis, S. A. Charman, R. M. Shanker, W. N. Charman, C. W. Pouton, C. J. H. Porter, *Pharmacol. Rev.*, 2013, **65**, 315

[2] S. J. Dengale, H. Grohganz, T. Rades, K. Löbmann, *Adv. Drug Deliv. Rev.*, 2016, **100**, 116

[3] S. Baghel, H. Catchcart, N. J. O'Reilly, *J. Pharm. Sci.*, 2016, **105**, 2527

[4] L. Yu, *Adv. Drug Deliv. Rev.*, 2001, **48**, 27

[5] N. L. Prasanthi, M. Sudhir, N. Jyothi, V. Srivajrapriya, *Am. J. Adv. Drug Deliv.*, 2016, **5**, 58

[6] Y. Sun, L. Zhu, T. Wu, T. Cai, E. M. Gunn, L. Yu, *AAPS J.*, 2012, **14**, 380

[7] A. Shayanfar, A. Jouyban, *J. Pharm. Innov.,* 2013, **8**, 218

[8] K. Gniado, K. Löbmann, T. Rades, A. Erxleben, *Int. J. Pharm.*, 2016, **504**, 20

[9] K. Löbmann, H. Grohganz, R. Laitinen, C. Strachan, T. Rades, *Eur. J. Pharm. Biopharm.*, 2013, **85**, 873

[10] K. T. Jensen, F.H. Larsen, C. Cornett, K. Löbmann, H. Grohganz, T. Rades, *Mol. Pharm.*, 2015, **12**, 2484

[11] A. W. Lim, K. Löbmann, H. Grohganz, T. Rades, N. Chieng, *J. Pharm. Pharmacol.* 2016, **68**, 36

[12] A. Beyer, L. Radi, H. Grohganz, K. Löbmann, T. Rades, C.S. Leopold, *Eur. J. Pharm. Biopharm.* 2016, **104**, 72

[13] Y. Hu, K. Gniado, A. Erxleben, P. McArdle, *Cryst. Growth Des.* 2014, **14**, 803

[14] K. Užarevic, V. Strukil, C. Mottillo, P. Julien, A. Puskaric', T. Friscıc', I. Halasz, *Cryst. Growth Des.*, 2016, **16**, 2342

[15] K.T. Jensen, K. Löbmann, T. Rades, H. Grohganz, *Pharmaceutics*, 2014, **6**, 416

[16] M. Descamps, A. Aumelas, S. Desprez, J. F. Willart, *J. Non Cryst. Solids*, 2015, **407**, 72

[17] C. F. Burmeister, A. Kwade, *Chem. Soc. Rev.* 2013, **42**, 7660

[18] L. S. Yong, M. Qiong-Jing, P. Zheng, L. Xiao-Dong, Y. Jian-Hua, *Chin. Phys. B,* 2012, **21**, 078201

[19] M. Khanal, C.T. Jayasundara, *Particuology* 2014, **16**, 54

[20] Y. T. Feng, K. Han, D.R.J. Owen, *Mat. Sci. Eng.*, 2004, **375**, 815

[21] P. W. Cleary, *Particuology*, 2010, **8**, 106

[22] H. Lee, H. Cho, J. Kwon, *Powder Technol.*, 2010, **198**, 364

[23] B. C. Hancock, G. Zografi, *Pharm. Res.*, 1994, **11**, 471

[24] S. A. Moggach, D. R. Allan, S. Parsons, L. Sawyer, J. E. Warren, *J. Synchrotron Radiat.*, 2005, **12**, 598

[25] M. Abdellaoui, E. Gaffet, *Acta Metall. Mater.* 1995, **43**, 1087

[26] M. V. Roux, C. Foces-Foces, R. Notario, J. Phys. Chem. B, 2010, **114**, 10530

[27] P. P. Chattopadhyay, I. Manna, S. Talapatra, S. K. Pabi, *Mater. Chem. Phys.*, 2001, **68**, 85

[28] H. Mio, J. Kano, F. Saito, K. Kaneko, *Mater. Sci. Eng. A*, 2002, **332**, 75

[29] K. T. Jensen, F.H. Larsen, K. Löbmann, T. Rades, H. Grohganz, *Eur. J. Pharm. Biopharm.*, 2016, **107**, 32

[30] H. Mio, J. Kano, F. Saito, K. Kaneko, *Int. J. Miner. Process.* 2004, **74**, S85

[31] Y. Konishi, K. Kadota, Y. Tozuka, A. Shimosaka, Y. Shirakawa, *Powder Technol.*, 2016, **301**, 220

[32] Y. Shirakawa, Y. Hayashi, K. Kadota, H. Mio, H. Ohtsuki, A. Shimosaka, J. Hidaka, *J. Nanopart. Res.*, 2008, **10**, 577

[33] L. Guzman, Y. Chen, S. Potter, M.R. Khan, *CIGR J.*, 2015, **17**, 235

[34] J. J. Ahn, K. Akram, J.H. Kwon, *Food Anal. Methods*, 2012, **5**, 1196

[35] B. M. Oughton, P.M. Harrison, *Acta Crystallogr.*, 1959, **12**, 396

[36] M. Ejgenberg, Y. Mastai, *Cryst. Growth Des.* 2012, **12**, 4995

[37] A. G. Shtukenberg, Z. Zhu, Z. An, M. Bhandari, P. Song, B. Kahr, M. D. Ward, *PNAS*, 2013, 110, 17195

[38] A.G. Flores-Huerta, A. Tkatchenko, M. Galva'n, *J. Phys. Chem. A*, 2016, **120**, 4223

[39] J. M. Aceves-Hernandez, I. Nicolás-Vázques, F. J. Aceves, J. Hinojosa-Torres, M. Paz, V. M. Castaño, *J. Pharm. Sci.*, 2009, **98**, 2448

[40] F. H. Chung, *J. Appl. Crystallogr.*, 1974, **7**, 519

[41] A. Sato, J. Kano, F. Saito, *Adv. Powder Technol.*, 2010, **21**, 212

[42] K. Shimono, K. Kadota, Y. Tozuka, A. Shimosaka, Y. Shirakawa, J. Hidaka, *Eur. J. Pharm. Sci.* 2015, **76**, 217

[43] B. M. Wise, N. B. Gallagher, *J. Process Control*, 1996, **6**, 329

[44] C. J. Strachan, T. Rades, K. C. Gordon, *J. Pharm. Pharmacol.* 2007, **59**, 261

[45] K. S. Khomane, P. K. More, G. Raghavendra, A. K. Bansal, *Mol. Pharm.*, 2013, **10**, 631

[46] A. V. Dushkin, *Chem. Sustain. Dev.*, 2004, **12**, 251

[47] Y. M. Fazil Marickar, P. R. Lekshmi, L. Varma, P. Koshy, *Urol. Res.*, 2009, **37**, 263

[48] K. Löbmann, R. Laitinen, C. Strachan, T. Rades, H. Grohganz, *Eur. J. Pharm. Biopharm.,* 2013, **85**, 882

[49] L. S. Taylor, G. Zografi, *Pharm. Res.* 1997, **14**, 1691

[50] S. Basavoju, D. Boström, S. P. Velaga, *Pharm. Res.* 2008, **25**, 530

[51] R. Carta, G. Tola, *J. Chem. Eng. Data*, 1996, **41**, 414

Chapter 7 Concluding remarks

To assure the robust quality and process, it is quite important to support the design of control strategy by understanding of the particle characteristics and how the particles are generated and changed especially via interfacial phenomena which less observed experimentally. Therefore, a microscopic study of interfacial phenomena affecting particle characteristics of drug substance has been presented in this thesis which has conducted by comprehensive approach including numerical simulation and statistical approach to get further fundamental understanding in terms of intrinsic behavior of related molecules and multi-interacted behavior.

In Chapter 2, nonequilibrium molecular dynamics (MD）simulations have been performed at interfaces in NaCl solution/1-butanol and KCl solution/1-butanol system in order to clarify diffusion behavior of solute ions and solvent molecules as simple case of anti-solvent crystallization. The solute ions were dehydrated with the diffusion of water from aqueous phase into 1-butanol phase. The different dehydration behaviors between NaCl and KCl solution can be also obtained. Cluster ions were formed by the dehydration near the solution/1-butanol interface. By comparison on the normalized number of total solute ions, the size and number of generated clusters in KCl solution/1-butanol interface are larger than those in the NaCl system. This originates in the difference hydration structures in each solute ion.

In Chapter 3, non-equilibrium molecular dynamics simulations were also performed for clarifying the mutual diffusion and ionic behavior near the liquid–liquid interface between KCl aqueous solution and organic solvent (1-butanol, 2- butanol, 2-methyl-1-propanol and 2-butanone). The 2-butanone molecules were clearly oriented to the aqueous phase among the aqueous and organic interfaces. Orientation of

2-butanone molecules significantly inhibited mutual diffusion between KCl aqueous solution and 2-butanone. Clusters, which were aggregated ions, were formed by the dehydration of potassium and chloride ions in the interfacial reason between KCl aqueous solution and organic solvent. The number of clusters at interface between KCl solution and 2-butanone was larger than that in other solvents. This indicates that organic solvents need to be evaluated of electronegativity and concentration fluctuation of solute ions is enhanced by 2-butanone near the interface.

In Chapter 4, the anti-solvent crystallization behavior of the glycine aqueous and ethanol system was addressed through a molecular dynamics simulation of a non-equilibrium state. Glycine zwitterions began to aggregate into clusters with the invasion of ethanol into the aqueous phase, caused by the dehydration and supersaturation of the area. The number and size of clusters gradually increased with the formation and collapse of the clusters with time progression as partially structured liquid–liquid phase separation. Pre-determination of the crystal polymorph during liquid–liquid phase separation was support from this partially structured mode of glycine zwitterion. Besides larger clusters which is over the critical size in classical nucleation theory increased and this deviation from the theory suggests complexity of nucleation of glycine which described by two-step nucleation theory.

Through the Chapter 2 to 4, it was revealed how each solute and solvent molecule behave near the interface and their diffusion behavior affect nucleation during anti-solvent crystallization from investigation of the cluster which seems precursor related to polymorph determination. This helps the further understanding of both classical and two-step nucleation theory in general and may lead the next step for the establishment of more sophisticated nucleation theory.

In chapter 5, TiO_2 hollow particles encapsulating the vitamins C and E were investigated not only the process via a sol-gel process using an inkjet nozzle but also their structures and related release performance at liquid–solid interface. The TiO_2 hollow particles were successful in encapsulating both the hydrophilic vitamin C and the hydrophobic vitamin E, resulting in a sustained release profile for these two components from the TiO_2 hollow particles. The difference of release behavior of the single and multivitamin seems originated from the adsorption state of each vitamin on the TiO_2 particle surface. Additionally, the value of multicomponent was always larger than that of single component and Knudsen diffusion coefficient was larger than molecular diffusion coefficient in all conditions. This suggest that the diffusion mechanism of the drug substances likely depends on the pore size of TiO_2 and the molecular size of the drug substances based on dominated interaction between molecules (dispersed in liquid) and pore surface of TiO_2 (solid).

In Chapter 6, The amorphization of indomethacin (IMC) with cystine (Cys2) was studied by discrete element method (DEM) simulations and principal component analysis (PCA). X-ray powder diffraction (XRPD) analysis suggested that the conversion of crystalline IMC to amorphous state was accelerated by co-grinding with Cys2. XRPD spectra about amorphization of IMC with Cys2. PCA results suggest that IMC/Cys2 system undergoes two-phase amorphization without any physical interpretation and the change in phase depends on the total frictional energy calculated by DEM simulations. Electron spin resonance result revealed that the radical from Cys2 may lead the amorphized progression of IMC. The indicator from numerical simulation may reach out the amorphous state during milling with combination of statistical analysis.

Finally, this work showed the mechanistic understanding of interfacial phenomena affecting particle characteristics at molecular level, especially nucleation of anti-solvent crystallization and amorphous state during milling process via multi approaches to the science. I believe that these findings will give light on further understanding of intrinsic phenomena and be an essential part of robust design of the processes.

List of publications

I. Akira Kitayama, Shinya Yamanaka, Kazunori Kadota, Yoshiyuki Shirakawa, Atsuko Shimosaka, Jusuke Hidaka, 2009. Diffusion and Cluster Formation near NaCl Solution/Organic Solvent Interface in a Crystallization Process. Journal of Chemical Engineering of Japan. 42, 346-350.

II. Akira Kitayama, Shinya Yamanaka, Kazunori Kadota, Atsuko Shimosaka, Yoshiyuki Shirakawa, Jusuke Hidaka, 2009. Diffusion Behavior in a Liquid–liquid Interfacial Crystallization by Molecular Dynamics Simulations. Journal of Chemical Physics. 131， 174707.

III. Kazunori Kadota, Taiki Wake, Kazuki Gonda, Akira Kitayama, Yuichi Tozuka, Atsuko Shimosaka, Yoshiyuki Shirakawa, Jusuke Hidaka, 2014. Effect of Organic Solvent on Mutual Diffusion and Ionic Behavior Near Liquid‐liquid Interface by Molecular Dynamics Simulations. Journal of Molecular Liquids. 197, 243-250.

IV. Akira Kitayama, Kazunori Kadota, Seika Fujioka, Yuto Konishi, Hiromasa Uchinaya, Yuichi Tozuka, Atsuko Shimosaka, Mikio Yoshida, Yoshiyuki Shirakawa, 2018. Assessment of amorphization behavior of a drug during co-grinding with an amino acid by discrete element method simulation. Journal of Industrial and Engineering Chemistry. 62, 436-445.

V. Yoko Tominaga, Akira Kitayama, Yuichi Tozuka, Atsuko Shimosaka, Mikio Yoshida, Yoshiyuki Shirakawa, 2019. Diffusion mechanism and release profile of a multivitamin from TiO2 hollow particles. Advanced Powder Technology. 30, 2989-2996.

VI. Akira Kitayama, Kazunori Kadota, Yuichi Tozuka, Atsuko Shimosaka, Mikio Yoshida, Yoshiyuki Shirakawa, 2020. Molecular aspects of glycine clustering and phase separation in an aqueous solution during anti-solvent crystallization. CrystEngComm. 22, 5182-5190.

Appendix: Molecular Dynamics Simulation

In the Chapter 2 and 3, several potential function of interaction among potential sites of molecules were commonly applied to the molecular dynamics simulations. In this appendix, the values of forcefields are summarized in following tables.

Table A-1 Potential parameters (intermolecular interactions: LJ potential +charge−charge electrostatics).

site	q [e]	σ [nm]	ε [kJ/mol]
O (water)	-0.8476	0.3169	0.6502
H (water)	0.4238	0	0
CH_3 (1-butanol)	0	0.3905	0.7320
CH_3 (2-butanol)	0	0.3750	0.8148
CH_3 (2-methyl-1-propanol)	0	0.3750	0.8148
CH_3 (2-butanone)	0	0.3750	0.8148
CH_2 (1-butanol)	0	0.3905	0.4936
CH_2 (2-butanol)	0	0.3905	0.3825
CH_2 (2-methyl-1-propanol)	0.2650	0.3950	0.3825
CH_2 (2-butanone)	0.2650	0.3950	0.4936
CH_2 (in $–CH_2OH$)	0.2650	0.3905	0.4936
CH (in –COH)	0.2650	0.4330	0.0831
CH (in $–CH_3$)	0.2650	0.4680	0.0831
C=O (in –CO)	0.4240	0.3820	0.3825
O (1-butanol)	-0.7000	0.3775	0.4936

O (2-butanol)	-0.7000	0.3020	0.7732
O (2-methyl-propanol)	-0.7000	0.3020	0.7732
O (2-butanone)	-0.4240	0.3050	0.3326
H (1-butanol)	0.4350	0	0
H (2-butanol)	0.4350	0	0
H (2-methyl-1-propanol)	0.4350	0	0
Na+	1.0	0.2583	0.4184
K+	1.0	0.3331	0.4184
Cl-	-1.0	0.4400	0.4184

Table A-2 Potential parameters (Intramolecular interactions: bond length, bond angle or torsion angle)

a) Bond length

	Bond length
	[nm]
O-H (water)	0.1000
C-C (1-butanol)	0.1530
C-C (2-butanol)	0.1540
C-C (2-methyl-1-propanol)	0.1540
C-C (2-butanone)	0.1520
C-O (1-butanol)	0.1430
C-O (2-butanone)	0.1229
O-H (1-butanol)	0.0945

b) Bond angle

	$U_{bend} = K_b(\theta - \theta_{eq})^2$	
	K_b [kJ/mol]	θ_{eq} [degree]
H–O–H	N/A	109.47
CH_3–CH_2–C(=O)	519.66	114
CH_2–C=O, O–C–CH_3	519.66	121.4
CH_2–C–CH_3	519.66	117.2
CH_3–CH_2–CH(–O)	519.66	114
$CH_{2(1)}$ –$CH_{(2)}$ –O, O–CH–CH_3	432.91	109.47
$CH_{(2)}$–O–H	460.62	108.5
$CH_{2,3}$–CH_2–CH_3	519.66	112

c) Torsion angle

	$U_{torsion}(\varphi) = K_{t0} + K_{t1}(1 + \cos\varphi) + K_{t2}(1 - \cos 2\varphi) + K_{t3}(1 + \cos 3\varphi)$			
	K_{t0} [kJ/mol]	K_{t1} [kJ/mol]	K_{t2} [kJ/mol]	K_{t3} [kJ/mol]
C–C–C–C	0	6.368	-1.322	13.418
CH_2–CH_2–CH_2–O	0	2.937	-0.887	12.803
CH_2–CH_2–O–H	0	3.489	-0.485	3.125
C–C–C_O	16.975	-6.127	0.481	-2.438
CH_2–CH–O–H	1.796	1.641	0.262	-1.446
CH_3–CH–CH_2–O	0	1.469	-0.443	6.402
CH–CH_2–O–H	0	1.745	-0.243	1.563

Acknowledgements

First of all, I highly appreciated my supervisor, Prof. Yoshiyuki Shirakawa, for his invaluable guidance and support. This thesis would not have been able to accomplish without his supervision and patience. I would also like to thank my committee members, Prof. Michiaki Matsumoto and Prof. Hiromitsu Yamamoto, for their thoughtful feedback and comments. Prof. Yuichi Tozuka, Prof. Mikio Yoshida and Dr. Atsuko Shimosaka are acknowledged for their valuable comments and great.

I sincerely thank to Prof. Kazunori Kadota for providing me the support and helpful discussion, numerous ideas and constructive criticism. I would like to express my sincere gratitude to Mr. Taiki Wake, Kazuki Gonda, Yuto Konishi, Ms. Seika Fujioka, Yoko Tominaga for their experimental and numerical simulation works. I also thank Prof. Shinya Yamanaka, Dr. Ryoichi Furukawa, Mr. Yoshihisa Maeyama, Dr. Yuto Deki, Mr. Yuki Saito and Daichi Kawabata for grateful supports of my research. Also thanks to my colleagues, Mr. Masami Murata, Dr. Takahiro Yamamura, Dr. Akiko Koga, Mr. Tomoaki Ohta and Dr. Kenichi Sakai have been continuing support.

I would like to thank for a scholarship "Doshisha University Graduate School Scholarships for Young Doctoral Students/Researchers" as a financial support.

Finally, special thanks for the years of patience, unmeasurable help and unconditional support to my wife Yumi throughout my research. Thanks also to my parents Hiroaki and Masako for the permanent support, especially highly appreciated to my daughter Emma and grandfather Tadaaki for keeping me motivated in the moments when I needed.

Akira Kitayama, 29th July, 2020